INVESTIGATING SPHINGOLIPID BEHAVIOR AND FUNCTION USING METABOLIC LABELING

BY

RAEHYUN KIM

DISSERTATION

Submitted in partial fulfillment of the requirements
for degree of Doctor of Philosophy in Chemical Engineering
in the Graduate College of the
University of Illinois at Urbana-Champaign, 2016

Urbana, Illinois

Doctoral Committee:

Associate Professor Mary L. Kraft, Chair
Professor Ryan C. Bailey
Professor Deborah E. Leckband
Associate Professor Charles M. Schroeder

ABSTRACT

The past few decades of research have accumulated a body of evidence that membrane lipids are far more than merely the structural components of biological membranes. Instead, membrane lipids play important roles in cellular functions in multiple ways. Sphingolipids are a group of lipids that are involved in various cellular processes that are crucial for cell survival and proliferation. However, our understanding of sphingolipid function is limited due to the complexity of their behaviors and the lack of proper tools to address and decipher this complexity.

Chapters 2 and 3 present metabolic labeling with fluorophores and stable isotope tags, respectively, as tools to investigate sphingolipid behaviors. Metabolic labeling enables one to detect and directly observe sphingolipids, and not the activities or levels of the enzymes that metabolize them. Metabolic labeling of cells with fluorescent sphingosines enabled visualization of the sphingosine metabolites in live cells and also showed potential for studies of metabolism and in vitro assays. Use of stable isotope tagged sphingolipid precursors, in conjunction with LC-MS/MS analysis, provided a more comprehensive and complete dataset than traditional radiolabeling, including information about unlabeled as well as labeled species. These tools offer great opportunities to explore sphingolipid behaviors.

In Chapter 4, based on the observations that sphingolipids have significant roles in membrane organization and that virus infection requires intense membrane reorganization, the involvement of acid sphingomyelinase or sphingomyelin phosphodiesterase 1 (SMPD1), a sphingolipid metabolizing enzyme, in influenza virus infection and particularly its entry was evaluated using RNAi and a pharmacological inhibitor. Western blotting performed prior to infection showed that a significantly higher level of SMPD1 was present in the medium than in the cells. Lowering SMPD1 levels by RNAi or a functional pharmacologic inhibitor, desipramine,

did not cause a statistically meaningful change in influenza virus entry. However, influenza virus infection itself was correlated with upregulated SMPD1 levels at the early phase of infection, opening the possibility that sphingolipids may still play an important role in influenza virus infection. Further investigation of the role of SMPD1 in influenza virus infection is necessary.

Lastly, in Chapter 5, the cellular uptake of protein-coated nanoparticles was investigated in an effort to understand how plasma proteins interact with the nanoparticle surface, and to enhance the efficiency of targeted nanoparticle delivery with an in vitro system that mimics the in vivo environment. Formation of the protein corona, the protein layer that adsorbs on the surface of the nanoparticle when it is exposed to a biological fluid, is reported to prevent the desired interactions between the nanoparticles and the target cells. Exploiting the well-established mechanism of opsonin-mediated endocytosis in immune cells, we tested whether the protein corona itself can be used as a targeting moiety. Pre-coating the nanoparticles with γ-globulins provided a simple route to enrich the protein corona with opsonins. However, the increased opsonin levels in the protein corona did not enhance cellular uptake, but instead significantly decreased it. Immunodot blot assay and confocal fluorescence microscopy showed that these nanoparticles were internalized through opsonin-receptor interactions, but the opsonins on the nanoparticle were not accessible. This indicates that other components in the protein corona shielded the opsonins, preventing them from interacting with their target receptor. This study demonstrates that the spatial organization of the targeting moieties is critical, and it must be optimized for more efficient targeted nanoparticle delivery.

ACKNOWLEDGMENTS

First, many thanks to my adviser Prof. Mary Kraft, for offering great opportunities and an environment to learn and grow throughout my PhD training. I should also point out that only a few people in the world would have the experience of going to Disneyland with their Ph. D. adviser and I am one of those few lucky people. I would also like to thank my committee members; Prof. Charles Schroeder, Prof. Deborah Leckband, and Prof. Ryan Bailey for their time and valuable advice.

Many thanks go to my labmates, both old and current. We have been through many things together, including the frozen pipe, the raccoon attack, and the lab moving. Thanks to Professor Kaiyan Lou for helping me a lot on my first project in the Kraft group with the magic of organic chemistry and re-educating me on TLC, Bill Hanafin for teaching me all about how to take good care of cells and offering help any time, Dr. Robert Wilson for providing me so many great stories (both directly and indirectly, you have no idea), Dr. Jessica Frisz for being open minded and super nice whenever I needed her knowledge and intelligence, Dr. Haley Klitzing for taking really good care of small and big things in Kraft lab and being a nice and fun labmate, Dr. Ashley Yeager for opening my eyes to viruses and infection and being a great coworker, Dr. Vahid Mirshafiee for inviting me to the wonderful world of protein corona and working together to conquer it, Yelena Illin for bringing the urban feel (which I missed a lot) from NYC and the dark humor, Corryn Neumann and Sayani Majumdar for being friendly and keeping my knowledge fresh by asking questions. Thanks to the undergraduates who worked with me, Lauren, Sean, Simeyon, Hannah, and Soyun, for bringing freshness and energy to lab.

I would like to thank the staff scientists who helped me along during my PhD training throughout campus. Thanks to Dr. Alexander Ulanov and Dr. Zhong Li at the Metabolomics center, to Dr. Peter Yau and Dr. Brian Imai at the Protein Sciences Facility, to Tatsiana Akraiko at the Functional Genomics Unit at the Roy J. Carver Biotechnology Center for immense help on the instruments and the analyses. Thanks also to Dr. Mayandi Sivaguru at the Carl R. Woese Institute for Genomic Biology for helping with the microscopy and also offering me great opportunities for the outreach programs there.

Thanks to my friends in the USA and other parts of the world. I have been very lucky to have great friends and I am grateful for that. Thanks to So Youn, Youyun, Molly, Santosh, Nik, Peter, Jess, Amanda, Gina, Victor, Kara, Kyle, Mike and my fellow ChemEs for having so much fun with me and introducing many great things that were new to me. I am fond of the memories with you guys. And of course, thanks to Mei, Grace, Cartney, Jess, Nick, and Ellen, my good friends and also lovely neighbor back in Davenport Hall for having great times together both at and out of work and also keeping company with me in such a long way to RAL. Special thanks to Mr. Handsome (a.k.a. Dr. Koirala) for saving me with his expertise, supporting me and sometimes pushing me when needed (I really needed that), and to Dr. Ji Sun Sunny Choi, my best friend at U of I, for supporting and encouraging me, and being there for me. And thanks to all my friends back home for being supportive and being there for me when I was going through hard time.

And lastly and most importantly, many thanks from my heart to my family for being super supportive for every step I take throughout my life. An hour long weekly phone call with mom was vital for keeping me sane. I should thank Apple for making Facetime available all around the world so that my sister could broadcast what happened at home. Dad, I hope you rest in peace. We miss you. I love you guys so much and I'm with you wherever I am.

TABLE OF CONTENTS

CHAPTER 1

INTRODUCTION

1.1 MEMBRANE LIPIDS

Every cell has a plasma membrane that separates itself from the surrounding environment. In addition, the organelles within eukaryotic cells are also surrounded by membranes. Cellular membranes consist of a self-assembled lipid bilayer. The fluid mosaic model suggests that the lipids in the membrane have fluid-like properties that allow membrane proteins to freely diffuse in the lateral direction.[1] Consequently, membrane lipids were once thought to merely function as structural components of cellular membranes. However, the past few decades of research have revealed that membrane lipids are not just structural components of cellular membranes, but they also play important, active roles in mediating diverse cellular functions.

Several mechanisms of how membrane lipids are involved in biological functions have been hypothesized and studied. First, certain membrane lipids, specifically sphingolipids and sterols, are thought to form functionally and compositionally distinct lipid domains in plasma membranes and more recently, nuclear envelops.[2-4] Second, some lipids are enzymatically converted to metabolites that act as second messenger signaling molecules by activating downstream signaling events.[5,6] For instance, the conversion of phosphatidylcholine (PC) to diacylglycerol (DAG) at the plasma membrane activates protein kinase C (PKC), triggering downstream signaling.[7] Lastly, some lipids bind directly to proteins and regulate the proteins' activities. Many proteins have lipid binding domains, such as C2 domains or SH domains that can precisely regulate their location and activities.[8] The direct and selective binding of specific lipid species to certain proteins that lack typical lipid binding domains have been also observed. COPI machinery protein p24 interacts specifically with C18 sphingomyelin (sphingomyelin that is acylated with stearic acid, a saturated 18-carbon fatty acid) and regulates COPI dependent transport in the cells.[9] C99, a protein generated from full-length amyloid precursor protein (APP) by ß-secretase, binds to cholesterol through GXXXG motifs; this binding affects the protein's conformation and enhances its cleavage by γ-secretase, which produces Aß polypeptides.[10]

Membrane lipids can be generally categorized into three classes, sterols, glycerophospholipids, and sphingolipids. Structurally, sterols are distinct from other membrane lipids due to their polycyclic ring structure. Cholesterol is a sterol lipid that is abundant in mammalian membranes, comprising approximately 30-40 mol% of all plasma membrane lipids.[11] Sterols are the major non-polar membrane lipid and are known to affect membrane fluidity and organization.[12,13]

Glycerophospholipids are a major structural membrane lipid class that comprises about 50 mol% of the plasma membranes.[11] Glycerophospholipids have two hydrophobic fatty acids and a hydrophilic head group that are attached to the glycerol backbone. This class includes phosphatidylcholine (PC), phosphatidylethanolamine (PE), phosphatidylserine (PS), phosphatidylinositol (PI), and phosphatidic acid (PA). In healthy cells, glycerophospholipids are heterogeneously distributed across the plasma membrane. Typically, PC is in the outer leaflet (exoplasmic leaflet) while PE and PS are primarily located in inner leaflet (cytosolic leaflet). This heterogeneity is maintained by lipid flippases and scramblases in the membranes.[11]

Sphingolipids are distinguished from glycerophospholipids by their sphingoid backbone. The amine moiety in this sphingoid backbone allows hydrogen bonding among sphingolipids or other membrane lipids, such as cholesterol.[11] Most membrane sphingolipids are *N*-acylated. Sphingomyelins, the most abundant sphingolipid in mammalian cells, have a phosphocholine head group, analogous to PC in the glycerophospholipid family. About 10-15 mol% of mammalian plasma membrane lipids are sphingolipids. Sphingolipids are discussed in more detail in the next section.

1.2 SIGNIFICANCE OF SPHINGOLIPIDS

Sphingolipids have been of great interest due to their significance in many pathological conditions.[14] Mutations in certain sphingolipid metabolic enzymes directly cause lysosomal lipid storage diseases that often present progressive neurodegeneration.[15] Aberrant levels of sphingolipids or sphingolipid metabolic enzymes have been also reported in many other pathological conditions. Ceramide synthase and ceramide levels were found to be statistically and significantly higher in malignant tumor tissue that the corresponding healthy tissue.[16] Inflammation is indicated to alter sphingolipid metabolism,[5] and impaired sphingolipid metabolism is associated with Alzheimer's disease.[17] Sphingolipids have proven to be a successful target for the treatment of multiple sclerosis. Specifically, fingolimod (FTY720), a FDA approved immunomodulatory drug that is taken orally to treat multiple sclerosis, is a structural analogue of sphingosine.[18] The involvement of sphingolipids in infections will be discussed in Chapter 4.

Sphingolipids and their metabolites are involved in numerous cellular signaling events in which they trigger downstream effectors that are important for biological functions. A number of comprehensive reviews on how sphingolipids regulates signaling events in the cells have been published.[5,19-27] Ceramides, sphingosine, and sphingosine-1-phosphate (S1P) are among the well-known bioactive sphingolipid molecules. Ceramides mediate various stress responses, such as apoptosis and cell growth arrest.[19] Ceramides can interact with a number of signaling molecules, including kinase suppressor of Ras (KSR), atypical protein kinase-C (aPKC), c-Raf-1, cathepsin D, protein phosphatase 2A (PP2A) and ceramide-activated protein phosphatase.[22] The physiological mechanisms through which ceramides regulate those signaling events are still not clear. In the classical view, ceramides have been thought to be a second messenger that affects the activity or localization of signaling proteins. However, recent data challenge this view and support the alternative model where changes in local ceramide levels alter membrane organization and, in turn, change the localization of certain proteins.[22] In addition to ceramide, sphingosine can also affect cellular signaling events. Sphingosine inhibits the anti-apoptotic function of 14-3-3 proteins by binding to them, which regulates their phosphorylation.[28] Sphingosine can also inhibit PP2A by binding to PP2A inhibitors ANP32a and ANP32b.[22] Sphingosine can be phosphorylated by sphingosine kinases. The phosphorylated product, S1P, is known to be pro-survival and mitogenic. S1P is a ligand for five S1P receptors (S1PRs). These S1PRs are G-protein coupled receptors (GPCRs, also known as 7 transmembrane (7TM) receptors). Each receptor triggers different downstream G protein(s) and induces different biological consequences.[25-27] Through these receptors, S1P regulates migration,[29] cytoskeletal organization,[30] angiogenesis and vasculogenesis.[31,32] Due to the opposite outcomes of ceramides and S1P signaling, the sphingolipid rheostat model has been hypothesized. The key concept of the sphingolipid rheostat model is the balance between pro-apoptotic ceramides and pro-survival S1P. Imbalance between two signaling molecules is associated with diseases, such as cancer and diabetes.[33-36]

Lastly, sphingolipids have been intensely studied in a biophysics perspective. Sphingolipids form lipid domains that are physically and chemically distinct from non-domain regions. Super-resolution fluorescence microscopy and high-resolution imaging mass spectrometry have independently demonstrated the presence of sphingolipids-enriched domains in the plasma membrane.[3,37] Sphingolipids have the capability to create curvature in the membrane. The conversion of sphingomyelin to ceramide significantly reduces the size of the head group. Such decrease in lipid head group size is known to induce curvature in model membranes.[38,39] This ceramide-induced curvature has been suggested to mediate membrane repair and exosome sorting. When the cells are wounded, lysosomal acid sphingomyelinase leaks out of the cells and converts sphingomyelins to ceramides in the plasma membrane, which can create an invagination that initiates endocytosis of the damaged region of the membrane.[40] Neutral sphingomyelinases can produce similar effects inside the cells. This neutral sphingomyelinase-dependent ceramide production has been shown to induce exosomes to bud into multivesicular endosomes.[38]

In summary, sphingolipids have significant roles in numerous cellular processes, and multiple mechanisms may be responsible for their actions. Therefore, it is critical to understand sphingolipid metabolism and behavior inside cells.

1.3 SPHINGOLIPID METABOLISM AND TRAFFICKING

Ceramides are at the center of sphingolipid metabolism. Ceramides are synthesized at the endoplasmic reticulum (ER) by the *N*-acylation of sphingoid backbones. The sphingoid backbones can be produced by the de novo pathway from the condensation of serine and palmitoyl CoA by serine palmitoyltransferase and then reduction by 3-ketodihydrosphingosine reductase, or by the degradation of complex sphingolipids at the lysosomes. Ceramides can be further processed to more complex sphingolipids that have larger head groups, such as sphingomyelins, glycosphingolipids, or gangliosides, and this mostly occurs at the Golgi apparatus. Ceramides can be also deacylated to produce sphingosine and a fatty acid. The resulting sphingosine can be reused to produce ceramide or phosphorylated to S1P. As discussed above, S1P is a ligand for S1P receptors, which are G protein coupled receptors that are involved in cell proliferation, migration, and many other biological functions. S1P can also be irreversibly catabolized to hexadecenal and ethanolamine phosphate by sphingosine-1-phosphate lyase. Sphingolipid metabolism is described in detail in Figure 1.1.

The intracellular distribution of sphingolipids is controlled by sphingolipid metabolism and transport. Organelle-specific enzymes regulate local sphingolipid levels. Ceramide synthase in the ER is responsible for ceramide synthesis. The conversion of ceramides to sphingomyelins or glycosphingolipids is carried out by transferases, namely sphingomyelin synthase and ceramide glucosyltransferase, in the Golgi apparatus. Sphingolipids are also metabolized at the plasma membrane. Sphingomyelin synthase 2 (SMS2) and neutral sphingomyelinases 2 (nSMase2) are found at the plasma membrane. Mitochondria also contain a neutral sphingomyelinase that is known to be specific to mitochondria.[41] At the lysosomes, sphingolipids are degraded by acidic catabolic enzymes, such as acidic sphingomyelinase (aSMase) and acid ceramidase. Therefore, organelle-specific sphingolipid metabolic enzymes are found in almost every organelle in the cell.

Sphingolipid transport has a huge impact on sphingolipid distribution throughout the cells. For instance, the level of sphingolipids is very low at the ER where sphingolipid synthesis takes place, which suggests that sphingolipids are rapidly transported out of the ER. The majority of sphingolipids are found in the plasma membrane, and this is thought to result from vesicular trafficking from the ER to the Golgi and then to the plasma membrane. Nonvesicular sphingolipid transport has also been reported. CERT (ceramide transfer protein) and FAPP2 (four-phosphate-adaptor protein 2) transfer ceramide from the ER to the trans-Golgi and glycosphingolipids from the trans-Golgi network to the plasma membrane, respectively.[42-44] This nonvesicular trafficking of ceramide from the ER to the Golgi is necessary for the synthesis of sphingomyelin, but not glucosylceramide.[44]

In summary, the subcellular distributions of sphingolipids are regulated and maintained by their metabolism and trafficking.

1.4 NOVEL TOOLS TO STUDY BEHAVIORS OF SPHINGOLIPIDS

Since sphingolipid metabolic enzymes were cloned,[45-47] many of them have been manipulated by overexpression,[48] knock-out by gene targeting,[49,50] or downregulation using RNAi[51] or pharmacological drugs[52,53] to probe the roles of sphingolipid metabolism in many different signaling pathways. Much less effort has been made to directly measure the local intracellular abundances of specific sphingolipid species or track their transport in the cell. Yet, much research suggests the direct involvement of sphingolipids such as ceramides and S1P,[19] and not the enzymes that produce them, in signaling events, whereas the sphingolipid metabolic enzymes play secondary roles, namely regulating the levels of bioactive sphingolipids. Therefore, to truly understand how sphingolipids affect cell signaling and function, more efforts should focus on to directly measuring and observing sphingolipids. For this reason, I aimed to utilize metabolic labeling with fluorescently labeled sphingolipid precursors (Chapter 2) and stable isotope-labeled sphingolipid precursors (Chapter 3) to investigate sphingolipid behaviors.

1.5 REFERENCES

1 S. J. Singer & G. L. Nicolson. The fluid mosaic model of the structure of cell membranes. *Science* **175**, 720-731 (1972).

2 K. Simons & E. Ikonen. Functional rafts in cell membranes. *Nature* **387**, 569-572 (1997).

3 J. F. Frisz *et al.* Direct chemical evidence for sphingolipid domains in the plasma membranes of fibroblasts. *Proc. Natl. Acad. Sci. U. S. A.* **110**, E613-E622 (2013).

4 G. Cascianelli, M. Villani, M. Tosti, F. Marini, E. Bartoccini, M. V. Magni & E. Albi. Lipid microdomains in cell nucleus. *Mol. Biol. Cell* **19**, 5289-5295 (2008).

5 M. Maceyka & S. Spiegel. Sphingolipid metabolites in inflammatory disease. *Nature* **510**, 58-67 (2014).

6 G. Van Meer, D. R. Voelker & G. W. Feigenson. Membrane lipids: where they are and how they behave. *Nat. Rev. Mol. Cell Biol.* **9**, 112-124 (2008).

7 Y. Saburi *et al.* Changes in distinct species of 1, 2-diacylglycerol in cardiac hypertrophy due to energy metabolic disorder. *Cardiovasc. Res.* **57**, 92-100 (2003).

8 J. P. Dinitto, T. C. Cronin & D. G. Lambright. Membrane recognition and targeting by lipid-binding domains. *Sci. STKE* **2003**, re16 (2003).

9 F.-X. Contreras *et al.* Molecular recognition of a single sphingolipid species by a protein's transmembrane domain. *Nature* **481**, 525-529 (2012).

10 P. J. Barrett *et al.* The amyloid precursor protein has a flexible transmembrane domain and binds cholesterol. *Science* **336**, 1168-1171 (2012).

11 J. C. Holthuis & T. P. Levine. Lipid traffic: floppy drives and a superhighway. *Nat. Rev. Mol. Cell Biol.* **6**, 209-220 (2005).

12 R. A. Cooper. Influence of increased membrane cholesterol on membrane fluidity and cell function in human red blood cells. *J. Supramol. Struct.* **8**, 413-430 (1978).

13 X. Xu & E. London. The effect of sterol structure on membrane lipid domains reveals how cholesterol can induce lipid domain formation. *Biochemistry* **39**, 843-849 (2000).

14 T. Kolter. A view on sphingolipids and disease. *Chem. Phys. Lipids* **164**, 590-606 (2011).

15 F. M. Platt. Sphingolipid lysosomal storage disorders. *Nature* **510**, 68-75 (2014).

16 S. Schiffmann *et al.* Ceramide synthases and ceramide levels are increased in breast cancer tissue. *Carcinogenesis* **30**, 745-752 (2009).

17 G. Van Echten-Deckert & J. Walter. Sphingolipids: critical players in Alzheimer's disease. *Prog. Lipid Res.* **51**, 378-393 (2012).

18 V. Brinkmann *et al.* Fingolimod (FTY720): discovery and development of an oral drug to treat multiple sclerosis. *Nat. Rev. Drug Discov.* **9**, 883-897 (2010).

19 Y. A. Hannun & L. M. Obeid. Principles of bioactive lipid signalling: lessons from sphingolipids. *Nat. Rev. Mol. Cell Biol.* **9**, 139-150 (2008).

20 J.-S. Won & I. Singh. Sphingolipid signaling and redox regulation. *Free Radic. Biol. Med.* **40**, 1875-1888 (2006).

21 Y. Li, S. Li, X. Qin, W. Hou, H. Dong, L. Yao & L. Xiong. The pleiotropic roles of sphingolipid signaling in autophagy. *Cell Death Dis.* **5**, e1245 (2014).

22 T. Hla & A. J. Dannenberg. Sphingolipid signaling in metabolic disorders. *Cell Metab.* **16**, 420-434 (2012).

23 Y. H. Zeidan & Y. A. Hannun. Translational aspects of sphingolipid metabolism. *Trends Mol. Med.* **13**, 327-336 (2007).

24 E. Bieberich. Ceramide signaling in cancer and stem cells. *Future Lipidol.* **3**, 273-300 (2008).

25 P. Susan. Sphingosine 1-phosphate signalling in mammalian cells. *Biochem. J* **349**, 385-402 (2000).

26 H. Fyrst & J. D. Saba. An update on sphingosine-1-phosphate and other sphingolipid mediators. *Nat. Chem. Biol.* **6**, 489-497 (2010).

27 N. J. Pyne & S. Pyne. Sphingosine 1-phosphate and cancer. *Nat. Rev. Cancer* **10**, 489-503 (2010).

28 A. K. Gardino, S. J. Smerdon & M. B. Yaffe. in *Semin. Cancer Biol.* 173-182 (Elsevier).

29 J. P. Hobson *et al.* Role of the sphingosine-1-phosphate receptor EDG-1 in PDGF-induced cell motility. *Science* **291**, 1800-1803 (2001).

30 E. Miller *et al.* Identification of serum-derived sphingosine-1-phosphate as a small molecule regulator of YAP. *Chem. Biol.* **19**, 955-962 (2012).

31 K. M. Argraves, B. A. Wilkerson & W. S. Argraves. Sphingosine-1-phosphate signaling in vasculogenesis and angiogenesis. *World J. Biol. Chem.* **1**, 291-297 (2010).

32 Y. Takuwa, W. Du, X. Qi, Y. Okamoto, N. Takuwa & K. Yoshioka. Roles of sphingosine-1-phosphate signaling in angiogenesis. *World J. Biol. Chem.* **1**, 298-306 (2010).

33 N. K. Haass, N. Nassif & E. M. Mcgowan. Switching the sphingolipid rheostat in the treatment of diabetes and cancer comorbidity from a problem to an advantage. *BioMed Res. Int.* **2015**, 165105 (2015).

34 J. Newton, S. Lima, M. Maceyka & S. Spiegel. Revisiting the sphingolipid rheostat: evolving concepts in cancer therapy. *Exp. Cell Res.* **2**, 195-200 (2015).

35 C. F. Jessup, C. S. Bonder, S. M. Pitson & T. H. Coates. The sphingolipid rheostat: a potential target for improving pancreatic islet survival and function. *Endocr. Metab. Immune Disord. Drug Targets* **11**, 262-272 (2011).

36 M. Taniguchi *et al.* Regulation of autophagy and its associated cell death by "sphingolipid rheostat": reciprocal role of ceramide and sphingosine 1-phosphate in the mammalian target of rapamycin pathway. *J. Biol. Chem.* **287**, 39898-39910 (2012).

37 A. Honigmann, V. Mueller, H. Ta, A. Schoenle, E. Sezgin, S. W. Hell & C. Eggeling. Scanning STED-FCS reveals spatiotemporal heterogeneity of lipid interaction in the plasma membrane of living cells. *Nat. Commun.* **5**, 5412 (2014).

38 K. Trajkovic *et al.* Ceramide triggers budding of exosome vesicles into multivesicular endosomes. *Science* **319**, 1244-1247 (2008).

39 I. López-Montero, M. Vélez & P. F. Devaux. Surface tension induced by sphingomyelin to ceramide conversion in lipid membranes. *Biochim. Biophys. Acta* **1768**, 553-561 (2007).

40 N. W. Andrews, P. E. Almeida & M. Corrotte. Damage control: cellular mechanisms of plasma membrane repair. *Trends Cell Biol.* **24**, 734-742 (2014).

41 B. X. Wu, V. Rajagopalan, P. L. Roddy, C. J. Clarke & Y. A. Hannun. Identification and characterization of murine mitochondria-associated neutral sphingomyelinase (MA-nSMase), the mammalian sphingomyelin phosphodiesterase 5. *J. Biol. Chem.* **285**, 17993-18002 (2010).

42 K. Hanada, K. Kumagai, S. Yasuda, Y. Miura, M. Kawano, M. Fukasawa & M. Nishijima. Molecular machinery for non-vesicular trafficking of ceramide. *Nature* **426**, 803-809 (2003).

43 G. D'angelo *et al.* Glycosphingolipid synthesis requires FAPP2 transfer of glucosylceramide. *Nature* **449**, 62-67 (2007).

44 T. Yamaji, K. Kumagai, N. Tomishige & K. Hanada. Two sphingolipid transfer proteins, CERT and FAPP2: their roles in sphingolipid metabolism. *IUBMB life* **60**, 511-518 (2008).

45 D. Newrzella & W. Stoffel. Molecular cloning of the acid sphingomyelinase of the mouse and the organization and complete nucleotide sequence of the gene. *Biol. Chem. Hoppe Seyler* **373**, 1233-1238 (1992).

46 S. Tomiuk, K. Hofmann, M. Nix, M. Zumbansen & W. Stoffel. Cloned mammalian neutral sphingomyelinase: Functions in sphingolipid signaling? *Proc. Natl. Acad. Sci. U. S. A.* **95**, 3638-3643 (1998).

47 S. M. Pitson *et al.* Human sphingosine kinase: purification, molecular cloning and characterization of the native and recombinant enzymes. *Biochem. J* **350**, 429-441 (2000).

48 C. J. Clarke, E. A. Cloessner, P. L. Roddy & Y. A. Hannun. Neutral sphingomyelinase 2 (nSMase2) is the primary neutral sphingomyelinase isoform activated by tumour necrosis factor-α in MCF-7 cells. *Biochem. J* **435**, 381-390 (2011).

49 E. Gulbins *et al.* Acid sphingomyelinase-ceramide system mediates effects of antidepressant drugs. *Nat. Med.* **19**, 934-938 (2013).

50 M. Zumbansen & W. Stoffel. Neutral sphingomyelinase 1 deficiency in the mouse causes no lipid storage disease. *Mol. Cell. Biol.* **22**, 3633-3638 (2002).

51 A. Carpinteiro *et al.* Regulation of hematogenous tumor metastasis by acid sphingomyelinase. *EMBO Mol. Med.* **7**, 714-734 (2015).

52 N. H. Petersen *et al.* Transformation-associated changes in sphingolipid metabolism sensitize cells to lysosomal cell death induced by inhibitors of acid sphingomyelinase. *Cancer Cell* **24**, 379-393 (2013).

53 C. Luberto *et al.* Inhibition of tumor necrosis factor-induced cell death in MCF7 by a novel inhibitor of neutral sphingomyelinase. *J. Biol. Chem.* **277**, 41128-41139 (2002).

1.6 FIGURES

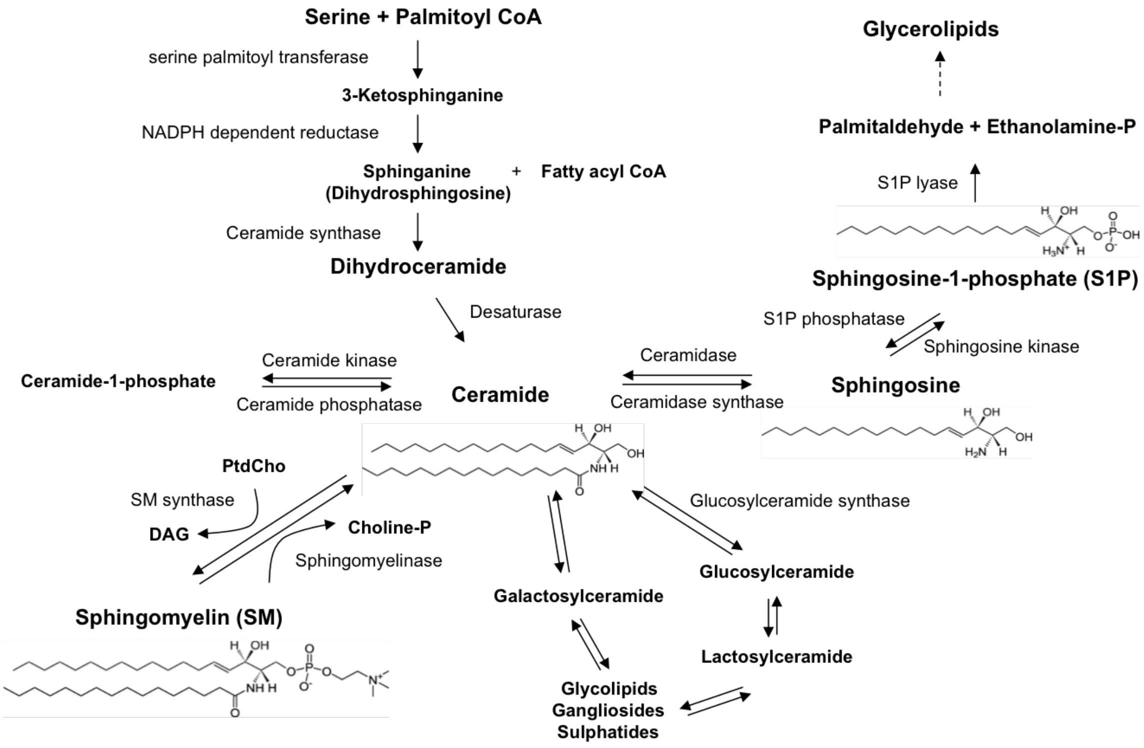

Figure 1.1. Metabolic pathways of sphingolipids.

CHAPTER 2

DEVELOPMENT AND USE OF FLUORESCENT SPHINGOSINES FOR INVESTIGATING SPHINGOLIPID BEHAVIORS[*]

2.1 INTRODUCTION

Sphingolipids and their metabolites serve both as structural components in eukaryotic cell membranes and as bioactive signaling molecules that modulate gene expression, apoptosis, and other critical cellular processes during normal cell function and disease.[1-4] Insight into sphingolipid biosynthesis, transport, and subcellular distribution has been acquired by observing fluorescent sphingolipid analogs within living cells.[5] Sphingolipid derivatives that contain a fluorophore-labeled *N*-acyl fatty acid are often employed to investigate dynamic processes that involve acylated sphingolipids.[5] Fatty acids that contain a polyene fluorophore are especially attractive for this purpose because the structure and behavior of polyene-containing lipids are very similar to the native lipid.[6] However, to study the bioactive, unacylated sphingolipids, sphingosine and sphingosine-1-phosphate, the fluorophore must instead be incorporated into the sphingosine backbone. Studies have confirmed that such fluorescent

---

[*] This chapter features portions of the work that was originally appeared in and has been reprinted with permission from: *Journal of Lipid Research.* Kim, R., Lou, K. & Kraft, M. L. "A new, long-wavelength borondipyrromethene sphingosine for studying sphingolipid dynamics in live cells", *Journal of Lipid Research* **54**, 265-275 (2013).

The publication in the Journal of Lipid Research was coauthored by Raehyun Kim, Kaiyan Lou, and Mary L. Kraft. R.K. characterized the fluorescence properties of the fluorescent sphingolipids, developed the experiment protocol for cell labeling, prepared and analyzed cell samples and cellular lipid samples. K.L. designed and synthesized the fluorescent sphingosines and assisted lipid analysis. M.L.K. planned and designed the experiments.

I thank Sean Sihoon Park for his assistance with the preparation of organelle marker plasmids, Lauren Macur Brousil for her assistance with the TLC separation.

M.L.K. held a 2007 Career Award at the Scientific Interface from the Burroughs Wellcome Fund. This material is based upon work supported by the National Science Foundation under CHE–1058809.

Portions of this work were carried out in the Core Facility in the Carl R. Woese Institute for Genomic Biology and Protein Sciences Facility in the Roy J. Carver Biotechnology Center at the University of Illinois at Urbana-Champaign.

sphingosine analogs can be metabolized to more complex fluorescently labeled sphingolipids in living cells.[7-10] Despite their potential utility, only a limited number of fluorophores, such as pyrene, borondipyrromethene (BODIPY), and nitrobenzo-2-oxa-1,3-diazole (NBD), have been incorporated into the sphingosine backbone.[7-9]

To increase the utility of fluorescent sphingosine analogs for investigating sphingolipid dynamics in living cells, derivatives with a wider range of fluorescence properties must be developed. Lacking in particular is a bioactive fluorescent sphingosine that has neither an excitation maximum that is in the UV range, nor emission that interferes with detecting green fluorescent protein (GFP), the most common genetically encoded fluorescent protein label.[11] A probe with these properties is expected to have the advantages of lower phototoxicity than existing fluorescent sphingosine analogs, and the capability to visualize it in parallel with GFP, which would facilitate assessing sphingolipid colocalization with proteins of interest. For this reason, here we report the synthesis and validation of BODIPY 540 sphingosine, which has maximum excitation at 540 nm, and emission that does not overlap with GFP. In this study, we use fluorescent organelle-specific markers to characterize the distribution of BODIPY 540 sphingosine and its fluorescent metabolites within living cells. We confirm that mammalian cells metabolized BODIPY 540 sphingosine to BODIPY 540 sphingolipids, and also catabolized these fluorescent sphingolipid metabolites. Based on these results, we anticipate that this new fluorescent sphingosine analog will be a valuable tool for investigating the metabolism, trafficking, and signaling of acylated and unacylated sphingolipid species in living cells.

2.2 MATERIALS AND METHODS

2.2.1 Synthesis of BODIPY 540 sphingosine, BODIPY 540 ceramide and BODIPY 540 sphingomyelin standards

BODIPY 540 sphingosine, BODIPY 540 ceramide and BOIDPY 540 sphingomyelin were synthesized as described.[12]

2.2.2 Cell culture

NIH3T3 murine fibroblast cells (ATCC© CRL-1658) were grown in Dulbecco's Modified Eagle Medium (DMEM) with 10% calf serum and 1% penicillin/streptomycin in a 5% CO_2 incubator at 37°C. For colocalization studies, organelle-specific fluorescent fusion proteins were expressed in HEK293 cells due to their ease of transfection. HEK293 cells were grown in DMEM with 10% fetal bovine serum (FBS) and 1% penicillin/streptomycin in a 5% CO2 incubator at 37°C. For microscopy experiments, cells were cultured in 35 mm glass bottom dishes (MatTek, Ashland, MA) or 35 mm plastic dishes for high-end microscopy (ibidi GmbH, München, Germany). For all other experiments, cells were grown in 150 mm cell culture dishes.

2.2.3 Pulse-chase labeling

Cells were incubated with BODIPY 540 sphingosine in OptiMEM supplemented with either 2% calf serum (NIH3T3 murine fibroblast cells) or 2% FBS (HEK293 cells). BODIPY 540 sphingosine was dissolved in ethanol and added to the labeling medium such that the final concentration of BODIPY 540 sphingosine was 1 or 1.25 μM. For pulse labeling, cells were incubated in labeling medium that contained either 1 or 1.25 μM of BODIPY 540 sphingosine for 30 min. After labeling, the medium was removed, and the cells were washed with phosphate buffered saline (PBS) and then cultured in unlabeled growth medium for the specified chase time. For studies of BODIPY 540 sphingosine metabolism, cells were incubated in growth medium that contained 1 μM of BODIPY 540 sphingosine for the specified time.

2.2.4 Lipid extraction

Cells were harvested when they reached 90-100% confluence. Cells were washed with cold PBS, removed from the dish with a scraper, and pelleted by centrifugation. Lipids were extracted using the Bligh and Dyer method.[13] The glycolipids were selectively hydrolyzed by alkaline treatment with sodium hydroxide; this treatment did not hydrolyze the sphingolipids.

2.2.5 TLC

Lipids extracts were dissolved in chloroform-methanol (20 µL, 2:1 v/v), spotted on TLC plates (Silica 60 F254 plates, EMD Chemicals), and developed in a TLC chamber using butanol-acetic acid-water (4.5:1:1 v/v/v) as the solvent. Digital imaging of the TLC plates was performed on a Typhoon 9400 imager (GE Healthcare) using 532 nm laser excitation and 580 nm emission filter to detect the fluorescent spots. Unlabeled lipids were visualized by iodine staining. The BODIPY 540-labeled sphingomyelin, ceramide, and sphingosine were identified by their co-migration with BODIPY 540-labeled sphingolipid standards. Because this solvent system primarily separated the lipid species according to their head groups, which was confirmed by the co-migration of the BODIPY 540 labeled sphingomyelin and ceramide with unlabeled sphingomyelin and ceramide, respectively, in this solvent system, the remaining fluorescent lipid species were identified according to their co-migration with an unlabeled lipid standard.

2.2.6 Glycerophospholipid quantification

For each labeling interval (2 h and 1 d), the total lipid extract obtained from a single labeling experiment was dissolved in chloroform-methanol (2:1 v/v) and divided into two equal portions. One portion of the total lipid extract was subjected to alkaline hydrolysis to remove the glycerolipids; the resulting fraction is referred to as the sphingolipid extract because it contained primarily sphingolipid species. For each labeling time, the total lipid extract and corresponding sphingolipid extract were applied to a TLC plate and separated using butanol-acetic acid-water (4.5:1:1 v/v/v) as the solvent system. For each labeling interval, the amount of BODIPY 540-labeled glycerophospholipids on the TLC plate was assessed by visualizing the spots with a Typhoon 9400 imager (GE Healthcare) using 532 nm laser excitation and 580 nm emission filter and quantifying their fluorescence intensities. To quantify the fraction of the fluorescence that corresponded to glycerolipids, the sum of the fluorescence intensities measured for each spot that corresponded to fluorescent phosphatidylcholine, phosphatidylethanolamine, phosphatidylserine, and phosphatidylinositol was measured using ImageQuant software (GE Healthcare) and divided by the total fluorescence intensities of all of the fluorescent lipid species.

2.2.7 Labeling organelles for colocalization study

For labeling the endoplasmic reticulum (ER), Golgi apparatus, and mitochondria, organelle-specific GFP protein constructs were employed. For ER labeling, HEK293 cells were transfected with pAc-GFPC1-Sec61β (Addgene plasmid 15108)[14] using TransPass D2 transfection reagent (New England BioLabs, Ipswich, MA). For Golgi apparatus and mitochondria labeling, CellLight® Golgi-GFP and CellLight® Mitochondria-GFP (Molecular Probes), respectively, were used according to the manufacturer's protocol. One to two days after transduction, the HEK293 cells were incubated with 1 μM of BODIPY 540 sphingosine for 30 min, followed by a chase in unlabeled medium for approximately 1 day. To label the lysosomes, NIH3T3 mouse fibroblast cells were incubated with OptiMEM containing 2 mg/mL of FITC-dextran (MW 10,000, Sigma-Aldrich) for 30 min. The cells were then cultured for 5 h in unlabeled medium, followed by 30 min in medium that contained 1 μM of BODIPY 540 sphingosine, and finally in unlabeled medium for a 30 min or 16 h chase. To label the nucleus, 2 μL of Hoechest 33342 (Invitrogen) stock solution (10 mg/mL) was added to the growth medium in which the NIH3T3 mouse fibroblast cells were cultured. After 30 min, the medium was replaced with unlabeled medium. After 30 min, the cells were incubated in medium with 1 μM of BODIPY540 sphingosine for 30 min, and then were transferred to unlabeled medium for a 2-day chase.

2.2.8 Confocal laser scanning microscopy

Labeled cells were transferred to phenol red-free OptiMEM supplemented with 2% calf serum (NIH3T3 mouse fibroblast cells) or 2% FBS (HEK293 cells). The labeled cells were observed on a Carl Zeiss LSM 700 confocal microscope with 63 X 1.4 NA oil immersion objective lens at room temperature using a 555 nm laser to excite BODIPY 540, a 488 nm laser to excite GFP and FITC, and a 405 nm laser to excite Hoechst 33342.

2.3 RESULTS

2.3.1 Fluorescence property of BODIPY 540 sphingosine

Characterization of the absorption and fluorescence of BODIPY 540 sphingosine in ethanol (1 μM) demonstrated its absorption and fluorescence emission maxima were 540 nm and 568 nm, respectively (Figure 2.1). Thus, the excitation and emission properties of the analog are similar to BODIPY TMR despite replacing the phenoxy methyl in BODIPY TMR with a sphingosine moiety. The long wavelength emission that is indicative of dimer formation appeared to be negligible in labeled cells.

2.3.2 Cells uptake and metabolize BODIPY 540 sphingosine

We first confirmed that BODIPY 540 sphingosine was internalized by cells and metabolized to more complex fluorescent sphingolipids. Mouse fibroblast cells (NIH3T3) were pulse labeled by incubation with 1.25 μM of BODIPY 540 sphingosine for 30 min at 37°C and transferred to unlabeled medium at 37°C for various chase times before imaging at room temperature. No adverse effect on cell viability was observed during or after labeling. Figure 2.2 shows that the pulse-labeled cells exhibited strong fluorescence, confirming they internalized the BODIPY 540 sphingosine. After a 30 min chase in unlabeled medium, fluorescent tubule-like structures and vesicles of various sizes were observed inside the NIH3T3 mouse fibroblast cells (Figure 2.2A). The edges of these cells did not exhibit strong fluorescence, which indicates that the plasma membrane contained low levels of fluorescent lipid species (Figure 2.2A). Fluorescent vesicles were also observed in NIH3T3 mouse fibroblast cells when the duration of the chase in unlabeled medium increased to 20 h (Figure 2.2B). Although the plasma membrane still appeared to be dim relative to the highly fluorescent intracellular vesicles, which were especially abundant in NIH3T3 mouse fibroblast cells, the clearer fluorescent outline of the cell's perimeter indicates that BODIPY 540 lipid species had incorporated into the plasma membrane (Figure 2.2B). Overall, these observations suggest that the BODIPY 540 sphingosine was metabolized to fluorescent sphingolipids, which were transported to the plasma membrane.

To verify that the fluorescent sphingosine was metabolized fluorescent sphingolipids, NIH3T3 mouse fibroblast cells were cultured in the presence of 1 μM of BODIPY 540 sphingosine for various time intervals, and their lipids were extracted. The glycerolipids in each total lipid extract were removed by base hydrolysis,[15] and the resulting fraction, referred to as the sphingolipid extract because it primarily contained sphingolipids, was separated by TLC. The BODIPY 540-labeled sphingolipids on the TLC plate could be detected with high sensitivity according to their fluorescence. Four fluorescent sphingolipid species, which included BODIPY 540 sphingosine, were detected after a labeling time as short as 2 h (Figure 2.2C). Co-migration with BODIPY 540-labeled sphingolipid standards confirmed that the NIH3T3 mouse fibroblast cells metabolized the fluorescent sphingosine to BODIPY 540-labeled ceramide and sphingomyelin. Because the BODIPY 540-labeled ceramide and sphingomyelin co-migrated with the analogous unlabeled sphingolipid in this solvent system, we identified the remaining fluorescent sphingolipid as BODIPY 540 glucosylceramide due to its co-migration with the unlabeled standard. In addition to these four sphingolipid species, a fifth species, identified as lactosylceramide based on its relative location on the TLC plate,[16] was observed for a labeling period of 1 day. More complex BODIPY 540-labeled glycosphingolipids, such as BODIPY 540 gangliosides, were not visible on the TLC plate. Because unlabeled gangliosides also were not detected on iodine-stained TLC plates, the inability to detect BODIPY 540 gangliosides likely reflects a low level of gangliosides in the NIH3T3 mouse fibroblast cell extracts and not a lack of BODIPY 540 sphingosine incorporation into complex glycosphingolipid species.

Native sphingolipid catabolism yields phosphoethanolamine and the fatty aldehyde trans-2-hexadecenal, which is oxidized to a fatty acid that can be incorporated into glycerolipids.[16-19] Therefore, if the BODIPY 540 sphingolipids were degraded via this pathway, the resulting BODIPY 540 labeled hexadecenal could be oxidized and used to biosynthesize fluorescent glycerolipids. To assess this possibility, sphingolipid extracts and total cellular lipid extracts were isolated from NIH3T3 mouse fibroblast cells that were cultured in the presence of 1 μM of BODIPY 540 sphingosine for 2 h, and the lipid components were separated with TLC. In addition to the BODIPY 540 labeled sphingolipid species observed by TLC separation of the sphingolipid extract, the total cellular lipid extract exhibited three additional fluorescent spots that corresponded to fluorescent glycerophospholipids (Figure 2.2C). Comparison of these migration patterns to those of unlabeled phospholipid standards indicated that two of these components were BODIPY 540 labeled phosphatidylcholine and phosphatidylethanolamine; the third spot was consistent with either BODIPY 540 labeled phosphatidylserine or phosphatidylinositol. Based on the relative intensities of the TLC spots corresponding to unlabeled lipid species, which were visualized by staining the same TLC plate with iodine, the BODIPY 540 fluorophore was incorporated into the major sphingolipid species but was less abundant in the major glycerolipid species after a 2 h labeling period. However, after labeling with 1 μM of BODIPY 540 sphingosine for 1 day, the BODIPY 540 labeled lipids reflected the major lipid species present in the cell extracts. These results suggest that fluorescent sphingolipid degradation followed the native sphingolipid catabolism pathway.

We estimated the fraction of BODIPY 540 that had been incorporated into glycerolipids after labeling NIH3T3 mouse fibroblast cells with 1 μM of BODIPY 540 sphingosine for 2 h and 1 day by measuring the fraction of the total fluorescence on the TLC plate that was produced by spots corresponding to glycerolipid species. After a 2 h labeling period, BODIPY 540 glycerolipids produced approximately 25% of the fluorescence measured in the total lipid extract; after labeling for 1 day, approximately 43% of the fluorescence measured in the total lipid extract was produced by BODIPY 540 glycerolipids. Thus, the BODIPY 540 glycerolipids that resulted from BODIPY 540 sphingolipid catabolism were detectable after a pulse as short as 2 h, and their abundance increased with time. Previous studies have demonstrated that exogenous [^{3}H]-sphingosine is also rapidly degraded by cells and that the amount of the radioactive degradation products increases with time.[20] This suggests that the time-dependent sphingolipid catabolism we observed is a characteristic of sphingosine pulse labeling and was not induced by the presence of the fluorophore.

2.3.3 Subcellular distribution of BODIPY 540 sphingolipids

The studies described above demonstrate that NIH3T3 mouse fibroblast cells metabolized the BODIPY 540 sphingosine to fluorescent sphingolipids and degraded these fluorescent sphingolipids in a manner that was consistent with native sphingolipid catabolism. We performed colocalization studies to confirm that BODIPY 540 sphingosine and its fluorescent metabolites were trafficked through the organelles where sphingolipid biosynthesis primarily occurs. For these experiments, HEK293 cells were used because their high transfectability facilitated the expression of the organelle-specific fluorescent proteins required to assess colocalization. HEK293 cells that expressed the ER or Golgi apparatus markers, GFP-Sec61β[14] or CellLight® Golgi-GFP, respectively, were pulse labeled with 1 μM of BODIPY 540 sphingosine for 30 min, followed by a 30 min or 1 day chase. Confocal microscopy imaging confirmed the fluorescent sphingolipid analogs were located in the ER (Figure 2.3A) and Golgi apparatus (Figure 2.3B) after the 30 min chase. Low colocalization occurred between the fluorescent sphingolipid analog and the ER or Golgi apparatus markers for the 1-day chase (Figure 2.3C and 2.3D, respectively). The transient colocalization of the BODIPY 540 with the ER and Golgi apparatus is consistent with the conversion of BODIPY 540 sphingosine to more complex fluorescent sphingolipids in these organelles and the subsequent transport of the newly synthesized fluorescent sphingolipids to the plasma membrane.[21]

Lysosomes are the subcellular compartment where complex sphingolipids are catabolized to sphingosine,[22,23] which can be reused for the biosynthesis of new sphingolipids, or degraded to nonsphingolipid species.[17,18,24] We investigated whether BODIPY 540 sphingosine or its fluorescent metabolites accumulated in lysosomes by assessing colocalization between the lysosome marker, FITC-dextran,[25] and BODIPY 540. NIH3T3 mouse fibroblast cells were labeled with FITC-dextran, pulse labeled for 30 min with BODIPY 540 sphingosine, and subjected to a 30 min or 16 h chase. Confocal microscopy imaging of these cells demonstrated that low levels of colocalization occurred after a 16 h chase time (Figure 2.4). The lack of BODIPY 540 accumulation in the lysosomes confirms that the fluorescent sphingolipids that reached the lysosomes were promptly degraded, and the resulting fluorescent products were exported from the lysosomes.

We also investigated whether BODIPY 540 sphingosine or its fluorescent metabolites could be detected in the mitochondria or nucleus. We focused on these organelles because sphingolipids and their metabolites have been previously detected within them, and the sphingolipid metabolism that occurs within these organelles plays a major role in modulating cellular function.[2,26-29] For example, internalized fluorescent ceramides are rapidly detected in mitochondria,[29] where ceramide is catabolized to bioactive metabolites that promote the mitochondrial pathway of apoptosis.[27] Figure 2.5A demonstrates that the fluorescent sphingolipid analogs were colocalized with the mitochondria marker, CellLight® mitochondria-GFP, in transfected HEK293 cells that were pulse labeled with BODIPY 540 sphingosine for 30 min and then chased for 30 min in unlabeled medium. Consistent with previous reports,[29] colocalization was not observed after the 1 day chase. Sphingolipids also perform regulatory and structural functions in the nucleus, but their presence and distribution in subnuclear compartments have primarily been identified by biochemical analysis of nuclear extracts.[2] To assess whether the BODIPY 540 sphingosine or its BODIPY 540 labeled metabolites could be detected in the nucleus, we performed colocalization studies between the DNA label, Hoechst 33342, and BODIPY 540 in labeled NIH3T3 mouse fibroblast cells. After labeling the DNA with Hoechst 33342, the cells were pulse labeled for 30 min with BODIPY 540 sphingosine, followed by a chase in unlabeled medium for approximately 2 days. From the en face confocal microscopy image acquired with the plane of focus at approximately the center of the cell (Figure 2.6A, D), small amounts of the BODIPY 540 fluorophore appeared to be in close proximity to a DNA segment in the nucleus. The reconstructed cross-sectional z-stack images acquired along (Figure 2.6B, E) and perpendicular to (Figure 2.6C, F) the DNA segment also indicate that the BODIPY 540 fluorophore was inside the nucleus and adjacent to the DNA segment. Based on the previously reported finding that sphingomyelin is associated with chromatin,[30] the BODIPY 540-labeled molecule associated with the DNA segment is likely BODIPY 540 sphingomyelin. To our knowledge, this is the first time that a fluorescent sphingolipid has been detected in the nucleus of a living cell.

2.3.4 Comparison of BODIPY 540 sphingosine metabolites with BODIPY sphingosine metabolites

Lastly, we compared the metabolic products of BODIPY sphingosine, a fluorescent sphingosine that was previously reported,[8] and BODIPY 540 sphingosine. For this, NIH3T3 mouse fibroblast cells were incubated in the medium that contained 0.75 μM of both fluorescent sphingosines for 1 day, and the total lipids and the sphingolipids were extracted and separated by TLC. The fluorescent lipids were visualized by a fluorescence imager using two different lasers serially (a 532nm laser for BODIPY 540 and then a 488 nm laser for BODIPY) and corresponding emission filters. The overlapped images of BODIPY metabolites and BODIPY 540 metabolites in the total lipid separation (Figure 2.7) showed three spots in common, a couple spots that were unique to BODIPY 540 metabolites, and three spots that were unique to BODIPY metabolites. Comparison of the total lipids with base hydrolyzed lipids (sphingolipids) revealed that the most of the BODIPY 540 metabolites were glycerophospholipids and the majority of the BODIPY metabolites were sphingolipids. Thus, in the presence of both labeled sphingosines, the NIH3T3 mouse fibroblasts preferentially used BODIPY sphingosine for sphingolipid synthesis, and degraded the BODIPY 540 sphingosine, producing BODIPY 540-labeled fatty acids that were incorporated into glycerolipids.

2.4 DISCUSSION

We have verified the efficacy of a new fluorescent sphingosine analog, BODIPY 540 sphingosine, for studying the transport, distribution, and metabolism of sphingolipids within living cells. BODIPY 540 sphingosine enabled imaging unacylated sphingolipids, which cannot be accomplished with the existing sphingolipid analogs that contain a fluorescent fatty acid side chain. Furthermore, unlike previously reported fluorescent sphingosine analogs,[7-9] BODIPY 540 sphingosine can be visualized in parallel with GFP without the use of UV excitation. By exploiting these capabilities, we verified that mammalian cells rapidly internalized BODIPY 540 sphingosine, transported it to the secretory pathway where it was metabolized to more complex fluorescent sphingolipids, and eventually catabolized these fluorescent sphingolipids. The similarity in the pattern of BODIPY 540 sphingosine metabolites and their subcellular distribution to those of the native sphingolipids indicates that the fluorophore did not significantly hinder lipid metabolism or trafficking.

Our finding that BODIPY 540 sphingosine and its metabolites mimicked the analogous native species in living cells is advantageous for using this probe to study dynamic sphingolipid processes but also has implications for its usage. Sphingosine is a bioactive signaling molecule, so consideration must be given to the biological effects that may be induced by labeling with the fluorescent analog. The BODIPY 540 sphingosine concentrations used in this work were substantially higher than the sphingosine concentrations found in human or bovine serum (~20 nM).[31,32] However, NIH3T3 mouse fibroblast cells did not exhibit the changes in morphology or growth rate that are characteristic of sphingosine toxicity during or after BODIPY 540 sphingosine labeling.[33] HEK293 cells were more sensitive to the exogenous sphingosine analog; changes in their morphology occurred during pulse labeling but subsided shortly after transfer to unlabeled chase medium. Previous reports have shown that the effects of exogenous sphingosine depend on the dose per cell and the capacity of the cells to metabolize it,[33] so the adverse effects of labeling sensitive cell lines might be reduced by decreasing the BODIPY 540 sphingosine concentration. Alternatively, for labeling more sensitive cell lines, BODIPY 540 sphingosine may need to be synthetically converted to BODIPY 540 sphingomyelin,[34,35] which would have lower bioactivity[1] and permit visualizing acylated and unacylated sphingolipids in parallel with GFP.

The catabolic capacity of the cells to degrade the BODIPY 540 sphingolipids in a manner consistent with the native sphingolipid catabolism pathway, which resulted in fluorophore incorporation into glycerophospholipid species, also has implications for use of BODIPY 540 sphingosine. This property permits observing the entire sphingolipid catabolism pathway, which could shed light on the cellular mechanisms that underlie sphingolipid homeostasis. However, this catabolism complicates the use of BODIPY 540 sphingosine to visualize the subcellular sphingolipid distribution selectively because some of the fluorescence observed will be produced by glycerolipids. The same problem is encountered with fluorescent sphingolipid analogs that contain a fluorophore-labeled *N*-acyl fatty acid because they are also catabolized to fluorescent fatty acids that are incorporated into glycerolipids.[5] We observed that the incorporation of BODIPY 540 into glycerolipids increased with increasing labeling time, so the fluorescence from nonsphingolipid species can be minimized by limiting the labeling time. In addition, the presence of a second fluorescent sphingosine analog, BODIPY sphingosine, in the medium increased the incorporation of BODIPY 540 into glycerolipids. The irreversible degradation of sphingosine-1-phosphate to fatty acid precursors, which causes the label scrambling we observed, has been shown to increase with increasing sphingosine concentration in the medium.[20,33] Thus, eliminating the presence of other sphingosine analogs and decreasing the BODIPY 540 sphingosine concentration in the labeling media should reduce fluorophore incorporation into glycerolipid species.

Interestingly, more sphingolipids were produced from BODIPY sphingosine than BODIPY 540 sphingosine, whereas the opposite was true for the glycerophospholipids when NIH3T3 mouse fibroblast cells were simultaneously labeled with both fluorescent sphingosine analogs. The different fates of these two fluorescent sphingosine analogs may reflect differences in substrate preferences between the different enzymes that metabolize sphingosine. Sphingosine can be *N*-acylated by ceramide synthases to produce ceramides and further metabolized to complex sphingolipids, or phosphorylated by sphingosine kinases to produce S1P, which is catabolized to a fatty aldehyde that can be eventually incorporated into glycerophospholipids.[16] The finding that more sphingomyelin and glycosphingolipids contained the BODIPY fluorophore suggests that the ceramide synthases in the mouse fibroblasts preferred BODIPY sphingosine to BODIPY 540 sphingosine as a substrate. Because BODIPY 540 sphingosine is longer and has larger fluorophore than BODIPY sphingosine, these findings may suggest that ceramide synthases require tighter coordination to the hydrophobic tail of the sphingosine substrate than sphingosine kinase. Of course, in vitro rate measurements would need to be performed to confirm the substrate specificities of ceramide synthases and sphingosine kinase for these two fluorescent sphingolipid analogs, and subsequent studies would be required to determine how substrate structure affects this selectivity. Nonetheless, the different preferences of the sphingolipid metabolic enzymes for BODIPY sphingosine and BODIPY 540 sphingosine may be useful as selective substrates for determining the activities of the two different sphingosine processing enzymes.

The ability to track unacylated sphingolipid analogs with BODIPY 540 sphingosine opens the door to identifying the subcellular locations where these bioactive molecules encounter their targets. One such unacylated sphingolipid, sphingosine-1-phosphate, stimulates signaling by binding to G protein-coupled receptors on the cell surface.[1,18] Recently, the hypothesis that fundamental cellular processes are regulated by sphingosine-1-phosphate binding to intracellular targets was verified. Specifically, sphingosine-1-phosphate binding to histone deacetylases in the nucleus regulates gene transcription,[28] whereas its binding to the pro-apoptotic effector molecule, BAK, in mitochondria promotes apoptosis.[27] In both cases, the sphingosine-1-phosphate was generated in the organelle where its target resided, and this location determined the effects of this binding on cell function. Efforts to identify additional intracellular targets of unacylated sphingolipids and their mechanisms of action may be facilitated by visualizing the subcellular distributions of BODIPY 540 sphingosine metabolites and GFP-labeled sphingolipid metabolizing enzymes in parallel.

The detection of BODIPY 540 sphingosine metabolites associated with DNA in the nucleus demonstrates the potential to discover new phenomena by metabolic labeling with BODIPY 540 sphingosine. To our knowledge, this is the first observation of fluorescent sphingosine metabolite association with DNA in the nucleus of a living cell, although further studies are required to confirm the BODIPY 540 labeled molecule was BODIPY 540 sphingomyelin. Since their detection in the nucleus decades ago,[36,37] the identities and subnuclear distributions of sphingolipids have been primarily probed by biochemical analysis of isolated nuclei and visualization of sphingolipid-specific functionalized affinity labels.[2,38,39] Additionally, structural and regulatory roles performed by various types of sphingolipids in the nucleus have been identified.[2] Sphingomyelin associates with chromatin and stabilizes DNA and newly synthesized RNA,[39,40] GM1 regulates nuclear calcium concentrations,[38] and nuclear ceramide is involved in proliferation and apoptosis, although the precise mechanisms remain to be established.[41-43] As mentioned above, nuclear sphingosine-1-phosphate regulates gene expression by binding to histone deacetylases, thereby inhibiting histone deacetylation.[28] Despite these discoveries, many aspects of nuclear sphingolipid function remain poorly understood. BODIPY 540 sphingosine may potentially be used to visualize nuclear sphingolipids, which may allow for a better understanding of how various stimuli influence nuclear sphingolipid distribution and the consequences for cell function.

BODIPY 540 sphingosine can be used to monitor the trafficking and metabolism of acylated and unacylated sphingolipids in living cells. Assessment of colocalization between BODIPY 540 sphingolipids and with GFP-labeled proteins of interest will facilitate identifying the subcellular locations where sphingolipids are metabolized or encounter their binding targets.

Such studies can provide new insight into the broad roles of sphingolipids in modulating cellular function.

2.5 REFERENCES

1 Y. A. Hannun & L. M. Obeid. Principles of bioactive lipid signalling: lessons from sphingolipids. *Nat. Rev. Mol. Cell Biol.* **9**, 139-150 (2008).

2 N. C. Lucki & M. B. Sewer. Nuclear sphingolipid metabolism. *Annu. Rev. Physiol.* **74**, 131-151 (2012).

3 T. Kolter. A view on sphingolipids and disease. *Chem. Phys. Lipids* **164**, 590-606 (2011).

4 T. Kolter & K. Sandhoff. Sphingolipid metabolism diseases. *Biochim. Biophys. Acta* **1758**, 2057-2079 (2006).

5 J.-a. M. Rasmussen & A. Hermetter. Chemical synthesis of fluorescent glycero-and sphingolipids. *Prog. Lipid Res.* **47**, 436-460 (2008).

6 L. Kuerschner, C. S. Ejsing, K. Ekroos, A. Shevchenko, K. I. Anderson & C. Thiele. Polyene-lipids: a new tool to image lipids. *Nat. Methods* **2**, 39-45 (2005).

7 P. Ettmayer, A. Billich, T. Baumruker, D. Mechtcheriakova, H. Schmid & P. Nussbaumer. Fluorescence-labeled sphingosines as substrates of sphingosine kinases 1 and 2. *Biorg. Med. Chem. Lett.* **14**, 1555-1558 (2004).

8 C. Peters, A. Billich, M. Ghobrial, K. Högenauer, T. Ullrich & P. Nussbaumer. Synthesis of borondipyrromethene (BODIPY)-labeled sphingosine derivatives by cross-metathesis reaction. *J. Org. Chem.* **72**, 1842-1845 (2007).

9 T. Hakogi, T. Shigenari, S. Katsumura, T. Sano, T. Kohno & Y. Igarashi. Synthesis of fluorescence-labeled sphingosine and sphingosine 1-phosphate; effective tools for sphingosine and sphingosine 1-phosphate behavior. *Biorg. Med. Chem. Lett.* **13**, 661-664 (2003).

10 C. Bode *et al.* Erythrocytes serve as a reservoir for cellular and extracellular sphingosine 1-phosphate. *J. Cell. Biochem.* **109**, 1232-1243 (2010).

11 E. L. Snapp. Fluorescent proteins: a cell biologist's user guide. *Trends Cell Biol.* **19**, 649-655 (2009).

12 R. Kim, K. Lou & M. L. Kraft. A new, long-wavelength borondipyrromethene sphingosine for studying sphingolipid dynamics in live cells. *J. Lipid Res.* **54**, 265-275 (2013).

13 W. J. D. E. G. Bligh. A rapid method of total lipid extraction and purification. *Can. J. Biochem. Physiol.* **37**, 911-917, doi:10.1139/o59-099 (1959).

14 G. K. Voeltz, W. A. Prinz, Y. Shibata, J. M. Rist & T. A. Rapoport. A class of membrane proteins shaping the tubular endoplasmic reticulum. *Cell* **124**, 573-586 (2006).

15 M. C. Sullards & A. H. Merrill. Analysis of sphingosine 1-phosphate, ceramides, and other bioactive sphingolipids by high-performance liquid chromatography-tandem mass spectrometry. *Sci. STKE* **2001**, pl1 (2001).

16 K. Nakahara *et al.* The Sjögren-Larsson syndrome gene encodes a hexadecenal dehydrogenase of the sphingosine 1-phosphate degradation pathway. *Mol. Cell* **46**, 461-471 (2012).

17 P. P. Van Veldhoven & G. P. Mannaerts. Subcellular localization and membrane topology of sphingosine-1-phosphate lyase in rat liver. *J. Biol. Chem.* **266**, 12502-12507 (1991).

18 M. Maceyka, S. Milstien & S. Spiegel. Sphingosine-1-phosphate: the Swiss army knife of sphingolipid signaling. *J. Lipid Res.* **50**, S272-S276 (2009).

19 W. Stoffel & G. Sticht. Metabolism of sphingosine bases, II. Studies on the degradation and transformation of [3-14C]erythro-DL-dihydrosphingosine,[7-3H]erythro-DL-sphingosine,[5-3H]threo-L-dihydrosphingosine and [3-14C;1-3H]erythro-DL-dihydrosphingosine in rat liver. *Hoppe Seylers Z. Physiol. Chem.* **348**, 1345-1351 (1967).

20 L. Riboni, R. Bassi, A. Prinetti, P. Viani & G. Tettamanti. Predominance of the acylation route in the metabolic processing of exogenous sphingosine in neural and extraneural cells in culture. *Biochem. J* **338**, 147-151 (1999).

21 N. Bartke & Y. A. Hannun. Bioactive sphingolipids: metabolism and function. *J. Lipid Res.* **50**, S91-S96 (2009).

22 T. Kolter & K. Sandhoff. Lysosomal degradation of membrane lipids. *FEBS Lett.* **584**, 1700-1712 (2010).

23 H. Schulze, T. Kolter & K. Sandhoff. Principles of lysosomal membrane degradation: Cellular topology and biochemistry of lysosomal lipid degradation. *Biochim. Biophys. Acta* **1793**, 674-683 (2009).

24 K. Kitatani, J. Idkowiak-Baldys & Y. A. Hannun. The sphingolipid salvage pathway in ceramide metabolism and signaling. *Cell. Signal.* **20**, 1010-1018 (2008).

25 S. L. Schmid, R. Fuchs, P. Male & I. Mellman. Two distinct subpopulations of endosomes involved in membrane recycling and transport to lysosomes. *Cell* **52**, 73-83 (1988).

26 D. Ardail *et al.* Occurrence of ceramides and neutral glycolipids with unusual long-chain base composition in purified rat liver mitochondria. *FEBS Lett.* **488**, 160-164 (2001).

27 J. E. Chipuk *et al.* Sphingolipid metabolism cooperates with BAK and BAX to promote the mitochondrial pathway of apoptosis. *Cell* **148**, 988-1000 (2012).

28 N. C. Hait *et al.* Regulation of histone acetylation in the nucleus by sphingosine-1-phosphate. *Science* **325**, 1254-1257 (2009).

29 N. G. Lipsky & R. E. Pagano. Intracellular translocation of fluorescent sphingolipids in cultured fibroblasts: endogenously synthesized sphingomyelin and glucocerebroside analogues pass through the Golgi apparatus en route to the plasma membrane. *J. Cell Biol.* **100**, 27-34 (1985).

30 C. Scassellati *et al.* Intranuclear sphingomyelin is associated with transcriptionally active chromatin and plays a role in nuclear integrity. *Biol. Cell* **102**, 361-375 (2010).

31 S. Ribar, M. Mesarić & M. Bauman. High-performance liquid chromatographic determination of sphinganine and sphingosine in serum and urine of subjects from an endemic nephropathy area in Croatia. *J. Chromatogr. B Biomed. Sci. Appl.* **754**, 511-519 (2001).

32 S. Mathur *et al.* Fumonisin B1 increases serum sphinganine concentration but does not alter serum sphingosine concentration or induce cardiovascular changes in milk-fed calves. *Toxicol. Sci.* **60**, 379-384 (2001).

33 L. Riboni, A. Prinetti, R. Bassi, P. Viani & G. Tettamanti. The effects of exogenous sphingosine on Neuro2a cells are strictly related to the overall capacity of cells to metabolize sphingosine. *J. Biochem.* **124**, 900-904 (1998).

34 T. Y. Ahmad, J. T. Sparrow & J. D. Morrisett. Fluorine-, pyrene-, and nitroxide-labeled sphingomyelin: semi-synthesis and thermotropic properties. *J. Lipid Res.* **26**, 1160-1165 (1985).

35 H.-S. Byun, R. K. Erukulla & R. Bittman. Synthesis of sphingomyelin and ceramide 1-phosphate from ceramide without protection of the allylic hydroxyl group. *J. Org. Chem.* **59**, 6495-6498 (1994).

36 F. A. Manzoli, N. M. Maraldi, L. Cocco, S. Capitani & A. Facchini. Chromatin phospholipids in normal and chronic lymphocytic leukemia lymphocytes. *Cancer Res.* **37**, 843-849 (1977).

37 L. Cocco, N. M. Maraldi, F. A. Manzoli, R. S. Gilmour & A. Lang. Phospholipid interactions in rat liver nuclear matrix. *Biochem. Biophys. Res. Commun.* **96**, 890-898 (1980).

38 R. W. Ledeen & G. Wu. Gangliosides of the nuclear membrane: a crucial locus of cytoprotective modulation. *J. Cell. Biochem.* **97**, 893-903 (2006).

39 E. Albi & M. Magni. The role of intranuclear lipids. *Biol. Cell* **96**, 657-667 (2004).

40 M. Micheli, E. Albi, C. Leray & M. V. Magni. Nuclear sphingomyelin protects RNA from RNase action. *FEBS Lett.* **431**, 443-447 (1998).

41 E. Albi, S. Cataldi, G. Rossi, M. V. Magni, M. Toller, S. Casani & G. Perrella. The nuclear ceramide/diacylglycerol balance depends on the physiological state of thyroid cells and changes during UV-C radiation-induced apoptosis. *Arch. Biochem. Biophys.* **478**, 52-58 (2008).

42 M. Watanabe *et al.* Increase of nuclear ceramide through caspase-3-dependent regulation of the "sphingomyelin cycle" in Fas-induced apoptosis. *Cancer Res.* **64**, 1000-1007 (2004).

43 K. Tsugane, K. Tamiya-Koizumi, M. Nagino, Y. Nimura & S. Yoshida. A possible role of nuclear ceramide and sphingosine in hepatocyte apoptosis in rat liver. *J. Hepatol.* **31**, 8-17 (1999).

2.6 FIGURES

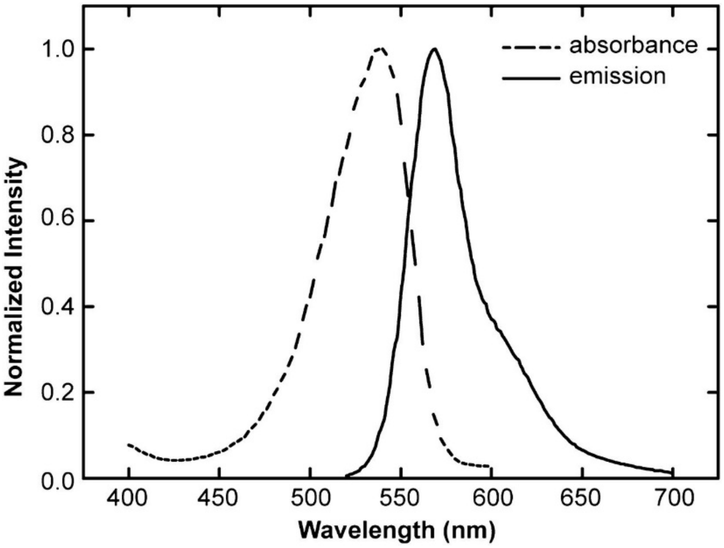

Figure 2.1. Absorbance and emission spectra of BODIPY 540 sphingosine in ethanol. The emission spectrum was collected using a 488 nm excitation.

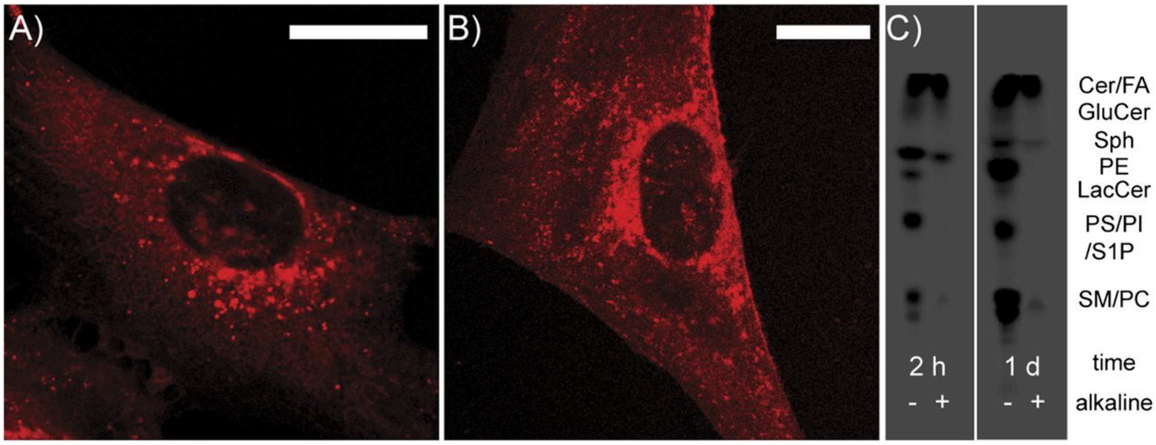

Figure 2.2. Subcellular distribution and metabolism of BODIPY 540 sphingosine in NIH3T3 mouse fibroblast cells. Cells were incubated in 1.25 μM of BODIPY 540 sphingosine for 30 min followed by unlabeled medium for a chase time of 30 min (A) or 20 h (B). Bars = 20 μm. Although the plasma membrane of the cell shown in B is dim in comparison to the highly fluorescent intracellular vesicles that were especially abundant in the NIH3T3 mouse fibroblast cells we examined, the more distinct fluorescent outline at the edge of the cell indicates that BODIPY 540 lipids were present in the plasma membrane. C: Lipid fractions were isolated from cells that were labeled with 1 μM of BODIPY 540 sphingosine for 2 h or 1 day. The total lipid fractions (−) and the lipid fractions subjected to alkaline treatment to remove the glycerolipids (+) were separated by TLC, as described in the Materials and Methods. Images were taken on a fluorescence imager using a 532 nm laser for excitation and a 580 nm emission filter. The identities of the BODIPY 540-labeled species that are indicated to the right of each spot were determined by comparison to lipid standards (see Materials and Methods for details). Cer, ceramide; FA, fatty acids; GluCer, glucosylceramide; LacCer, lactosylceramide; PC, phosphatidylcholine; PE, phosphatidylethanolamine; PI, phosphatidylinositol; PS, phosphatidylserine; SM, sphingomyelin; Sph, sphingosine

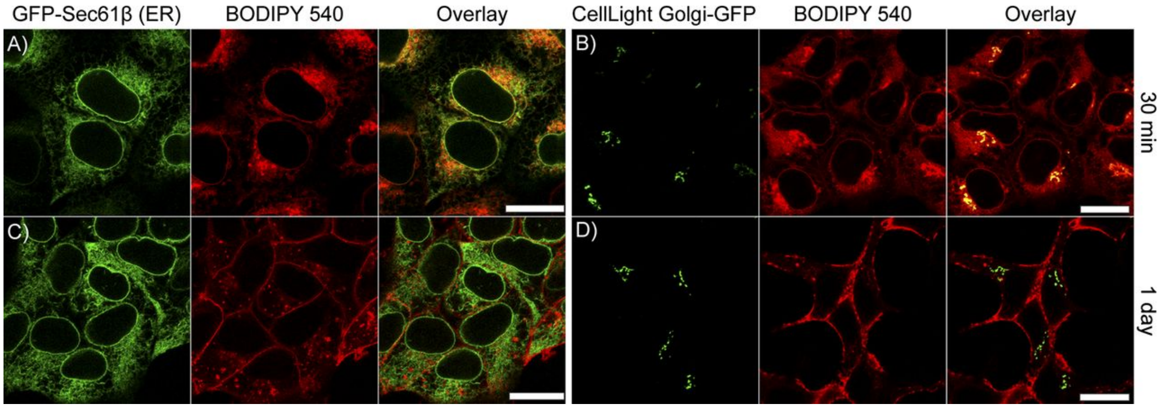

Figure 2.3. Intracellular distribution of BODIPY 540 sphingosine and its fluorescent metabolites. Transfected HEK293 cells that expressed GFP-Sec61β or CellLight® Golgi-GFP were pulse labeled for 30 min in medium containing 1 μM of BODIPY 540 sphingosine and transferred to unlabeled medium for the chase time indicated to the right of the last column. Confocal microscopy imaging was performed on living cells at room temperature. The GFP signal (green) locates the ER (A and C) or Golgi apparatus (B and D). The BODIPY 540 signal (red) shows the subcellular distribution of BODIPY 540 sphingosine and its fluorescent metabolites. The fluorescent outline of each cell, which signifies the incorporation of BODIPY 540 lipids into the plasma membrane, is especially distinct in these images because these HEK293 cells have few highly fluorescent intracellular vesicles. The overlay images show that colocalization between BODIPY 540 and each organelle-specific GPF fusion protein (yellow) occurred when the chase time was 30 min (A and B) but not 1 day (C and D). Bars = 20 μm.

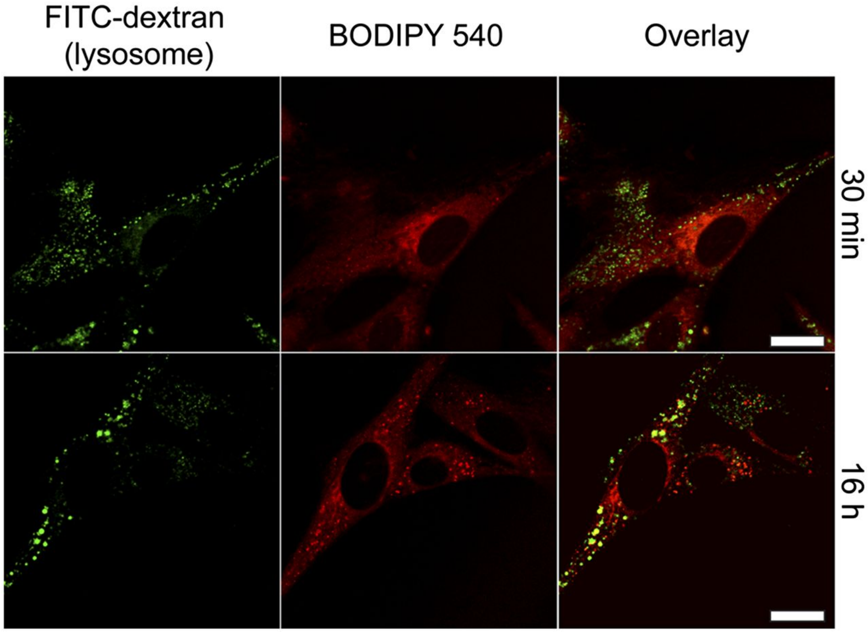

Figure 2.4. Localization of BODIPY 540 sphingolipid analogs in lysosomes. The lysosomes in NIH3T3 mouse fibroblast cells were labeled by incubating the cells for 30 min in medium containing 2 mg/mL of FITC-dextran and then transferring the cells to label-free medium for 5 h. The lysosome-labeled NIH3T3 mouse fibroblast cells were incubated for 30 min in culture medium containing 1 μM of BODIPY 540 sphingosine and transferred to label-free medium for the chase time indicated to the right of the last column. Confocal imaging of the living cells at room temperature revealed the intracellular distribution of the FITC-dextran (green) that labeled the lysosomes and BODIPY 540 sphingosine and its metabolites (red). The overlay images (last column) show that colocalization between BODIPY 540 and FITC-dextran (yellow) did not occur after a 30 min chase but was detectable at low levels after a 16 h chase. Bars = 20 μm.

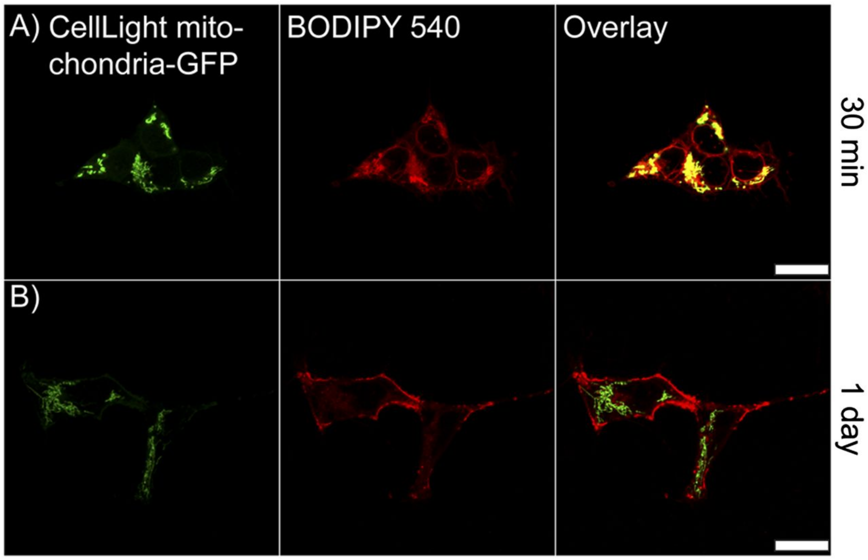

Figure 2.5. Transfected HEK293 cells that expressed CellLight® mitochondria-GFP were pulse labeled for 30 min in medium containing 1 μM of BODIPY 540 sphingosine and transferred to unlabeled medium for 30 min (A) or 1 day (B). The locations of the mitochondria (green) and BODIPY 540 sphingolipid analogs (red) were imaged in living cells at room temperature with confocal microscopy. The overlay images (last column) show that a high amount of colocalization (yellow) occurred between BODIPY 540 and CellLight® mitochondria-GFP 30 min after pulse labeling. In contrast, colocalization of the two fluorescent components was not detected when the chase time increased to 1 day. Bars = 20 μm.

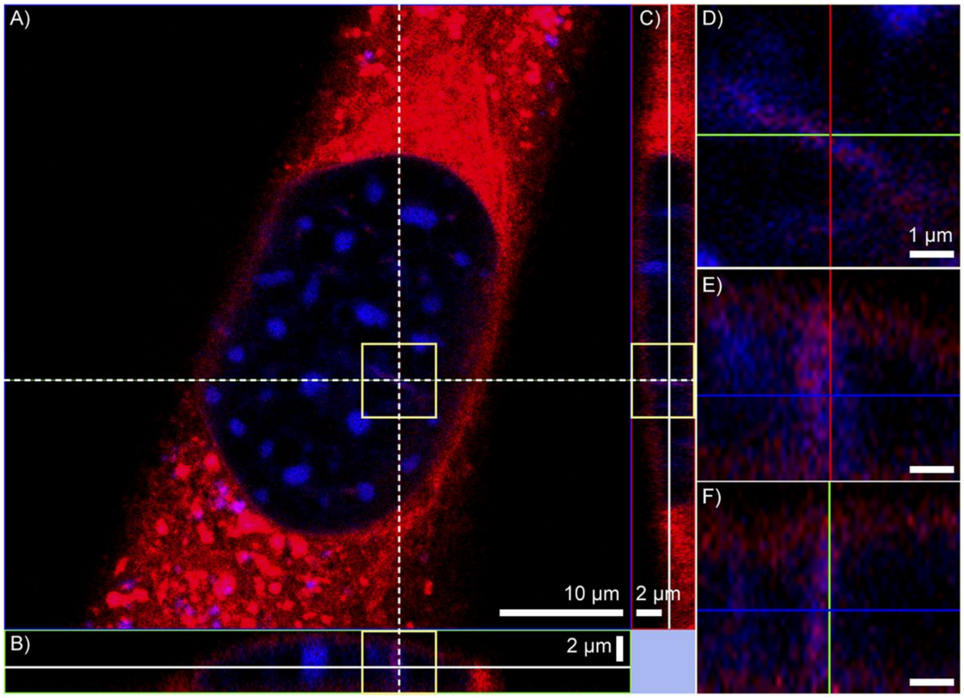

Figure 2.6. Detection of BODIPY 540 sphingosine metabolites in the nucleus. The DNA in NIH3T3 mouse fibroblast cells was labeled with Hoechst 33342 for 30 min. After 30 min in unlabeled medium, the cells were pulse labeled for 30 min with BODIPY 540 sphingosine and chased in unlabeled medium for approximately 2 days. Confocal imaging of the cell shows the subcellular location of DNA (blue) and BODIPY 540 sphingolipid analogs (red). A: An en face confocal microscopy image acquired with the plane of focus at approximately the center of the cell. The horizontal and vertical white dashed lines denote where cross-sectional images were acquired. B: Reconstructed cross-section acquired at the vertical white dashed line shown in A. z-scan step: 0.2 µm. C: Reconstructed cross-section acquired at the horizontal white dashed line shown in A. z-scan step: 0.2 µm. D: Enlargement of the region outlined in yellow in A. E: Enlargement of the region outlined in yellow in B. F: Enlargement of the region outlined in yellow in C. Bars in E and F = 1 µm.

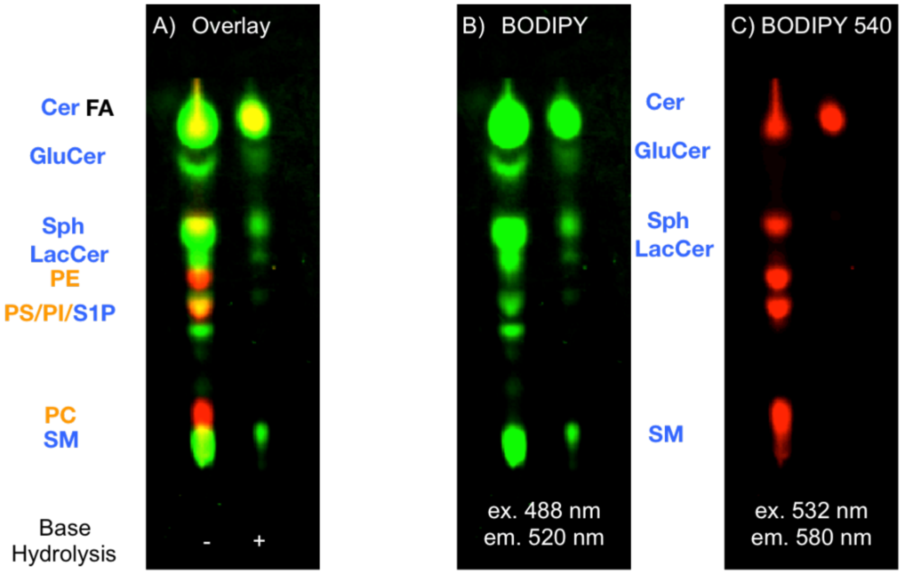

Figure 2.7. Cellular metabolism of BODIPY 540 sphingosine produces more glycerolipids than BODIPY sphingosine metabolism in the cells. NIH3T3 mouse fibroblast cells were incubated with 0.75 μM each of BODIPY sphingosine and BODIPY 540 sphingosine for 1 day. The cellular lipids were extracted and separated by TLC either with or without base hydrolysis, as described in the Materials and Methods. The fluorescent lipids that were separated on the TLC plate were imaged using a fluorescence imager with a 532 nm laser for excitation and a 580 nm emission filter for BODIPY 540 (C), and a 488 nm laser for excitation and a 520 nm emission filter for BODIPY (B). A: overlapped images of BODIPY lipids and BODIPY 540 lipids. B: BODIPY lipids, C: BODIPY 540 lipids.

CHAPTER 3

STABLE ISOTOPE METABOLIC LABELING AS A TOOL TO STUDY SPHINGOLIPID METABOLISM[*]

3.1 INTRODUCTION

Metabolic pathways of sphingolipids are well established despite their complexity. However, we are still far from a complete view of sphingolipid metabolism and behavior. For instance, the generation of ceramides by two different pathways, the de novo pathway and sphingomyelinase-dependent pathway, is well established but the contribution of each of these metabolic pathways to total ceramide synthesis is not known. This issue becomes more difficult and complicated if subcellular locations are also considered in parallel with sphingolipid metabolism, especially because the kinetics of each sphingolipid metabolic reaction are not well known. Considering the significance of sphingolipids in cell signaling and pathological conditions, these questions must be addressed in order to further understand and control sphingolipid behaviors for therapeutic interventions. For this purpose, measurements must be directly performed on the sphingolipids, and not the activities or expression levels of the enzymes that produce them, which, until recently, has not been possible.

Radioactive labeling has been the major tool for understanding sphingolipid metabolism and kinetics. Radiolabels, such as [^{3}H] or [^{14}C], have been incorporated into sphingosine and sphingolipids, as well as serine,[1] which is a substrate for de novo ceramide synthesis, in order to study sphingolipids. [^{14}C] radiolabeling has also been used to investigate sphingomyelin

---

[*] I thank A. Ulanov and Z. Li at the Metabolomics Center for technical assistance on lipidomics study and lipid analysis with LC-MS and LC-MS/MS, and Dr. Kaiyan Lou for the synthesis of ^{15}N-sphingosine and ^{15}N-sphinganine.

This material was partially supported by the National Science Foundation under CHE–1508662.
A portion of this work was carried at the Metabolomics Center in the Roy J. Carver Biotechnology Center at the University of Illinois at Urbana-Champaign.

synthesis.[2] These radioactive labels are incorporated into sphingolipids or phospholipids, producing radioactive sphingolipids following sphingolipid metabolism. Many studies on sphingolipid metabolism have been performed by detecting the only the radiolabeled lipids with thin film chromatography and autoradiography. The high sensitivity of radiolabel detection enables studying the metabolism of even minor lipid species, but such radiolabeling studies do not provide any information about the unlabeled lipids.

Stable isotope labeling has been also used, though less frequently, to study sphingolipid metabolism.[3] Since labeled lipids are analyzed using mass spectrometry, whether performed with or without chromatographic separation, the sensitivity and mass resolution of mass spectrometry has been the limiting factor for using stable isotope labeling for lipid metabolism research. Mass isotopomer distribution analysis (MIDA) has been developed for measuring the synthesis of lipids as well as carbohydrates and proteins.[4] Cholesterol and fatty acid synthesis was investigated using ^{13}C-acetate and MIDA,[5] but improvements in the mass spectrometer's analytic performance was still required.[6] To overcome these limitations in instrumentation and ensure the detection of labeled sphingolipid species, substrates that contain multiple stable isotope labels such as [U-^{13}C, ^{15}N] serine,[7] D$_9$-choline,[8] or ^{13}C-palmitate[9] have been employed. A possible drawback of this multi-label approach is that the incorporation of the labels into sphingolipids can be low because the labeled substrates are also metabolized into other species. Stable-isotope labeled sphingoid backbones, sphingosine and sphinganine, would circumvent this issue and improve incorporation efficiency because, unlike serine, choline, or palmitate, the sphingoid backbones are metabolized mostly to sphingolipids. However, the use of stable-isotope labeled sphingoid bases for sphingolipid metabolism studies has not been reported yet due to the lack of commercially available sphingolipid backbones that are labeled with stable isotopes, and perhaps also due to the limited ability of mass spectrometers suitable for analyzing metabolic products.

Recent improvement in mass spectrometry enables distinguishing lipid species with mass differences less than 1 Da, opening tremendous opportunities for lipid research. A lipidomics approach, an -omics approach analogous to genomics and proteomics, is already gaining attention from the scientific community, and has demonstrated the capability of obtaining comprehensive and meaningful data on lipids. For instance, differences in lipid composition before and after epithelial-to-mesenchymal transition was characterized using a shotgun lipidomics analysis.[10] The same group also reported the quantitative lipidomics analysis of the lipids in the influenza viral envelope and the host cells,[11] which revealed the influenza virus envelope contained more sphingolipids and cholesterol than the donor cell membrane. However, lipidomics approaches that do not employ any isotope labels are unable to answer questions concerning the dynamics or kinetics of lipid metabolism.

Here I set out to use stable isotope labeled sphingoid bases to metabolically label sphingolipids in cells. Prior to metabolic labeling, the sphingolipids of unlabeled NIH3T3 mouse fibroblast cells were profiled by lipidomics analysis using LC-MS/MS. Then, NIH3T3 mouse fibroblast cells were metabolically labeled with ^{15}N-sphingoid bases and ^{13}C-fatty acids, which were incorporated into their cellular sphingolipids, for various time intervals. The resulting cellular lipids were analyzed with LC-MS or LC-MS/MS to assess the production of stable isotope-labeled sphingolipids as a function of labeling time. This study indicates that stable isotope labeling in combination with the improved mass spectrometry can be a powerful tool for lipid metabolism research that exploits both the label's specificity and the comprehensive dataset produced by lipidomics analysis.

3.2 MATERIALS AND METHODS

3.2.1 Materials

^{15}N-sphingosine and ^{15}N-sphinganine were synthesized as previously reported.[12] ^{13}C-algal lipid mix was purchased from Cambridge Isotope Laboratories, Inc. (Tewksbury, MA).

$^{13}C_{18}$-stearic acid (99% atom% ^{13}C) and defatted bovine serum albumin (BSA) was purchased from Sigma-Aldrich (Saint Louis, MO).

3.2.2 Cell culture

NIH3T3 mouse fibroblast cells (ATCC CRL-1658^{TM}) were grown in Dulbecco's Modified Eagle Medium (DMEM) supplemented with calf serum (10% final concentration in medium) and penicillin/streptomycin (1%) at 37°C in 5% CO_2.

3.2.3 Preparation of ^{14}N-sphingoid base, ^{15}N-sphingoid base, and ^{13}C-fatty acid stock solutions

Unlabeled (natural abundance) sphingoid bases, referred to as ^{14}N-sphingoid bases, and ^{15}N-sphingoid bases were each separately dissolved in DMSO to make separate 6 mM stock solutions. The stock solutions were filtered through a sterile 0.2 μm PTFE syringe filter unit, aliquoted and stored at -20°C. ^{13}C-fatty acid mixture were prepared as previously described[13] by dissolving 13.3 mg of ^{13}C-algal lipid mix and 3.3 mg ^{13}C-stearic acid in 750 μL DMSO followed by filtering through a 0.2 μm PTFE syringe filter unit. Then the ^{13}C-fatty acids in DMSO were complexed with 250 μL of 125 mg/mL filtered defatted BSA for efficient delivery to the cells. The resulting solution was vortexed, sonicated for 10-15 min, and then stored at 4°C until labeling (up to a week). When used, the solution was warmed, vortexed, and sonicated for 10-15 min prior to use. The concentration of this ^{13}C stock solution is 16.6 mg/mL or approximately 55.6 mM.[13]

3.2.4 Metabolic Labeling

The cells were seeded in a 100 mm dish with 10 mL of the normal growth media. As a pre-labeling step, ^{14}N-sphingoid bases were added to the cell culture media to produce a final concentration of 3 μM on a daily basis for 2 days. On the third day, the medium was exchanged for fresh growth medium that contained the same concentration (3 μM) of ^{14}N-sphingoid bases. For the labeling step, labeling media were prepared by adding stock solutions of ^{15}N-sphingoid bases and ^{13}C-fatty acids in DMEM supplemented with 1% calf serum (final concentration) and

10% charcoal stripped FBS (Gibco). The final concentrations of ^{15}N-sphingoid bases and ^{13}C-fatty acids in the labeling media were 3 µM and 215 µM respectively. The cells were washed with DPBS and then were cultured in the labeling media for various time intervals. After the labeling, the cells were detached from the dishes using trypsin/EDTA, pelleted by centrifugation, washed with DPBS, and stored as pellets at -20°C.

3.2.5 Lipid extraction

Cellular lipids were extracted following Bligh and Dyer method with slight modification[14] as described previously.[13] The pelleted cells were suspended in 0.75 mL of water (the residual water in the pellet makes up approximately to 0.8 mL). Then 2 mL of methanol and 1 mL of chloroform were added to the mixture, and the solution was vortexed thoroughly, sonicated for 30-60 sec, and then allowed to sit for several hours at room temperature. The resulting solution was centrifuged at 1,811 g for 5 min. The supernatant was decanted into a new glass vial, 1 mL of chloroform and 1 mL of water was added, and the solution was vortexed hard. Centrifugation at 1,811g for 5 min resulted in a biphasic solution. The lower chloroform layer was collected, transferred into a new glass vial, and dried under nitrogen gas stream. The resulting lipids were stored at -20°C until LC-MS analysis.

3.2.6 LC-MS analysis

The extracted cellular lipids were analyzed using Thermo Q-Exactive hybrid quadruple Orbitrap mass spectrometer after separation with an Ultimate 3000 HPLC system. Separation was performed either with a Phenomenex Gemini 3u C6-Phenyl 110A column (2 × 100 mm) using methanol at a flow rate of 300 µL/min, or a Thermo Accucore C18 LC column (2.1 × 150 mm) using two mobile phases (mobile phase A: 60% ACN, 10 mM ammonia formate, 0.1% formic acid, mobile phasee B: 90% isopropanol, 10% acetonitrile, 10 mM ammonia formate, 0.1% formic acid) in gradient at a flow rate of 400 µL/min. The *m*/*z* was scanned in the range of 230-1600. The resolution of the mass spectrometry (R) was 70,000. For lipidomics analysis of the cellular sphingolipids from unlabeled NIH3T3 mouse fibroblast cells, the resulting LC-

MS/MS data of the unlabeled cellular lipids were analyzed by LipidSearch (Thermo Fisher Scientific). The amount of each species was measured by first identifying the retention time for C_{16}-SM and C_{16}-ceramide, and then obtaining the mass peak intensity of corresponding *m*/*z* values at the retention time.

3.3 RESULTS

3.3.1 Profiling sphingolipids in NIH3T3 murine fibroblast cellular lipids

Cellular sphingolipids extracted from unlabeled NIH3T3 mouse fibroblast were first profiled. Lipidomics analysis revealed that palmitoyl sphingomyelin (C_{16}-SM) was the dominant sphingolipid species in NIH3T3 mouse fibroblasts (Figure 3.1 and Table 3.1). The level of C_{16}-SM was about 10 times higher than the second most abundant sphingolipid, C_{16}-glucosylceramide. This lipidomics analysis indicates that palmitic acid or palmitoyl CoA is the most favorable substrate for *N*-acylation of the sphingoid base for sphingolipid production in NIH3T3 mouse fibroblast cells. Therefore, the subsequent metabolic labeling analysis focused on C_{16}-SM and its upstream lipid species, C_{16}-ceramide.

3.3.2 Detection and identification of labeled sphingolipids

The cells were labeled with 6 μM of ^{15}N-sphingoid bases and 215 μM of ^{13}C-fatty acids for various time after pre-labeling the cells with 3 μM of ^{14}N-sphingid bases for 3 days. Pre-labeling was performed to ensure that the cells would be able to process the relatively high levels of exogenous sphingoid bases. Metabolic labeling with ^{15}N-sphingoid bases and ^{13}C-fatty acids permitted the incorporation of two different rare stable isotopes, ^{15}N and ^{13}C, into the cellular sphingolipids' sphingoid backbones and fatty acyl chains, respectively.

High-resolution mass spectrometry allowed detection of both non-labeled and ^{15}N and ^{13}C-fatty acid labeled C_{16}-SM ($^{15}N^{13}C_{16}$ C_{16}-SM) with mass error of less than 0.0035 from the calculated value. However, C_{16}-SM labeled with either ^{15}N-sphingoid or ^{13}C-fatty acids showed a much higher mass error (0.006-0.009) from the theoretical value. We reasoned that this peak with higher error was due to the presence of two unresolved peaks, one from ^{15}N-labeled C_{16}-SM ($^{15}N^{12}C_{16}$ C_{16}-SM), and the other from C_{16}-SM with only one ^{13}C ($^{14}N^{13}C_1$ C_{16}-SM); the natural occurrence of $^{14}N^{13}C_1$ C_{16}-SM in an unlabeled sample is 0.422 time that of $^{14}N^{12}C_{16}$ C_{16}-SM. This altered the *m*/*z* value of the peak such that it was closer to that of $^{14}N^{13}C_1$ C_{16}-SM (theoretical *m*/*z* 704.5788) for short labeling periods and closer to the *m*/*z* of $^{15}N^{12}C_{16}$ C_{16}-SM (theoretical *m*/*z* 704.5724) for longer labeling periods. Therefore, the abundance of ^{15}N-labeled C_{16}-SM was calculated by assuming that the observed mass peak consisted of two Gaussian peaks from the two different C_{16}-SM, $^{14}N^{13}C_1$ C_{16}-SM and $^{15}N^{12}C_{16}$ C_{16}-SM, superimposed on top of one another. This assumption was also made to calculate the abundance of $^{14}N^{13}C_{16}$ C_{16}-SM ($^{14}N^{13}C_{16}$ C_{16}-SM vs. $^{15}N^{13}C_{15}{}^{12}C_1$ C_{16}-SM). C_{16}-ceramide species were also detected in parallel with the C_{16}-SM isotopologues. Again, the mass error of C_{16}-ceramide labeled with only one of the two rare isotopes was higher (0.005-0.008) than unlabeled sphingomyelin and $^{15}N^{13}C_{16}$ C_{16}-SM (0.0025). Therefore, the same assumption was used to calculate the $^{15}N^{12}C_{16}$ C_{16}-ceramide and $^{14}N^{13}C_{16}$ C_{16}-ceramide abundances. The list of *m*/*z* values for identifying labeled and unlabeled C_{16}-ceramide and C_{16}-SM are listed in Table 3.2.

3.3.3 Incorporation of ^{15}N-sphingoid and ^{13}C-fatty acids into C_{16}-ceramide and C_{16}-SM

The incorporation of ^{15}N-sphingoid bases into C_{16}-ceramide and C_{16}-SM were evaluated and the results are shown in Figure 3.2. The incorporation of ^{15}N-sphingoid bases into C_{16}-ceramide increased until it reached a maximum at some time between 4-8 hours and then decreased (Figure 3.2A) while incorporation into SM increased continuously with time over the course of the pulse labeling experiment (Figure 3.2B). These general trends of incorporation into ceramide and SM were similar to the results reported for radiolabeling even though the time point when the maximum incorporation was reached would vary depending on the concentration of the label and the cell types.[15]

The incorporation of ^{13}C-fatty acids into C_{16}-ceramide and C_{16}-SM were also determined, as shown in Figure 3.3. The incorporation of ^{13}C-fatty acids into C_{16}-ceramide increased for the first 4 h, and then reached a plateau (Figure 3.3A). The incorporation of ^{13}C-fatty acids into C_{16}-SM increased continuously during the 24 h labeling interval (Figure 3.3B), similar to ^{15}N-sphingoid incorporation into C_{16}-SM.

3.3.4 Comparison of labeled and total C_{16}-ceramide and C_{16}-SM levels

Next, the levels of labeled and total C_{16}-ceramide and C_{16}-SM were compared (Figure 3.4). SM is generated from ceramide, therefore when new SM synthesis increases, the increase in SM levels should be accompanied by a decrease in ceramide levels. For both the incorporation of ^{15}N-sphingoid bases and ^{13}C-fatty acids into C_{16}-SM and C_{16}-ceramide, the SM/ceramide ratio increased with labeling time (Figure 3.4A and B).

Prior to metabolic labeling, the cellular SM levels were significantly higher than the cellular ceramide levels. However, the addition of ^{15}N-sphingoid bases would increase the total level of sphingoid bases in the cells, and subsequently ceramide synthesis based on the sphingolipid metabolic pathway, which might trigger cell cycle arrest and apoptosis[16] unless the newly synthesized ceramide was rapidly converted to SM. Therefore, the total (labeled and unlabeled) SM to ceramide ratio was calculated at different labeling times. The ratio of total SM to ceramide rapidly decreased until it reached a minimum at 4 h of labeling (Figure 3.4C), which corresponds to the labeling time when the isotope-labeled ceramide levels reached a maximum, and then increased continuously after 8 h.

3.3.5 The effect of ^{13}C-fatty acid labeling on ^{15}N-sphingoid labeling efficiency

Lastly, we evaluated whether the addition of ^{13}C-fatty acids affected the efficiency of incorporating ^{15}N-sphingoid bases into the cellular sphingolipids. The cells were metabolically labeled using only ^{15}N-sphingoids for 4 h or 24 h, at which point the lipids were extracted and subjected to LC-MS. Then the incorporation of ^{15}N-sphingoid bases into C_{16}-ceramide in the absence of ^{13}C-fatty acids was compared to the incorporation obtained when metabolic labeling was performed with ^{13}C-fatty acids (Figure 3.5A). No difference in ^{15}N-sphingoid base incorporation into C_{16}-ceramide and C_{16}-SM was detected after labeling for 4 h labeling with and without ^{13}C-fatty acids. For the 24 h labeling interval, the incorporation of ^{15}N-sphingoid bases into SM was similar in the presence or absence of fatty acids, but more ceramide contained the ^{15}N-sphingoid bases when ^{13}C-fatty acids were added during the labeling.

The ^{15}N-labeled SM/ceramide ratio and the total SM/ceramide ratios with and without ^{13}C-fatty acids were also compared (Figure 3.5B). After labeling for 4 h, the difference between the SM/ceramide ratios measured for labeling performed with and without ^{13}C-fatty acids was not significant. However, after 24 h of labeling, both the ^{15}N-labeled SM/ceramide ratio and the total SM/ceramide ratio were much higher when the labeling was performed without ^{13}C-fatty acids.

3.4 DISCUSSION

Thanks to recent improvements in mass spectrometry, stable isotope labeling now has great potential as a tool that may substitute for radiolabeling for studies of lipid metabolism. A limited number of reported studies have employed stable isotope labeling for sphingolipid research thus far.[7-9] Here, we used ^{15}N-labeled sphingoid bases and ^{13}C-fatty acids to selectively label sphingolipids, and confirmed the feasibility of this metabolic labeling strategy. Even though ^{15}N-sphingoid bases would be an obvious choice for sphingolipid labeling, their use has only been reported by our group, likely because they are not commercially available.

For comparison to metabolically labeled cells, lipidomics analysis of the sphingolipids was performed on unlabeled cell samples. The lipidomics analysis of the lipids extracted from unlabeled NIH3T3 mouse fibroblast cells showed that the majority of the sphingolipids, specifically about 60% of all sphingolipids in NIH3T3 mouse fibroblast cells, was C_{16}-SM. This is consistent with the observation that C_{16}-ceramide, the precursor of C_{16}-SM, is a major ceramide species found in mammalian cells. Despite this, under normal conditions, the levels of CerS5 and CerS6 are usually low in human tissues.[17] Hence, we introduced pre-labeling step to prime the cells so that they would be capable of processing high levels of sphingoid bases during the subsequent stable isotope labeling step. Because C_{16}-SM was the major sphingolipid species found in the NIH3T3 mouse fibroblast cells and C_{16}-ceramide is its precursor, our subsequent analyses focused on C_{16}-SM and C_{16}-ceramide.

High mass resolution mass spectrometry (R=70,000) combined with HPLC allowed the detection of unlabeled and fully labeled (containing both ^{15}N-sphingoid and ^{13}C-fatty acid) C_{16}-SM with very little mass error. Although this high mass resolution is significant progress for lipid studies, two peaks within 0.00632 *m*/*z*, which is the difference between ^{13}C and ^{15}N, still could not be resolved. To address this issue, the two unresolved mass peaks were both assumed to have Gaussian profiles and to be superimposed on top of one another, resulting in a single unresolved peak located between their two *m*/*z* values. Though additional studies would be necessary to definitively verify this assumption, this approximation seems to be more accurate than the alternative approach in which terrestrial abundances of the rare isotope are used to estimate the contribution of each isotopologue to the unresolved mass peak. For example, after a short labeling time (30 min), the portion of ^{15}N-sphingoid-labeled C_{16}-SM was so low that subtraction of the portion of naturally occurring C_{16}-SM with one ^{13}C that was estimated from standard rare isotope abundances (0.422) gave negative incorporation of ^{15}N, which is not possible. For longer labeling time, however, the incorporation that was calculated by assuming that the peaks from the two isotopologues were Gaussian and superimposed gave similar incorporation, within 5% difference, of the ^{15}N incorporation that was calculated by subtracting the portion of C_{16}-SM that naturally contained one ^{13}C. The same principle was also applied to assess the label incorporation into other species. The peaks from $^{14}N^{13}C_{16}$ C_{16}-SM (or ceramide) and $^{15}N^{13}C_{15}{}^{12}C_1$ C_{16}-SM (or ceramide) were also assumed to be Gaussian and superimposed, although whether the cells can produce palmitate or palmitoyl CoA with only fifteen ^{13}C from the^{13}C-algal lipid mix is not known. Additional analysis of the ^{13}C-algal lipid mix with LC-MS/MS would be necessary to assess whether the algal lipid mixture contained $^{12}C_1{}^{13}C_{15}$-palmitic acid.

It is also possible that another isobaric lipid eluted at the same retention time as C_{16}-SM. These possibilities should be evaluated with consideration that different numbers of rare isotopes might be incorporated to the candidate lipids.

The incorporation of ^{15}N-sphingoids into C_{16}-ceramide increased rapidly then slowly decreased while the incorporation into C_{16}-SM increased continuously over labeling time. Similar patterns were shown in the literature with radioactive ^{3}H-sphingoids,[15] which is not surprising since these labeled sphingoid bases are chemically identical to the unlabeled species despite potential differences in the concentration of the labels and the cell types used in these studies. However, the unlabeled lipid species can be detected only when stable isotope labeling and mass spectrometry are employed. For the experiments described herein, about 60% of the C_{16}-SM and 40% of the C_{16}-ceramide would not have been detected if we had employed the same concentration of radioactive labels, assuming that it is possible, to label NIH3T3 mouse fibroblast cells and used thin film chromatography and autoradiography for detection.

^{13}C-fatty acid incorporation followed a trend that was fairly similar to ^{15}N-sphingoid base incorporation. The most noticeable difference was observed for label incorporation into C_{16}-ceramide when longer labeling times were employed. While ^{15}N incorporation into ceramide reached a maximum and then decreased, ^{13}C incorporation instead reached a plateau and did not decrease. This could be due to the differences in the amount of each label that was available to the cells over time. The source of ^{13}C-fatty acids used for labeling was a ^{13}C-algal lipid mix that was complexed with defatted albumin. Algal lipids consist of triacylglycerols as well as free fatty acids.[18] Therefore, the triacylglycerols would be able to further provide ^{13}C-palmitate for labeling through hydrolysis even if the free ^{13}C-palmitate from the algal lipid mix is exhausted. On the other hand, the ^{15}N-sphingoid bases would enter the cells through passive diffusion, as shown with a radioactive sphingosine,[19] mix with the endogenous pool of sphingoid bases and be used for ceramide synthesis immediately. As a result, ^{15}N-sphingoid bases would be exhausted faster than ^{13}C-palmitate for labeling sphingolipids. C_{16}-ceramide with an unlabeled sphingoid can be generated by de novo synthesis from serine and palmitoyl CoA or the recycling pathway from the catabolism of unlabeled sphingolipids. Therefore, the decrease in ^{15}N incorporation into C_{16}-ceramide as the labeling time increases past 4 h likely coincides with an increase in the conversion of unlabeled sphingoid bases to C_{16}-ceramide. The extent that the de novo sphingolipid biosynthetic pathway and the salvage pathway contributed to the generation of unlabeled ceramide is presently unknown. However, careful design of the labeling strategy would allow this aspect of sphingolipid metabolism to be addressed.

The addition of ^{13}C-fatty acids to the medium significantly lowered the ratio of both ^{15}N-labeled SM to ceramide and unlabeled (total) SM to ceramide. Given that one molecule of the sphingoid base and one molecule of palmitic acid is required to produce one molecule of ceramide, fatty acid addition may promote ceramide production by ensuring sufficient levels of the fatty acid starting material are available. Alternatively, some components in the ^{13}C-algal lipid mix may downregulate SM synthesis or upregulate ceramide generation. Exogenous palmitate is reported to increase ceramide synthesis and decrease SM levels in C2C12 myotubes, suggesting that palmitate may activate sphingomyelinases that convert SM to ceramide.[20] The palmitate (or palmitic acid) or some other fatty acids in or produced from the lipid mixture may have the same effect in NIH3T3 mouse fibroblast cells. One other possibility is that the ^{13}C-triacylglycerols, other neutral lipids in the ^{13}C algal lipid mixture, or their metabolic products may compete with ceramide for a phosphocholine head group. SM is generated by transferring a phosphocholine head group from PC to ceramide, producing diacylglycerol (DAG). Because the ^{13}C-triacylglycerols are catabolized to fatty acids that are incorporated into both glycerophospholipids as well as sphingolipids, the addition of the ^{13}C-fatty acid mixture in parallel with the ^{15}N-sphingoid bases may increase the need for phosphocholine in the cells. This competition for phosphocholine may slow down the conversion of ceramide to SM but further investigation would be necessary to confirm it.

In conclusion, this work demonstrates that stable isotope labeling in conjunction with LC-MS analysis has great potential for sphingolipid metabolism studies, providing comprehensive information. The metabolic labeling of cells with ^{15}N-sphingoid bases and ^{13}C-fatty acids are useful tools to understand sphingolipid behavior. In contrast to traditional radiolabeling, this new method enables the measurement of unlabeled sphingolipid species as well as labeled sphingolipids. By combining multiple stable isotope labels and carefully designing the experimental conditions, new information about sphingolipid metabolism and behavior that could not previously been obtained is now within reach.

3.5 REFERENCES

1 E. R. Smith & A. H. Merrill. Differential roles of de novo sphingolipid biosynthesis and turnover in the" burst" of free sphingosine and sphinganine, and their 1-phosphates and N-acyl-derivatives, that occurs upon changing the medium of cells in culture. *J. Biol. Chem.* **270**, 18749-18758 (1995).

2 C. M. Eppler, B. Malewicz, H. M. Jenkin & W. J. Baumann. Phosphatidylcholine as the choline donor in sphingomyelin synthesis. *Lipids* **22**, 351-357 (1987).

3 N. A. Rana, A. Singh, M. Del Poeta & Y. A. Hannun. in *Bioactive Sphingolipids in Cancer Biology and Therapy* 313-338 (Springer, 2015).

4 M. Hellerstein & R. Neese. Mass isotopomer distribution analysis: a technique for measuring biosynthesis and turnover of polymers. *Am. J. Physiol. Endocrinol. Metab.* **263**, E988-1001 (1992).

5 W. P. Lee. in *Dietary Fats, Lipids, Hormones, and Tumorigenesis* 95-114 (Springer, 1996).

6 M. K. Hellerstein & R. A. Neese. Mass isotopomer distribution analysis at eight years: theoretical, analytic, and experimental considerations. *Am. J. Physiol. Endocrinol. Metab.* **276**, E1146-E1170 (1999).

7 E. V. Berdyshev, I. A. Gorshkova, P. Usatyuk, Y. Zhao, B. Saatian, W. Hubbard & V. Natarajan. De novo biosynthesis of dihydrosphingosine-1-phosphate by sphingosine kinase 1 in mammalian cells. *Cell. Signal.* **18**, 1779-1792 (2006).

8 R. Schifferer, G. Liebisch, S. Bandulik, T. Langmann, A. Dada & G. Schmitz. ApoA-I induces a preferential efflux of monounsaturated phosphatidylcholine and medium chain sphingomyelin species from a cellular pool distinct from HDL(3) mediated phospholipid efflux. *Biochim. Biophys. Acta* **1771**, 853-863 (2007).

9 A. U. Blachnio-Zabielska, X. M. T. Persson, C. Koutsari, P. Zabielski & M. D. Jensen. A liquid chromatography/tandem mass spectrometry method for measuring the in vivo incorporation of plasma free fatty acids into intramyocellular ceramides in humans. *Rapid Commun. Mass Spectrom.* **26**, 1134-1140 (2012).

10 J. L. Sampaio, M. J. Gerl, C. Klose, C. S. Ejsing, H. Beug, K. Simons & A. Shevchenko. Membrane lipidome of an epithelial cell line. *Proc. Natl. Acad. Sci. U. S. A.* **108**, 1903-1907 (2011).

11 M. J. Gerl *et al.* Quantitative analysis of the lipidomes of the influenza virus envelope and MDCK cell apical membrane. *J. Cell Biol.* **196**, 213-221 (2012).

12 J. F. Frisz *et al.* Direct chemical evidence for sphingolipid domains in the plasma membranes of fibroblasts. *Proc. Natl. Acad. Sci. U. S. A.* **110**, E613-E622 (2013).

13 H. A. Klitzing, P. K. Weber & M. L. Kraft. Secondary ion mass spectrometry imaging of biological membranes at high spatial resolution. *Methods Mol. Biol.* **950**, 483-501 (2013).

14 W. J. D. E. G. Bligh. A rapid method of total lipid extraction and purification. *Can. J. Biochem. Physiol.* **37**, 911-917, doi:10.1139/o59-099 (1959).

15 M. Fukasawa, M. Nishijima & K. Hanada. Genetic evidence for ATP-dependent endoplasmic reticulum-to-Golgi apparatus trafficking of ceramide for sphingomyelin synthesis in Chinese hamster ovary cells. *J. Cell Biol.* **144**, 673-685 (1999).

16 Y. A. Hannun & L. M. Obeid. Principles of bioactive lipid signalling: lessons from sphingolipids. *Nat. Rev. Mol. Cell Biol.* **9**, 139-150 (2008).

17 M. Levy & A. H. Futerman. Mammalian ceramide synthases. *IUBMB life* **62**, 347-356 (2010).

18 I. A. Guschina & J. L. Harwood. Lipids and lipid metabolism in eukaryotic algae. *Prog. Lipid Res.* **45**, 160-186 (2006).

19 N. Garmy, N. Taïeb, N. Yahi & J. Fantini. Apical uptake and transepithelial transport of sphingosine monomers through intact human intestinal epithelial cells: physicochemical and molecular modeling studies. *Arch. Biochem. Biophys.* **440**, 91-100 (2005).

20 W. Hu, J. Bielawski, F. Samad, A. H. Merrill & L. A. Cowart. Palmitate increases sphingosine-1-phosphate in C2C12 myotubes via upregulation of sphingosine kinase message and activity. *J. Lipid Res.* **50**, 1852-1862 (2009).

3.6 FIGURES AND TABLES

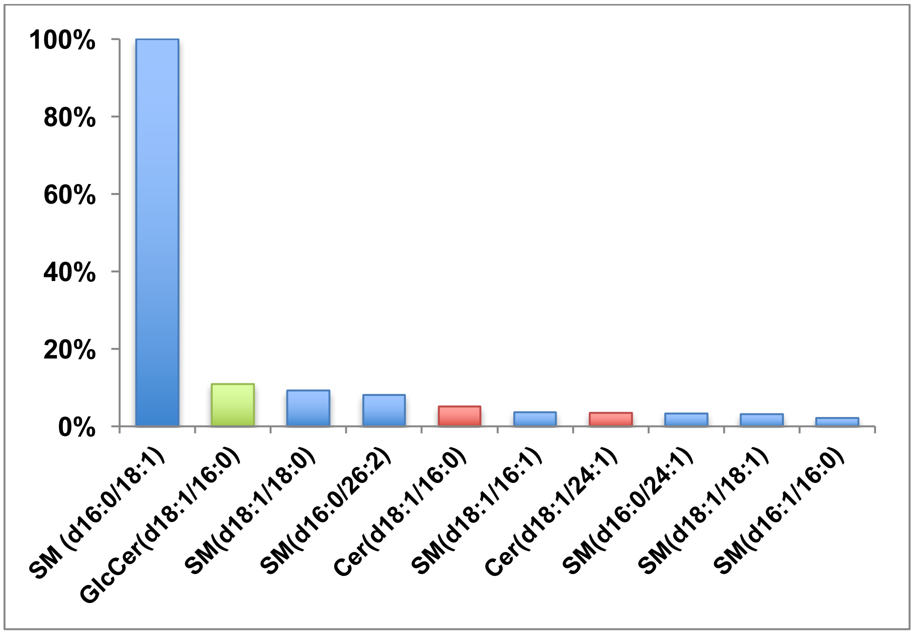

Figure 3.1. Ten most abundant sphingolipids in unlabeled NIH3T3 murine fibroblast cells. Lipidomics analysis of the lipid extracts from these cells was performed as described in the Materials and Methods.

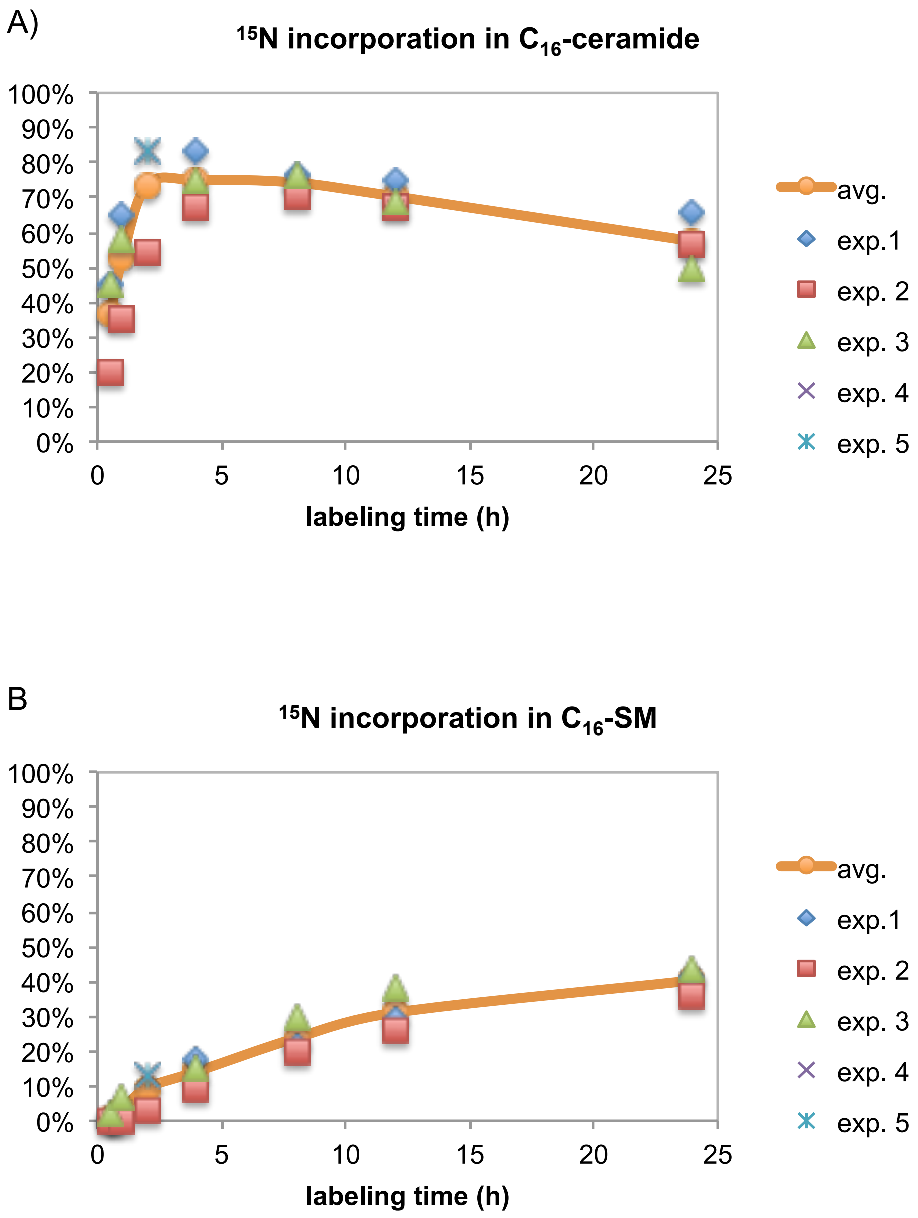

Figure 3.2. Incorporation of ^{15}N-sphingoid bases into A: ceramide and B: sphingomyelin at various labeling times. NIH3T3 murine fibroblast cells were pre-labeled with 3 μM of ^{14}N-sphingoids for 3 days prior to labeling with 6 μM of ^{15}N-sphingoid bases and 215 μM of ^{13}C-fatty acids for the indicated times.

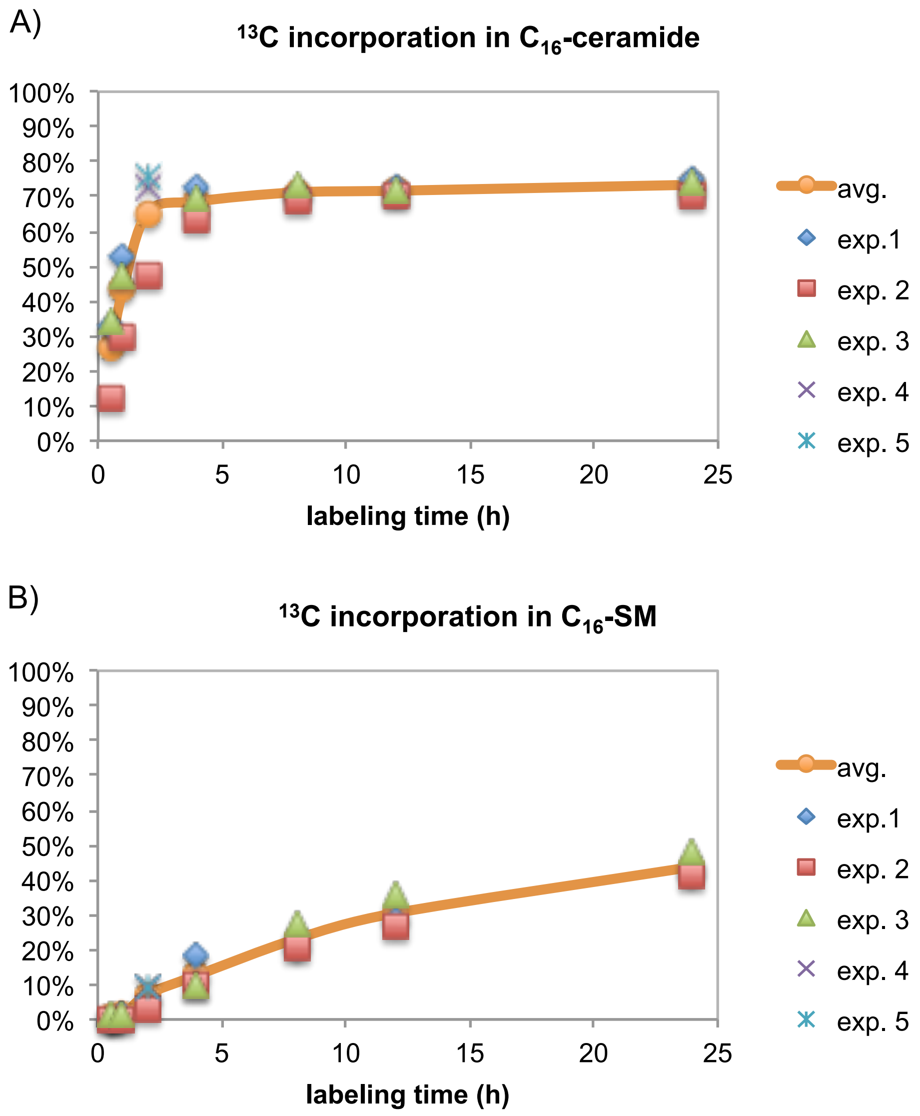

Figure 3.3. Incorporation of ^{13}C-fatty acids in A: ceramide and B: sphingomyelin in murine mouse fibroblast cells after various labeling times. Data was acquired from the same cell samples as the data shown in Figure 3.2.

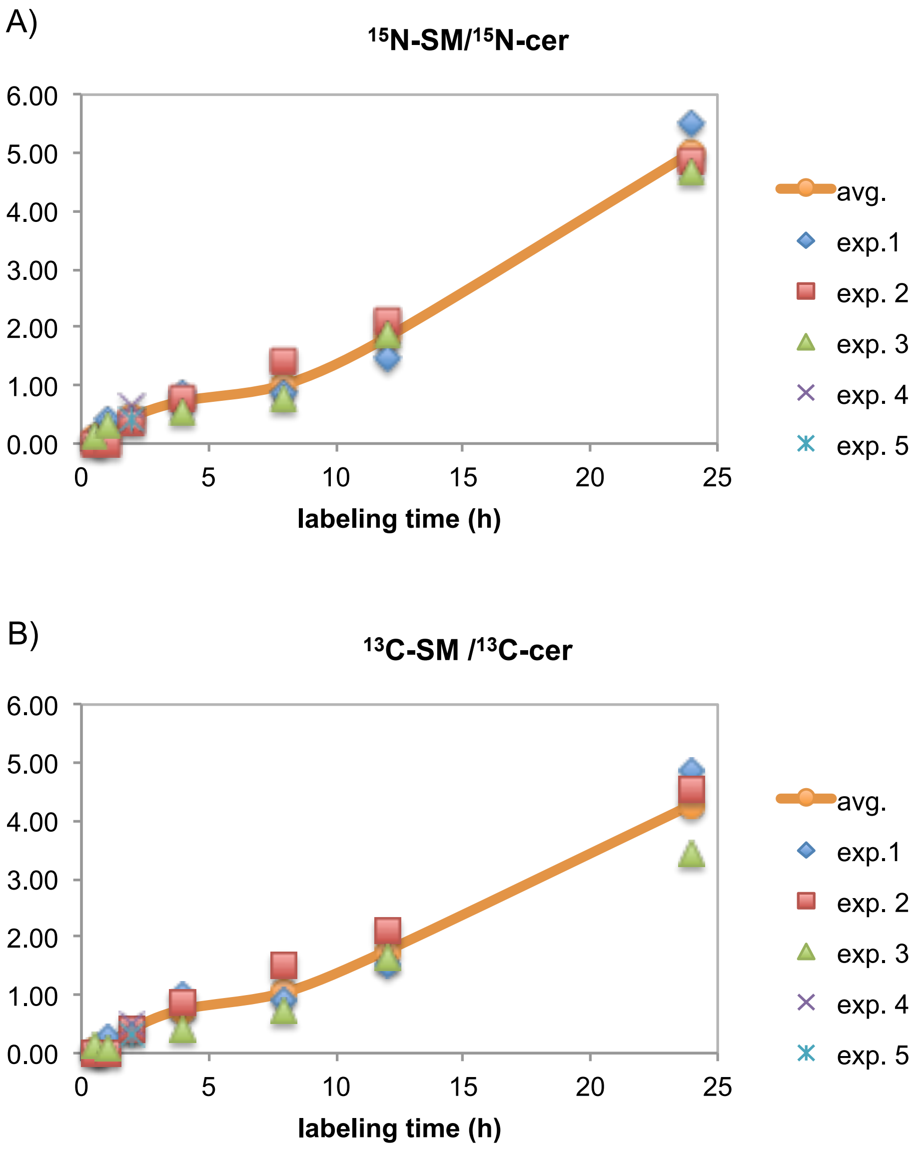

Figure 3.4 (cont.)

Figure 3.4 (cont.)

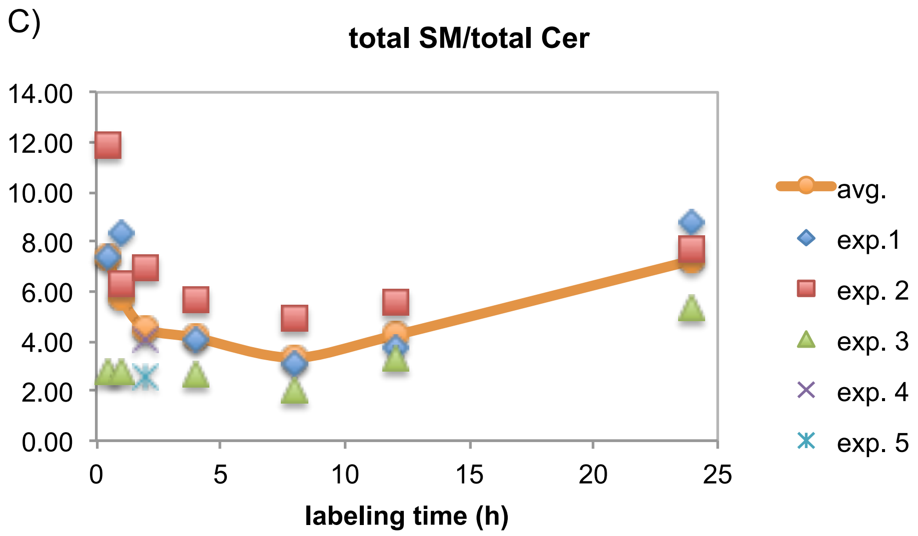

Figure 3.4. Change in SM/ceramide ratios at various labeling times. A: the ratio of ^{15}N-SM to ^{15}N-ceramide produced by metabolic incorporation of ^{15}N-sphingoid bases. B: the ratio of ^{13}C-fatty acid-labeled SM and ceramide, C: the ratio of total (labeled and unlabeled) SM and ceramide.

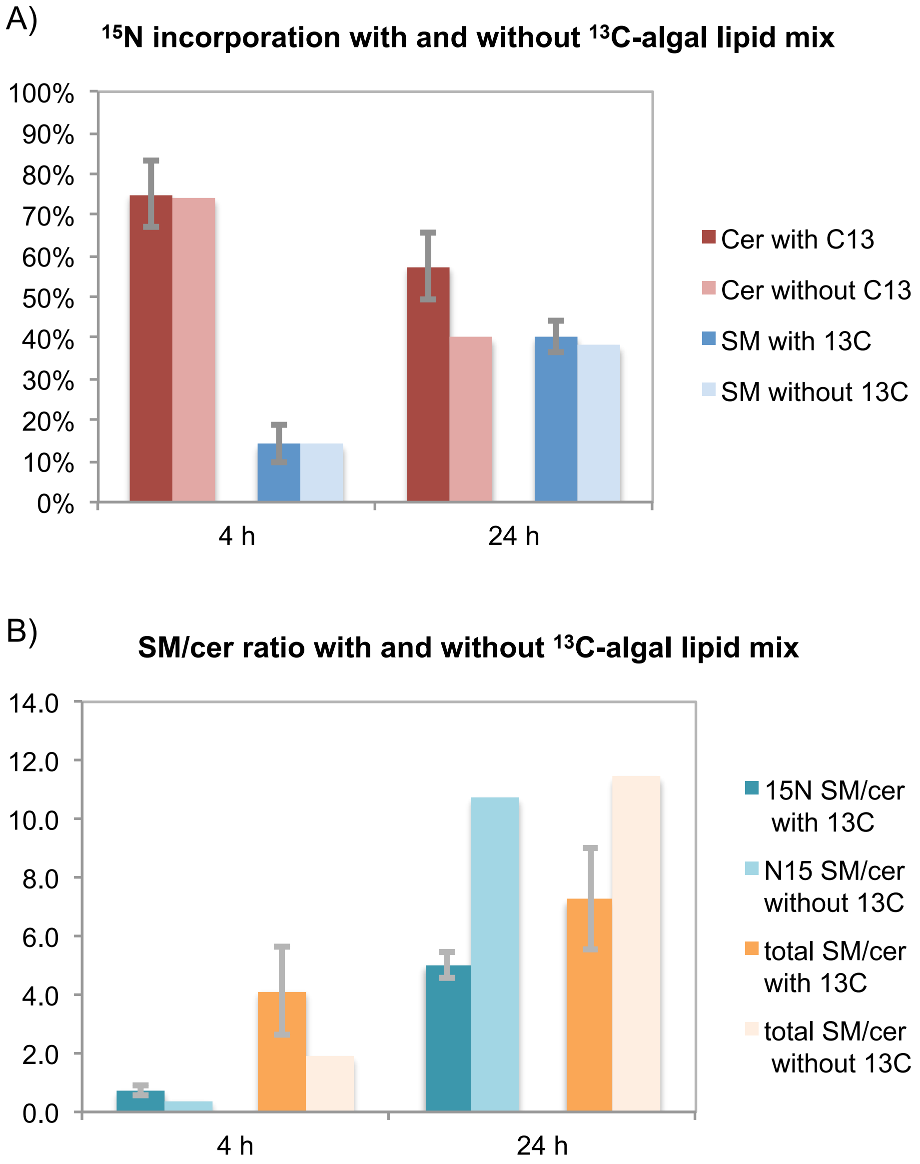

Figure 3.5. Changes in A: ^{15}N-sphingoid base incorporation and B: SM/ceramide ratio for metabolic labeling performs for 4 h and 24 h labeling with and without ^{13}C-algal lipid mix. NIH3T3 mouse fibroblast cells were pre-labeled with 3 µM of ^{14}N-sphingoid bases for 3 days prior to labeling with 6 µM ^{15}N-sphingoid bases in the presence and absence of 215 µM of ^{13}C-algal lipids.

Table 3.1. List of the top 10 sphingolipids that were detected in NIH3T3 cellular lipids and their *m*/*z* values.

Sphingolipids ions	***m*/*z* value**	**Chemical formula**	**Relative abundance**
SM (d18:1/16:0) + H*	703.5749	$C_{39}H_{80}O_6N_2P$	100%
GlcCer(d18:1/16:0) + H	700.5722	$C_{40}H_{78}O_8N$	11%
SM(d18:1/18:0) + H	731.6062	$C_{41}H_{84}O_6N_2P$	9%
SM(d16:0/26:2) + H	813.6844	$C_{47}H_{94}O_6N_2P$	8%
Cer(d18:1/16:0) + H	538.5194	$C_{34}H_{68}O_3N$	5%
SM(d18:1/16:1) + H	701.5592	$C_{39}H_{78}O_6N_2P$	4%
Cer(d18:1/24:1) + H	648.6289	$C_{42}H_{82}O_3N$	3%
SM(d16:0/24:1) + H	787.6688	$C_{45}H_{92}O_6N_2P$	3%
SM(d18:1/18:1) + H	729.5905	$C_{41}H_{82}O_6N_2P$	3%
SM(d16:1/16:0) + H	675.5436	$C_{37}H_{76}O_6N_2P$	2%

* It was first identified as SM (d18:0/16:1) by the database but manually identified as SM (d18:1/16:0) based on LC-MS/MS data.

Table 3.2. List of *m/z* values used to identify labeled and unlabeled ceramide and SM.

	C_{16}-ceramide		**C_{16}-SM**	
Isotope incorporation	*m/z*	Theoretical occurrance	*m/z*	Theoretical occurrance
Naturally the most abundant (1)	538.5199		703.5754	
One ^{13}C contained, occurring naturally	539.5233	0.368 of (1)	704.5788	0.422 of (1)
^{15}N labeled	539.5170		704.5724	
$^{13}C_{16}$ labeled (2)	554.5736		719.6291	
^{15}N and $^{13}C_{16}$ labeled	555.5706	0.195 of (2)	720.6261	0.249 of (2)
$^{13}C_{16}$ labeled both in acyl and backbone	570.6273		735.6828	

CHAPTER 4

EVALUATING THE INVOLVEMENT OF ACID SPHINGOMYELINASE IN INFLUENZA VIRUS ENTRY[*]

4.1 INTRODUCTION

Changes in the local concentration of ceramide have been shown to play roles in curvature formation and membrane fusion in model systems[1,2] and cells.[3-6] For example, sphingomyelinase treatment was reported to induce the formation of inward vesicles that were not enriched with either clathrin or caveolin by pinching off from the plasma membrane, even when ATP was depleted.[4] Sphingomyelinase treatment induced internalization of 10-30% of the plasma membrane in J774 macrophage cells and TRVb-1 cells (a variant of CHO cell). This clearly shows that local increases in ceramide levels influence trafficking by regulating membrane organization and fusion.

As discussed in Chapter 1, ceramides can be produced through the de novo pathway or via degradation of sphingomyelin by sphingomyelinases (SMase). The SMase-dependent pathway is considered to be responsible for stress-induced ceramide generation.[7] Mammalian SMases are classified as alkaline, neutral, or acidic in accordance with their optimal pH. So far, one alkaline SMase, four neutral SMases (nSMase1, nSMase2, nSMase3, and mitochondrial SMase) and one acidic SMase have been identified.[8]

Alkaline SMase is almost exclusively found in intestinal mucosa and human liver.[9] It was first found in 1969,[10] but seems to have been forgotten based on the lack of papers on the

---

[*] This work was the result of collaboration with Ashley Yeager. A.Y prepared the influenza virus, infected the cells, and assisted setting up the RT-qPCR procedure.
I thank Tatsiana Akraiko at the Functional Genomics Unit at the Roy J. Carver Biotechnology Center Biotechnology for technical assistance on RT-qPCR measurement.
Portions of this work were conducted at the Core Facility in the Carl R. Woese Institute for Genomic Biology and at the Functional Genomics Unit at the Roy J. Carver Biotechnology Center Biotechnology.

subject for about 20 years, although rapid progress was made on other SMases during this time. The lack of attention paid to alkaline SMase is likely because no genetic disorder is known to be caused by mutations in alkaline SMase. In addition, sphingolipid research has mainly focused on intracellular signaling and membrane organization, so extracellular enzymes such as alkaline SMase and secreted SMase (which will be discussed later) were largely neglected.[11] Nonetheless, recent studies show that alkaline SMase is responsible for the digestion of dietary sphingomyelins that are approximated to be about 300 mg per day.[12] Knockout of this enzyme increased sphingomyelin and decreased ceramides in intestinal contents and induced mucosal hypertrophy.[12] A recent report also showed that sphingolipids in the intestine, specifically S1P are involved in the occurrence of allergic diarrhea and pathogenic cell trafficking.[13] Sphingomyelin comprises a significant portion of the dietary sphingolipids,[14] therefore alkaline SMase that cleaves sphingomyelin may affect the composition of acylated and unacylated sphingolipids in the intestinal lumen and intestinal tissues. Certainly more effort should be made to understand the roles and significance of alkaline SMase.

Among the neutral SMases, nSMase2, also known as sphingomyelin phosphodiesterase 3 (SMPD3), is thought to be the major SMase in cells that is responsible for ceramide signaling. Nonetheless, the first cloned nSMase was nSMase1, or sphingomyelin phosphodiesterase 2 (SMPD2)[15] which is ubiquitously expressed in almost all tissues and localized to the ER and Golgi.[16] Although it hydrolyzes sphingomyelin in vitro, nSMase1 also hydrolyzes lyso-PC and lyso-PAF[17], and no sphingomyelin accumulation was observed in a mutant mouse line that was deficient in nSMase1.[18] This and the discovery and cloning of nSMase2, which was first found in rat brain tissue,[19] led to skepticism regarding whether nSMase1 is truly a sphingomyelinase. SMase2 is localized in the Golgi and plasma membrane, and it is predominantly considered to be the nSMase responsible for ceramide signaling in cells. Deletion of this gene impaired growth and development in mice, producing a dwarf mouse phenotype.[20,21] Interestingly, the findings that mice lacking nSMase2 activity exhibit residual nSMase activity, and mutant mice that were deficient in both SMPD2 and SMPD3 did not accumulate sphingomyelin[18] argue against dismissing nSMase1 as a neutral sphingomyelinase. A third nSMase that has little homology to nSMase1 and nSMase2 was first identified in bovine brain[22] and then in human tissues (mostly heart and skeletal muscles).[23] A fourth neutral SMase, mitochondrial SMase, was fairly recently identified, first in zebrafish[24] and then in mouse.[25] Mitochondrial ceramides are reported to induce apoptosis,[26,27] but additional research is required to fully elucidate its biological functions and significance.

Acid SMase (aSMase) or sphingomyelin phosphodiesterase 1 (SMPD1) is the first SMase that was cloned in 1966.[28] Its biological significance was elucidated soon after its cloning in reports that Niemann-Pick disease patients were deficient in aSMase.[29] A recessive mutation in the *SMPD1* gene is the direct cause of two of the three types of Niemann-Pick disease (NPD), specifically type A and B.[30,31] Type A NPD is characterized by rapid progressive neurodegeneration that leads to death by age 3 while type B NPD patients have much less severe symptoms and a longer life expectancy (up to adulthood).[30] ASMase is a lipid catabolic enzyme that is localized in the lysosomes, and its role in lipid catabolism is supported by aberrant lysosomal lipid storage in NPD cells.[32] Because of its subcellular localization, aSMase is also called lysosomal aSMase. Lysosomal aSMase is ubiquitously expressed in all tissues[28] and cell types[33] and is thought to be involved in many stress-induced cell responses, including apoptosis,[34] as well as in regulating membrane organization and endocytosis, as described in Chapter 1.

The gene encoding for aSMase, *SMPD1*, expresses both lysosomal aSMase and another form of sphingomyelinase, secretory SMase (sSMase). Depending on the sorting pathway at the Golgi, the same pro-aSMase protein can be transported to the lysosomes (lysosomal aSMase) or secreted extracellularly (sSMase).[35] These differences in trafficking pathways result in different glycosylation patterns on lysosomal aSMase and sSMase.[31] Although originating from the same gene, the enzymatic properties of these two SMases are different. ASMase does not require Zn^{2+} and is active at low pH[35]. In contrast, sSMase requires Zn^{2+} and neutral pH for its enzymatic activity.[35] Their turnover rates also differ, where the life time of lysosomal aSMase is less than 6 h, while sSMase is much more stable.[36] Elevated sSMase activity has been detected in the serum of human patients with many diseases, such as type II diabetes, chronic heart failure, sepsis, and hypercytokinemia.[36]

Because sphingolipids play critical parts in membrane (re)organization and internalization, as discussed above and in Chapter 1, it is not surprising that SMases have been implicated in infections by various pathogens ranging from bacteria, fungi, parasites, and viruses.[37-39] In particular, host aSMase has been shown to control the entry of many pathogens, including *Listeria monocytogenes*,[40] *Neisseria meningitidis,*[41] Pseudomonas aeruginosa,[42] *Mycobacterium avium,*[40] *Trypanosoma cruzi,*[43] choriomeningitis virus,[40] Ebola virus,[44] and measles virus.[45] Here we investigated how SMPD1 levels in host MDCK cells affect influenza virus entry using RNAi. We found that influenza virus entry was only slightly affected by the reduced aSMase levels. However, the influenza virus seemed to upregulate the levels of mRNA for SMPD1 and other sphingomyelinases. These results suggest that SMPD1 may play an important role in influenza virus infection.

4.2 MATERIALS AND METHODS

4.2.1 Materials

Lipofectamine RNAiMAX, EDTA-free Halt Protease and Phosphatase Inhibitor Cocktail 100X were purchased from Thermo Fisher. Mission siRNA Universal Negative Control #1 and desipramine hydrochloride were purchased from Sigma-Aldrich. Polyclonal rabbit primary antibody against SMPD1 protein (ARP35630_P050) of many species including dog was purchased from Aviva Systems Biology. Goat polyclonal primary antibody against β-actin (ab8229) and rabbit polyclonal antibody against influenza A virus nucleoprotein (ab22285) were purchased from Abcam. HRP-conjugated anti-rabbit secondary antibodies from Cell Signaling

Technology (#7074) and Thermo Fisher (A16104) were used. Goat secondary antibody against rabbit antibody with Alexa Fluor 488 conjugate (A11008) was purchased from Invitrogen. 2X Laemmli sample buffer, the Clarity Western ECL blotting substrate that was used for chemiluminescence, iTaq Universal One-Step RT-qPCR kit (1725150), and 4-20% polyacrylamide Mini-PROTEAN precast gels were from Bio-Rad. Glass bottomed petri dishes were obtained from CellVis. Paraformaldehyde was purchased from Electron Microscopy Sciences. Alexa488 goat anti-rabbit IgG Hoechst 33342 nuclear stain, and Lipofectamine RNAiMAX were purchased from Life Technologies. RNeasy mini kit for RNA isolation and Cf_SMPD1_2_SG QuantiTect Primer Assay (QT01646463, targeting XM_542452, XM_857542) were from Qiagen. Primers for canine GAPDH and influenza virus M1 protein were purchased from IDT. Fresh chicken blood was obtained from the Department of Animal Sciences at the University of Illinois Urbana-Champaign. V-bottom 96 well plates were purchased from Sarstedt. MDCK cells (ATCC® CCL-34™) and the A/Aichi/2/68 (H3N2) strain of the influenza virus (ATCC® VR-1680™) were purchased from ATCC.

4.2.2 Cell culture and influenza virus propagation

MDCK cells (ATCC® CCL-34™) were grown in Dulbecco's Modified Eagle Medium (DMEM) supplemented with 10% FBS and 1% penicillin/streptomycin in a 5% CO_2 incubator at 37°C. MDCK cells were grown in 12 well plates for Western blots, 24 well plates for RT-qPCR, and glass bottomed dishes for confocal microscopy. The A/Aichi/2/68 (H3N2) strain of the influenza virus was propagated as described previously.[46] Virus stock solutions were prepared in DMEM with 7.5% BSA, 25 mM HEPES and 2 μg/mL trypsin, and quantified by 50% tissue culture infectious dose assay (TCID50) and hemagglutination assay[46] and calculated by the method of Reed and Muench.[47]

4.2.3 RNA interference and desipramine treatment

RNA interference with siRNAs was used to manipulate SMPD1 levels in MDCK cells. The siRNAs against canine SMPD1 (XM_542452.4) were designed and manufactured by

Sigma-Aldrich. The sequences of the siRNAs are GUCUCAUCUCUCUCAAUAUdTdT (sense), AUAUUGAGAGAGAUGAGACdTdT (antisense), GAGGAUAGCUGUGGUAAGAdTdT (sense), UCUUACCACAGCUAUCCUCdTdT (antisense), GAGACAAGGUACAUAUAAUdTdT (sense), AUUAUAUGUACCUUGUCUCdTdT (antisense). Mission siRNA Universal Negative Control #1 (Sigma-Aldrich) was used as a negative control. For transfection, MDCK cells were seeded in either 12 well plates or 24 well plates. One day after seeding, the cells were transfected with the siRNAs complexed with Lipofectamine RNAiMAX. After incubation with the transfection complex for 6 h, the cells were incubated in fresh media without transfection complex until either influenza virus infection or an assay was performed. Desipramine stock solution (25 mM) was prepared in water and stored at -20°C.

4.2.4 Influenza virus infection

After washing with PBS two times, the cells were incubated with virus stock solution diluted in DMEM (final concentrations of BSA and trypsin in the culture medium were 0.2% and 2 μg/mL, respectively) at a multiplicity of infection (MOI) of ~10 (determined by TCID50 per number of cells) for 30 min 4°C, and then at 37°C for 30 min. Then the cells were washed with the virus media (DMEM with 0.2% BSA and 2 μg/mL trypsin) to remove unbound virus, placed into fresh virus media, and incubated at 37°C for the specified time.

4.2.5 Western blot

The medium in the cell culture was aliquoted for Western blot analysis. Then the transfected cells were removed from the culture medium, thoroughly washed with PBS, lysed with lysis buffer containing 1% Triton X-100, 20 mM Tris-HCl, 137 mM NaCl, 10% glycerol, 2 mM EDTA supplemented with EDTA-free Halt Protease and Phosphatase Inhibitor Cocktail following the manufacturer’s protocol. The cell lysates and the aliquoted media were mixed with Laemmli sample buffer containing mercaptoethanol (5% v/v in final concentration) and heated at 85°C for 5-10 min. The proteins in the cell lysates and the media were separated by electrophoresis on 4-20% polyacrylamide Mini-PROTEAN precast gels using a Mini-Protean system. The proteins in the gels were transferred to either a PVDF or nitrocellulose membrane, and blocked for 30 min with 2.5% skim milk powder in Tris-buffered saline and Tween 20 (TBST) buffer at room temperature. The membranes were incubated in SMPD1 primary antibody (1:1000) or β-actin primary antibody (1:500) diluted in TBST with 1% skim milk powder overnight at 4°C. After washing three times, the membranes were incubated with HRP-conjugated secondary antibody diluted in TBST with 1% skim milk powder following the manufacture's protocols for 1 h at room temperature and visualized by chemiluminescence using Clarity Western blot ECL and ImageQuant LAS 4010 imager.

4.2.6 Immunofluorescence and confocal fluorescence microscopy

The cells were fixed with 1% paraformaldehyde in PBS at room temperature and permeabilized with 0.1% Triton-X in PBS for 10 min on ice. After thorough washing with PBS, the cells were blocked with 1% BSA in PBS for 30 min at room temperature, incubated with the diluted rabbit primary antibody against influenza A virus nucleoprotein in PBS with 1% BSA for 1 h at room temperature and then washed with 1% BSA in PBS at room temperature three times. The cells were incubated with the anti-rabbit secondary antibody conjugated with Alexa 488 diluted in PBS with 1% BSA for 1 h at room temperature and washed with 1% BSA in PBS three times. Hoechst 33342 was added and incubated for 10 min for nuclear staining following manufacturer's protocol. The samples then were imaged using a Carl Zeiss LSM 700 at room temperature. A 488 nm laser and a 405 nm laser were used to excite Alexa 488 fluorophore and Hoechst 33342 respectively.

4.2.7 Quantitative reverse transcription polymer chain reaction (RT-qPCR)

RNA in the cells and the media were extracted using RNeasy mini RNA isolation kit from Qiagen following the manufacture's protocol. The concentration of RNA in the final product was measured using NanoDrop. A commercially available primer assay for canine SMPD1 was used. The primer sequences used for influenza M1 gene were based on literature reports[48-50] where the exact sequences are 5'-AGATGAGTCTTCTAACCGAGGTCG-3' and 5'-

TGCAAAAACATCTTCAAGTCTCTG-3'. The primer sequences for dog GAPDH were 5'-AACATCATCCCTGCTTCCAC-3', 5'-GACCACCTGGTCCTCAGTGT-3'. Reverse transcription and amplification were performed using the primers and iTaq Universal One-Step RT-qPCR kit following the manufacturer's protocol using a ABI 7900 real time PCR machine.

4.3 RESULTS

4.3.1 Expression levels of aSMase in SMPD1 knockdown MDCK cells and media

First, the SMPD1 gene expression levels in the MDCK cells treated with SMPD1 targeting siRNAs or control siRNA were evaluated by RT-qPCR at 48 h posttransfection. The SMPD1 gene expression level decreased by at least 50% in SMPD1 targeting siRNA treated cells compared to control siRNA treated cells in two biological replicates (Figure 4.1A). Next, the SMPD1 protein levels (which include aSMase and sSMase) in the MDCK cells and the media after RNAi were evaluated by Western blot at 48 h posttransfection. Even though aSMase is considered to be a lysosomal housekeeping protein,[31] the level of cellular SMPD1 detected by Western blot was very low in all samples to a similar degree, even in the sample without siRNA treatment (Figure 4.1B). Because aSMase can be secreted through lysosomal exocytosis[51,52] and sSMase is expressed from the encoding *SMPD1* gene, the level of extracellular SMPD1 protein was also assessed by collecting the media and subjecting it to Western blot. Very intense bands were detected in the blot of all media samples, indicating the presence of aSMase or sSMase in the media. The media that was collected from the siRNA-treated cell culture showed only slightly weaker signals than the media from the cells treated with control siRNA. However, these results did not necessarily indicate that the knockdown was ineffective because further investigation revealed that the FBS that had been added to the culture medium contained a high level of sSMase[53] and the antibody used in this study detects bovine SMPD1 protein as well as canine SMPD1 protein. Therefore, when the 6 h of transfection procedure was complete, the cells were incubated in serum-free media supplemented with BSA at final concentration of 0.2% for 42 h, and then the cell lysates and culture media were collected and analyzed by Western blot. Figure 4.1B shows again that the bands from cellular SMPD1 were much weaker than those from extracellular SMPD1, as observed when FBS was added to the media. However, it also shows that knockdown with siRNAs lowered the levels of cellular SMPD1 by approximately 50% (Figure 4.1C). Although the Western blot showed that the media from all the cells contained extracellular SMPD1, the band for the cells transfected with SMPD1 siRNA was weaker than that of the control and untransfected MDCK cells, indicating some knockdown of SMPD1. However, the knockdown of extracellular SMPD1 is difficult to quantify using the blot shown in Figure 4.1C because the extracellular SMPD1 would have accumulated in the medium before the expression of this proteins started to decrease. Nevertheless, these results show that SMPD1 knockdown using siRNAs reduced the levels of both cellular and extracellular SMPD1.

4.3.2 Visualization of influenza virus entry in SMPD1 knockdown and control MDCK cells by immunofluorescence

Next, immunofluorescence microscopy was used to investigate how lowering SMPD1 levels with RNAi and desipramine, a pharmacological inhibitor of lysosomal aSMase, affects influenza virus entry. The MDCK cells were transfected with either SMPD1 siRNAs or control RNAs for 6 h, and then the media were substituted to either 10% FBS or 0.2% BSA in DMEM without transfection complex. At 48 h post-transfection, the MDCK cells that were transfected with SMPD1 siRNAs or negative control RNAs were infected with 10 MOI of the influenza virus. At 1.5 h post infection (hpi), the cells were fixed, permeabilized, immunolabeled for influenza virus nucleoprotein, and imaged with confocal fluorescence microscopy. The nucleoprotein was imaged because it locates to the nucleus shortly after the influenza virus enters the cell. Figure 4.2 shows the confocal fluorescence microscopy images of the nucleoproteins in MDCK cells with and without SMPD1 knockdown. Little difference was observed in the fluorescence levels within the SMPD1 knockdown cells and control siRNA-treated cells that were incubated in medium containing 10% FBS after transfection but before influenza infection (Figure 4.2A). When the cells were incubated in DMEM that contained 0.2% BSA instead of 10% FBS for the 48 h after transfection but before infection, SMPD1 knockdown appeared to slightly decrease the amount of nucleoproteins in the cell and also its localization at the nuclei (Figure 4.2B) upon infection.

4.3.3 Quantification of influenza virus entry in SMPD1 knockdown and control MDCK cells by RT-PCR

Next, we assessed the virus entry in SMPD1 knockdown, and control MDCK cells that were transfected with control siRNA by measuring the influenza virus M1 gene level using RT-qPCR. The MDCK cells were transfected and infected in the same way as described above. In addition, RT-qPCR was also used to measure M1 expression in influenza-infected MDCK cells in which aSMase activity was pharmacologically reduced by incubating the cells in the presence of desipramine (25 μM) overnight prior to the infection. The total RNA of the infected cells was collected at 1.5 hpi. The relative amount of internalized virus was quantified by measuring the level of the virus M1 RNA and comparing it to the level of cellular GAPDH, which is a housekeeping gene. As shown in Figure 4.3A, the virus M1 gene level in the infected MDCK cells subjected to SMPD1 knockdown was about 80% of that of the infected MDCK cells that were subjected control siRNA transfection (infected control cells), indicating SMPD1 knockdown slightly decreased the infection (single measurement). A similar decrease in the virus M1 gene level was measured in the desipramine-treated cells after infection.

The SMPD1 levels in the infected cells were also measured (Figure. 4.3A, red). Without infection, knockdown with the siRNAs decreased the SMPD1 level to no more than 50% of that measured in the cells treated with control siRNA (Figure 4.1A). However, the SMPD1 level measured in the SMPD1 knockdown cells after infection was about 60% of the SMPD1 mRNA level measured in the infected control cells after infection. This reduced level of SMPD1 knockdown in the presence of infection may suggest that the influenza virus itself upregulates

SMPD1 levels. As shown in Figure 4.3B, at 1.5 hpi, SMPD1 knockdown did not produce a statistically significant reduction in M1 levels when serum free media was used after the transfection and before the infection, which is inconsistent with the confocal microscopy data presented above. In fact, very high variations in M1 and SMPD1 levels were observed in the three replicate measurements. This high variance in the three repeats may be due to small variations in MOI, the time after transfection at which infection began, or the time after that infection was allowed to proceed.

We also measured the M1 level at 8 hpi, which is approximately the duration of one infection cycle (Figure 4.3C). The M1 levels barely decreased, by only about 10%, in the SMPD1 knockdown cells. In addition, the level of SMPD1 in these knockdown cells was about 75% of that in control cells, which indicates the SMPD1 level further increased in the presence of influenza virus infection. However, desipramine treatment significantly lowered M1 expression, down to about 30% of control siRNA-treated cells, in influenza-infected cells 8 hpi, but increased SMPD1 levels to ~250% of that measured in control siRNA-treated cells.

4.3.4 Change of SMPD1 level by influenza virus infection

Our data above suggest that influenza virus infection was correlated with changes in the level of SMPD1 mRNA. To confirm this, the level of SMPD1 mRNA in influenza virus infected cells that were not treated with any siRNA was compared to that in cells that were not infected with virus (mock infected) by measuring SMPD1 mRNA levels using RT-qPCR. At 2 hpi, the SMPD1 levels in the virus-infected cell samples were consistently higher (about 40%, 2 replicates) than that of the mock-infected control cells (Figure 4.4). Although the relative SMPD1 levels measured in the two influenza virus-infected replicates were highly variable at a time of 4 hpi, they seemed to return to that found in uninfected cells by 6 hpi. These findings confirm that SMPD1 mRNA increases during the early stages of influenza virus infection. This suggests that sphingolipids, and particularly those generated by SMPD1, are involved in the early stages of influenza virus replication.

4.4 DISCUSSION

Pathogen infection requires significant rearrangement of the host and viral membranes, therefore it is not surprising that host membrane lipids can influence virus infection and replication.[54] Several studies show that aSMase is important in the entry of not only viruses but also other pathogens including bacteria, fungi, and parasites, into the cytosol and their subsequent escape.[40-45] These studies suggest that ceramide-enriched domains induced by SMase are essential for pathogen entry. For example, non-enveloped viruses that are known to pierce or rupture the membrane, such as adenovirus, were recently reported to hijack the host cell's membrane repair mechanisms to facilitate entry.[55] A key event in membrane repair process is to enhance the endocytosis of damaged membranes by the secretion of aSMase through lysosomal exocytosis in response to Ca^{2+} influx at the sites of membrane damage. The adenovirus promotes its entry by inducing secretion of lysosomal aSMase and triggering ceramide-enriched domain formation. Although the entry of enveloped viruses is very different from that of non-enveloped viruses, it is also significantly affected by aSMase. Ebola virus particles were reported to strongly associate with sphingomyelin-rich regions in the plasma membrane and surface-localized aSMase.[44] Pharmacological inhibitors and RNAi inhibited the infection of Ebola virus and Ebola virus pseudotyped virus in HeLa cells. Therefore, we hypothesized that aSMase would regulate influenza virus infection, and focused on the role of aSMase in the early phase of influenza virus infection.

Here we used MDCK cells as the host for influenza infection because they were used to propagate our influenza virus strain, and this cell line is commonly used for basic influenza research and vaccine production.[56-59] Prior to infection, cellular SMPD1 protein was barely detectable in the MDCK cells, which was somewhat unexpected because aSMase is thought to be a housekeeping protein in the lysosomes.[31] A lack of antibody recognition is unlikely responsible for the discrepancy between our expectations and the experimental results because, interestingly, using the same antibody, our Western blot data show that a significant amount of SMPD1 was secreted from the MDCK cells into the medium. Whether the protein detected by the SMPD1 antibody in the media was aSMase, sSMase, or a mixture of the two is not known. In human cells, sSMase undergoes no proteolytic processing from pro-SMase and has a reported molecular weight of 75-80 kDa, while aSMase is produced by more extensive cleavage of pro-aSMase at the lysosomes where its molecular weight decreases to 65 kDa, and eventually down to a 52 kDa protein that is mostly inactive.[60] Not much information is available on canine SMPD1 proteins. The molecular weight of dog SMPD1 protein is calculated to be 69 kDa based on the canine genome.[61] This is slightly higher than the molecular weight we observed in the Western blot (approximately 63-65 kDa). Post-translational modification of SMPD1 proteins in canine cells has not been studied. However, considering that the molecular weight of extracellular SMPD1 detected on our blot was smaller than that of cellular SMPD1, the extracellular SMDP1 that we detected may have been the hydrolyzed form of aSMase that was secreted through lysosomal exocytosis. Indeed, lysosomal exocytosis occurs not only in specialized secretory cells (such as neurons), but also in both polarized and nonpolarized cells, where it is Ca^{2+}-dependent.[62] Whether the extracellular SMPD1 is active, and if so, what conditions (pH and Zn^{2+} concentration) optimize its activity would need to be determined to establish the identity of the extracellular SMPD1.

Visualization of influenza nucleoproteins by immunofluorescence 1.5 h after infecting cells that had been transfected with SMPD1 siRNAs and control siRNAs prior to the infection suggested that exposing the cells to serum after transfection influenced whether SMPD1 knockdown affected virus entry. This is consistent with our observation that the knockdown was more effective in terms of protein level when the cells were incubated in serum-free medium following transfection (Figure 4.1). Noteworthy, influenza infection was always performed under serum-free conditions. The cells that were incubated in serum-free medium prior to infection may have acclimated to this medium condition, while the cells that were incubated in 10% FBS, the normal cell growth media for MDCK cells, would have been adjusting to the new culture environment during virus infection. It is not clear how this need to acclimate during virus infection might affect virus entry, but this factor should be considered when designing future experiments, since serum deprivation not only alters protein synthesis capacity[63] and secretion[64] but also induces global change in cell signaling responses.[65]

To measure the extent of the virus inside the cells, we measured the M1 RNA level that would be proportional to the extent of the infection by RT-qPCR. RT-qPCR is advantageous over traditional assays for investigating the early stage of infection because it is much more sensitive than the traditional assays by principle. Our data showed that at 1.5 hpi, the effect of SMPD1 knockdown on influenza virus infection was not statistically significant. Slightly lower M1 RNA levels were observed in SMPD1 knockdown cells incubated in serum-containing medium prior to infection (Figure 4.3A), but the reproducibility of these results was not assessed, and our immunofluorescence results (Figure 4.2A) showed no difference in M1 levels, thus viral entry under these conditions. The data from the three biological replicates of the cells incubated in the serum free medium after siRNA treatment and before infection (Figure 4.3B) show high variation, demonstrating that SMPD1 knockdown has no statistically significant effect on influenza virus entry. These results are contrary to the previous reports on the effect of aSMase in other pathogenic infections. The knockdown here may not have been sufficient to induce significant, reproducible changes in influenza virus entry. Moreover, the cellular level of SMPD1 protein in this specific cell line (MDCK) may be too low to observe an effect of SMPD1 knockdown. Figure 4.1 shows that, unexpectedly, the cellular SMPD1 protein level in the uninfected MDCK cells was very low even without knockdown, and the amount of extracellular SMPD1 protein secreted into the medium over the 1.5 h duration of influenza infection may not have been sufficient to affect influenza virus entry. The effects of SMPD1 on influenza virus infection might become more clear if cells that endogenously express higher levels SMPD1 or were manipulated to overexpress SMPD1 were employed. Alternatively, SMPD1 proteins may not influence the early stages of influenza infection. Interestingly, SMPD1 gene expression levels in the SMPD1 knockdown cells compared to control siRNA treated cells was higher in the infected cells than uninfected cells (Figure 4.1A vs. Figure 4.3), suggesting that the virus internalization may induce an increase in cellular SMPD1 expression. This possibility was assessed with the subsequent experiments and will be discussed below.

Interestingly, while the difference in virus M1 RNA levels were not statistically significant (Figure 4.3B), the virus nucleoprotein levels detected by immunofluorescence showed a slight decrease in SMPD1 knockdown cells compared to control siRNA treated cells (Figure 4.2B) in the infected cells that were incubated in the serum free media between the transfection with siRNAs and the infection with influenza virus. Among the three biological replicates in the RT-qPCR data in Figure 4.3B, only one SMPD1 knockdown cell sample had a slightly lower virus M1 level than control siRNA treated cells. The possibility of nonspecific binding in immunofluorescence or irreproducible knockdown prior to the infection cannot be excluded and needs to be tested under similar experimental conditions. However, it should be also noted that the levels of virus RNA (as well as virus mRNAs) change in the course of infection, even at 1.5 hpi.[66] Interestingly, a report[66] showed that upon influenza virus infection, the virus M1 RNA level first decreased until 2 hpi and then increased until 6 hpi. Based on that, the increased virus M1 RNA level in SMPD1 knockdown cells compared to control siRNA treated cells may indicate the delay in the decrease of virus M1 RNA by SMPD1 knockdown, which would, then, be not contrary to the immunofluorescence data. However, more experimental evidence is required to confirm whether the same change in virus M1 RNA also occurs during infection with the virus strain used in this study, and whether and how SMPD1 knockdown affects these changes in M1 RNA.

Virus infection alters host proteins and genes. Some enveloped viruses, such as Sindbis virus (the prototypic alphavirus)[67] and measles virus[45] as well as the non-enveloped rhinovirus[68] increased the host aSMase activity upon infection. Therefore, it is also plausible that influenza virus infection may alter host gene expression, either directly by viral components, or indirectly as a cell response to infection. Our RT-qPCR data indicate that SMPD1 levels increased during the early stages of influenza virus infection. The proteins whose levels were altered during influenza virus infection (H1N1) in MDCK cells were previously documented with mass spectrometry-based quantitative proteomics using the approach of stable isotope labeling by amino acids (SILAC) in cell culture.[69] Although changes in SMPD1 were not reported, this may be due to the low level of cellular SMPD1 proteins in MDCK cells, as shown in our data. The increased SMPD1 levels we observed at the early stage of influenza infection is in line with the observation that the levels of proteins that are related to metabolic processes, including lipid metabolism, were increased at the early phase (4 hpi) of infection.[69] Interestingly, this study revealed that acid ceramidase 1(ASAH1), which cleaves ceramides to sphingosine and fatty acids, was among the proteins that were increased at the early phase of the infection, implying the significance of sphingolipids during the early phase of the infection. In addition to eliciting endocytosis, ceramides can induce cytoskeletal reorganization and apoptosis, as discussed in Chapter 1, which coincides with the typical morphological changes that the host cells undergo during influenza virus infection. But our data, together with the aforementioned report,[69] demonstrate that influenza virus influences host sphingolipid metabolism. It also renders another possible scenario in our observation that inhibiting SMPD1 using siRNA only slightly lowered the infection. Many reports used lower MOI than were used herein, typically below 0.5 MOI. This lower MOI would make it more challenging to detect the virus at the early phase of the infection and synchronize the infection, but reduces the cytopathic effect of the virus. In our experiments, some virus particles may have been internalized after the SMPD1 levels became elevated due to virus infection, which could make it difficult to ascertain the effects of lowering SMPD1 on virus entry.

Interestingly, desipramine treatment lowered the M1 gene levels 8 hpi by about 65%, whereas treatment with siRNAs had a minimal effect, reducing M1 expression by about 10%. The decrease in M1 levels observed after desipramine treatment may not be due to lower aSMase protein levels. Though desipramine and other cationic amphiphilic drugs such as chlorpromazine and chloroquine are frequently used as aSMase inhibitors, these drugs have more effects than just inhibition of aSMase. Desipramine is also a potent inhibitor of acid ceramidase,[70] a catabolic enzyme that degrades ceramide to sphingosine in lysosomes as mentioned above. Little is currently known about the roles of acid ceramidase in infection, but considering the broad effects of phosphorylated sphingosine (S1P) in cells, acid ceramidase that produces sphingosine may have important roles in infection. More importantly, these cationic amphiphilic drugs raise the pH of the lysosomes [71] and late endosomes.[72,73] This is an important side effect because the low pH in late endosomes elicits changes in the influenza envelope protein, hemagglutinin, that are required for release of the virus ribonucleoprotein complex into the cytosol during virus entry.[74] The increase in late endosomal pH induced by desipramine would inhibit the escape of the influenza virus from the endolysosomes[75] and prevent the replication of virus genes. Therefore, the inhibitory effect of desipramine on influenza infection cannot be attributed to aSMase inhibition.

It has been previously reported that the de novo synthesis of sphingolipids and sphingomyelin synthase 1 (SGMS1) are essential for the transport of influenza virus proteins.[76] Our data suggest the possibility that sphingolipids are involved in the early phase of the infection, which including entry and escape from the endosomes. However, further infection experiments that involve use of a pharmacological inhibitor that is specific to aSMase(and inactive against acid ceramidases such as siramesine,[77] and complete knockout of SMPD1 gene expression are required to verify these findings and better elucidate the involvement of SMPD1 in influenza virus infection.

4.5 REFERENCES

1 M. Kunishima, M. Tokaji, K. Matsuoka, J. Nishida, M. Kanamori, K. Hioki & S. Tani. Spontaneous membrane fusion induced by chemical formation of ceramides in a lipid bilayer. *J. Am. Chem. Soc.* **128**, 14452-14453 (2006).

2 F. M. Goñi & A. Alonso. Biophysics of sphingolipids I. Membrane properties of sphingosine, ceramides and other simple sphingolipids. *Biochim. Biophys. Acta* **1758**, 1902-1921 (2006).

3 K. Trajkovic *et al.* Ceramide triggers budding of exosome vesicles into multivesicular endosomes. *Science* **319**, 1244-1247 (2008).

4 X. Zha, L. M. Pierini, P. L. Leopold, P. J. Skiba, I. Tabas & F. R. Maxfield. Sphingomyelinase treatment induces ATP-independent endocytosis. *J. Cell Biol.* **140**, 39-47 (1998).

5 N. W. Andrews, P. E. Almeida & M. Corrotte. Damage control: cellular mechanisms of plasma membrane repair. *Trends Cell Biol.* **24**, 734-742 (2014).

6 N. Kosaka, H. Iguchi, Y. Yoshioka, F. Takeshita, Y. Matsuki & T. Ochiya. Secretory mechanisms and intercellular transfer of microRNAs in living cells. *J. Biol. Chem.* **285**, 17442-17452 (2010).

7 C. J. Clarke, E. A. Cloessner, P. L. Roddy & Y. A. Hannun. Neutral sphingomyelinase 2 (nSMase2) is the primary neutral sphingomyelinase isoform activated by tumour necrosis factor-α in MCF-7 cells. *Biochem. J* **435**, 381-390 (2011).

8 M. Adada, C. Luberto & D. Canals. Inhibitors of the sphingomyelin cycle: Sphingomyelin synthases and sphingomyelinases. *Chem. Phys. Lipids* **197**, 45-59 (2016).

9 R.-D. Duan, U. Hindorf, Y. Cheng, P. Bergenzaun, M. Hall, E. Hertervig & Å. Nilsson. Changes of activity and isoforms of alkaline sphingomyelinase (nucleotide pyrophosphatase phosphodiesterase 7) in bile from patients undergoing endoscopic retrograde cholangiopancreatography. *BMC Gastroenterol.* **14**, 138 (2014).

10 Å. Nilsson. The presence of sphingomyelin- and ceramide-cleaving enzymes in the small intestinal tract. *Biochim. Biophys. Acta* **176**, 339-347 (1969).

11 R.-D. Duan. Alkaline sphingomyelinase: an old enzyme with novel implications. *Biochim. Biophys. Acta* **1761**, 281-291 (2006).

12 Y. Zhang *et al.* Crucial role of alkaline sphingomyelinase in sphingomyelin digestion: a study on enzyme knockout mice. *J. Lipid Res.* **52**, 771-781 (2011).

13 J. Kunisawa & H. Kiyono. Sphingolipids and epoxidized lipid metabolites in the control of gut immunosurveillance and allergy. *Front. Nutr.* **3**, 3 (2016).

14 H. Vesper, E.-M. Schmelz, M. N. Nikolova-Karakashian, D. L. Dillehay, D. V. Lynch & A. H. Merrill. Sphingolipids in food and the emerging importance of sphingolipids to nutrition. *J. Nutr.* **129**, 1239-1250 (1999).

15 S. Tomiuk, K. Hofmann, M. Nix, M. Zumbansen & W. Stoffel. Cloned mammalian neutral sphingomyelinase: Functions in sphingolipid signaling? *Proc. Natl. Acad. Sci. U. S. A.* **95**, 3638-3643 (1998).

16 S. Tomiuk, M. Zumbansen & W. Stoffel. Characterization and subcellular localization of murine and human magnesium-dependent neutral sphingomyelinase. *J. Biol. Chem.* **275**, 5710-5717 (2000).

17 H. Sawai, N. Domae, N. Nagan & Y. A. Hannun. Function of the cloned putative neutral sphingomyelinase as lyso-platelet activating factor-phospholipase C. *J. Biol. Chem.* **274**, 38131-38139 (1999).

18 M. Zumbansen & W. Stoffel. Neutral sphingomyelinase 1 deficiency in the mouse causes no lipid storage disease. *Mol. Cell. Biol.* **22**, 3633-3638 (2002).

19 B. Liu, D. F. Hassler, G. K. Smith, K. Weaver & Y. A. Hannun. Purification and characterization of a membrane bound neutral pH optimum magnesium-dependent and

phosphatidylserine-stimulated sphingomyelinase from rat brain. *J. Biol. Chem.* **273**, 34472-34479 (1998).
20 W. Stoffel, B. Jenke, B. Blöck, M. Zumbansen & J. Koebke. Neutral sphingomyelinase 2 (smpd3) in the control of postnatal growth and development. *Proc. Natl. Acad. Sci. U. S. A.* **102**, 4554-4559 (2005).
21 I. Aubin *et al.* A deletion in the gene encoding sphingomyelin phosphodiesterase 3 (Smpd3) results in osteogenesis and dentinogenesis imperfecta in the mouse. *Nat. Genet.* **37**, 803-805 (2005).
22 K. Bernardo *et al.* Purification and characterization of a magnesium-dependent neutral sphingomyelinase from bovine brain. *J. Biol. Chem.* **275**, 7641-7647 (2000).
23 O. Krut, K. Wiegmann, H. Kashkar, B. Yazdanpanah & M. Krönke. Novel tumor necrosis factor-responsive mammalian neutral sphingomyelinase-3 is a C-tail-anchored protein. *J. Biol. Chem.* **281**, 13784-13793 (2006).
24 T. Yabu, A. Shimuzu & M. Yamashita. A novel mitochondrial sphingomyelinase in zebrafish cells. *J. Biol. Chem.* **284**, 20349-20363 (2009).
25 B. X. Wu, V. Rajagopalan, P. L. Roddy, C. J. Clarke & Y. A. Hannun. Identification and characterization of murine mitochondria-associated neutral sphingomyelinase (MA-nSMase), the mammalian sphingomyelin phosphodiesterase 5. *J. Biol. Chem.* **285**, 17993-18002 (2010).
26 L. J. Siskind. Mitochondrial ceramide and the induction of apoptosis. *J. Bioenerg. Biomembr.* **37**, 143-153 (2005).
27 M. Colombini. Ceramide channels and their role in mitochondria-mediated apoptosis. *Biochim. Biophys. Acta* **1797**, 1239-1244 (2010).
28 J. N. Kanfer, O. M. Young, D. Shapiro & R. O. Brady. The metabolism of sphingomyelin. I. Purification and properties of a sphingomyelin-cleaving enzyme from rat liver tissue. *J. Biol. Chem.* **241**, 1081-1084 (1966).
29 P. B. Schneider & E. P. Kennedy. Sphingomyelinase in normal human spleens and in spleens from subjects with Niemann-Pick disease. *J. Lipid Res.* **8**, 202-209 (1967).
30 E. H. Schuchman. Acid sphingomyelinase, cell membranes and human disease: Lessons from Niemann–Pick disease. *FEBS Lett.* **584**, 1895-1900 (2010).
31 R. W. Jenkins, D. Canals & Y. A. Hannun. Roles and regulation of secretory and lysosomal acid sphingomyelinase. *Cell. Signal.* **21**, 836-846 (2009).
32 H. Schulze & K. Sandhoff. Lysosomal lipid storage diseases. *Cold Spring Harb. Perspect. Biol.* **3**, a004804 (2011).
33 E. Schuchman, M. Suchi, T. Takahashi, K. Sandhoff & R. Desnick. Human acid sphingomyelinase. Isolation, nucleotide sequence and expression of the full-length and alternatively spliced cDNAs. *J. Biol. Chem.* **266**, 8531-8539 (1991).
34 E. L. Smith & E. H. Schuchman. The unexpected role of acid sphingomyelinase in cell death and the pathophysiology of common diseases. *FASEB J.* **22**, 3419-3431 (2008).
35 J. Kornhuber, C. Rhein, C. P. Müller & C. Mühle. Secretory sphingomyelinase in health and disease. *Biol. Chem.* **396**, 707-736 (2015).
36 R. W. Jenkins *et al.* Regulated secretion of acid sphingomyelinase: implications for selectivity of ceramide formation. *J. Biol. Chem.* **285**, 35706-35718 (2010).
37 E. Gulbins, S. Dreschers, B. Wilker & H. Grassmé. Ceramide, membrane rafts and infections. *J. Mol. Med.* **82**, 357-363 (2004).
38 L. J. Heung, C. Luberto & M. Del Poeta. Role of sphingolipids in microbial pathogenesis. *Infect. Immun.* **74**, 28-39 (2006).
39 P. Cossart & A. Helenius. Endocytosis of viruses and bacteria. *Cold Spring Harb. Perspect. Biol.* **6**, a016972 (2014).

40 O. Utermöhlen, J. Herz, M. Schramm & M. Krönke. Fusogenicity of membranes: the impact of acid sphingomyelinase on innate immune responses. *Immunobiology* **213**, 307-314 (2008).

41 A. Simonis, S. Hebling, E. Gulbins, S. Schneider-Schaulies & A. Schubert-Unkmeir. Differential activation of acid sphingomyelinase and ceramide release determines invasiveness of Neisseria meningitidis into brain endothelial cells. *PLoS Pathog.* **10**, e1004160 (2014).

42 H. Grassme *et al.* Host defense against Pseudomonas aeruginosa requires ceramide-rich membrane rafts. *Nat. Med.* **9**, 322-330 (2003).

43 M. C. Fernandes, M. Cortez, A. R. Flannery, C. Tam, R. A. Mortara & N. W. Andrews. Trypanosoma cruzi subverts the sphingomyelinase-mediated plasma membrane repair pathway for cell invasion. *J. Exp. Med.* **208**, 909-921 (2011).

44 M. E. Miller, S. Adhikary, A. A. Kolokoltsov & R. A. Davey. Ebolavirus requires acid sphingomyelinase activity and plasma membrane sphingomyelin for infection. *J. Virol.* **86**, 7473-7483 (2012).

45 E. Avota, E. Gulbins & S. Schneider-Schaulies. DC-SIGN mediated sphingomyelinase-activation and ceramide generation is essential for enhancement of viral uptake in dendritic cells. *PLoS Pathog.* **7**, e1001290 (2011).

46 K. J. Szretter, A. L. Balish & J. M. Katz. Influenza: propagation, quantification, and storage. *Curr. Protoc. Microbiol.*, 15G. 11.11-15G. 11.22 (2006).

47 L. J. Reed & H. Muench. A simple method of estimating fifty per cent endpoints. *Am. J. Epidemiol.* **27**, 493-497 (1938).

48 E. Spackman *et al.* Development of a real-time reverse transcriptase PCR assay for type A influenza virus and the avian H5 and H7 hemagglutinin subtypes. *J. Clin. Microbiol.* **40**, 3256-3260 (2002).

49 J. A. Richt, K. M. Lager, D. F. Clouser, E. Spackman, D. L. Suarez & K.-J. Yoon. Real-time reverse transcription–polymerase chain reaction assays for the detection and differentiation of North American swine influenza viruses. *J. Vet. Diagn. Invest.* **16**, 367-373 (2004).

50 M. J. Slomka *et al.* Real time reverse transcription (RRT)-polymerase chain reaction (PCR) methods for detection of pandemic (H1N1) 2009 influenza virus and European swine influenza A virus infections in pigs. *Influenza Other Respi. Viruses* **4**, 277-293 (2010).

51 C. Tam *et al.* Exocytosis of acid sphingomyelinase by wounded cells promotes endocytosis and plasma membrane repair. *J. Cell Biol.* **189**, 1027-1038 (2010).

52 X. Li, E. Gulbins & Y. Zhang. Oxidative stress triggers Ca2+-dependent lysosome trafficking and activation of acid sphingomyelinase. *Cell. Physiol. Biochem.* **30**, 815-826 (2012).

53 M. W. Spence, D. Byers, F. Palmer & H. W. Cook. A new Zn2+-stimulated sphingomyelinase in fetal bovine serum. *J. Biol. Chem.* **264**, 5358-5363 (1989).

54 D. S. Dimitrov. Virus entry: molecular mechanisms and biomedical applications. *Nat. Rev. Microbiol.* **2**, 109-122 (2004).

55 S. Luisoni *et al.* Co-option of membrane wounding enables virus penetration into cells. *Cell Host Microbe* **18**, 75-85 (2015).

56 G. P. Leser & R. A. Lamb. Influenza virus assembly and budding in raft-derived microdomains: a quantitative analysis of the surface distribution of HA, NA and M2 proteins. *Virology* **342**, 215-227 (2005).

57 J. B. Ulmer, U. Valley & R. Rappuoli. Vaccine manufacturing: challenges and solutions. *Nat. Biotechnol.* **24**, 1377-1383 (2006).

58 A. Y.-C. Hu *et al.* Production of inactivated influenza H5N1 vaccines from MDCK cells in serum-free medium. *PLoS One* **6**, e14578 (2011).

59 M. J. Gerl *et al.* Quantitative analysis of the lipidomes of the influenza virus envelope and MDCK cell apical membrane. *J. Cell Biol.* **196**, 213-221 (2012).

60 R. W. Jenkins *et al.* A novel mechanism of lysosomal acid sphingomyelinase maturation: requirement for carboxyl-terminal proteolytic processing. *J. Biol. Chem.* **286**, 3777-3788 (2011).

61 K. Lindblad-Toh *et al.* Genome sequence, comparative analysis and haplotype structure of the domestic dog. *Nature* **438**, 803-819 (2005).

62 D. L. Medina *et al.* Transcriptional activation of lysosomal exocytosis promotes cellular clearance. *Dev. Cell* **21**, 421-430 (2011).

63 M. M. Salimans, H. A. Van Heugten, H. Van Steeg & H. O. Voorma. The effect of serum deprivation on the initiation of protein synthesis in mouse neuroblastoma cells. *Biochim. Biophys. Acta* **824**, 16-26 (1985).

64 L. Sun *et al.* Serum deprivation elevates the levels of microvesicles with different size distributions and selectively enriched proteins in human myeloma cells in vitro. *Acta Pharmacol. Sin.* **35**, 381-393 (2014).

65 S. Pirkmajer & A. V. Chibalin. Serum starvation: caveat emptor. *Am. J. Physiol. Cell Physiol.* **301**, C272-C279 (2011).

66 D. Vester *et al.* Real-time RT-qPCR assay for the analysis of human influenza A virus transcription and replication dynamics. *J. Virol. Methods* **168**, 63-71 (2010).

67 J.-T. Jan, S. Chatterjee & D. E. Griffin. Sindbis virus entry into cells triggers apoptosis by activating sphingomyelinase, leading to the release of ceramide. *J. Virol.* **74**, 6425-6432 (2000).

68 H. Grassmé, A. Riehle, B. Wilker & E. Gulbins. Rhinoviruses infect human epithelial cells via ceramide-enriched membrane platforms. *J. Biol. Chem.* **280**, 26256-26262 (2005).

69 S. Kummer *et al.* Alteration of protein levels during influenza virus H1N1 infection in host cells: a proteomic survey of host and virus reveals differential dynamics. *PLoS One* **9**, e94257 (2014).

70 S. Elojeimy *et al.* New insights on the use of desipramine as an inhibitor for acid ceramidase. *FEBS Lett.* **580**, 4751-4756 (2006).

71 M. Kölzer, N. Werth & K. Sandhoff. Interactions of acid sphingomyelinase and lipid bilayers in the presence of the tricyclic antidepressant desipramine. *FEBS Lett.* **559**, 96-98 (2004).

72 C. De Duve, T. De Barsy, B. Poole & P. Tulkens. Lysosomotropic agents. *Biochem. Pharmacol.* **23**, 2495-2531 (1974).

73 U. E. Honegger, A. A. Roscher & U. N. Wiesmann. Evidence for lysosomotropic action of desipramine in cultured human fibroblasts. *J. Pharmacol. Exp. Ther.* **225**, 436-441 (1983).

74 J. Fontana, G. Cardone, J. B. Heymann, D. C. Winkler & A. C. Steven. Structural changes in Influenza virus at low pH characterized by cryo-electron tomography. *J. Virol.* **86**, 2919-2929 (2012).

75 A. Yoshimura, K. Kuroda, K. Kawasaki, S. Yamashina, T. Maeda & S.-I. Ohnishi. Infectious cell entry mechanism of influenza virus. *J. Virol.* **43**, 284-293 (1982).

76 F. G. Tafesse, S. Sanyal, J. Ashour, C. P. Guimaraes, M. Hermansson, P. Somerharju & H. L. Ploegh. Intact sphingomyelin biosynthetic pathway is essential for intracellular transport of influenza virus glycoproteins. *Proc. Natl. Acad. Sci. U. S. A.* **110**, 6406-6411 (2013).

77 N. H. Petersen *et al.* Transformation-associated changes in sphingolipid metabolism sensitize cells to lysosomal cell death induced by inhibitors of acid sphingomyelinase. *Cancer Cell* **24**, 379-393 (2013).

4.6 FIGURES

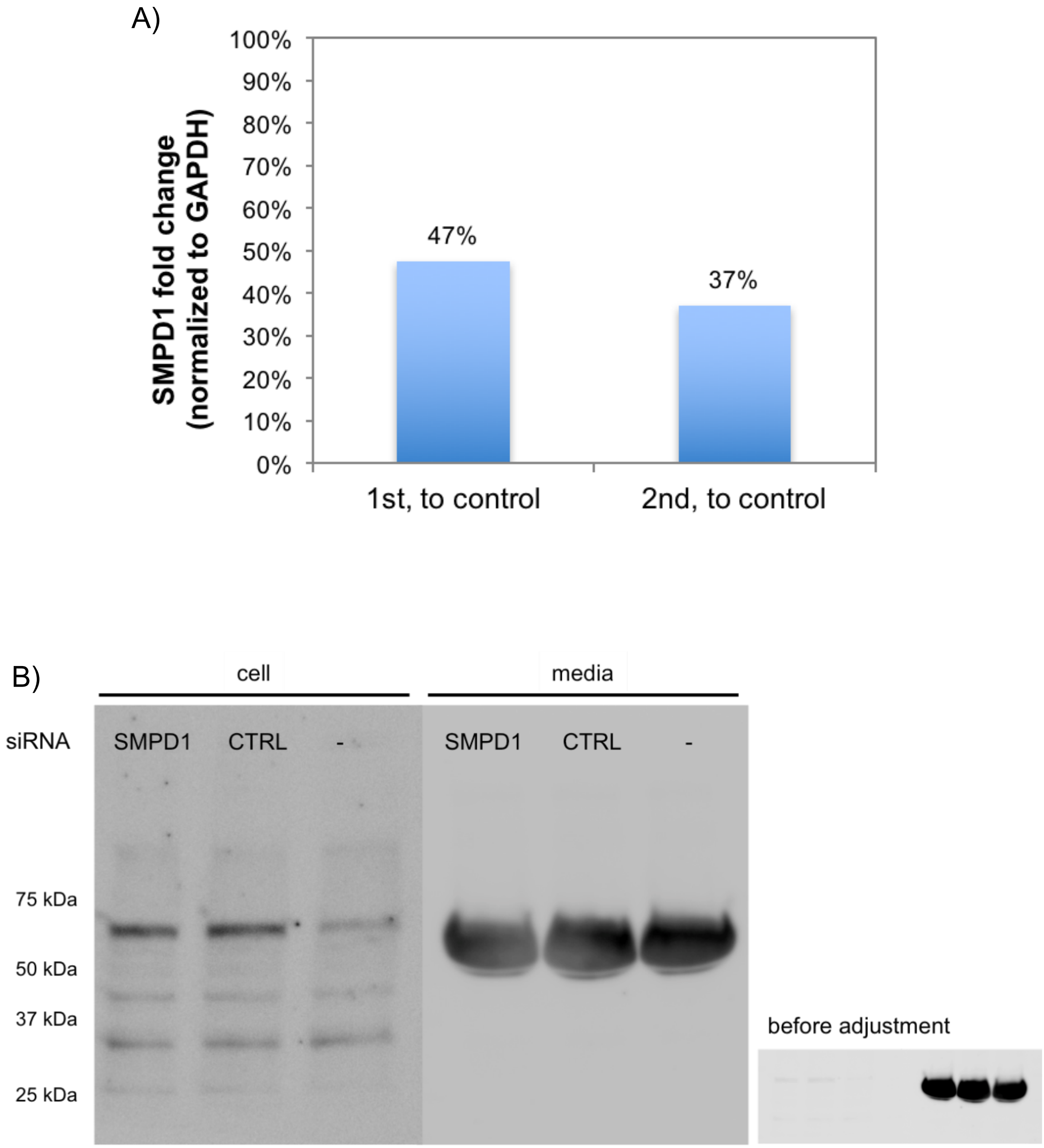

Figure 4.1 (cont.)

Figure 4.1 (cont.)

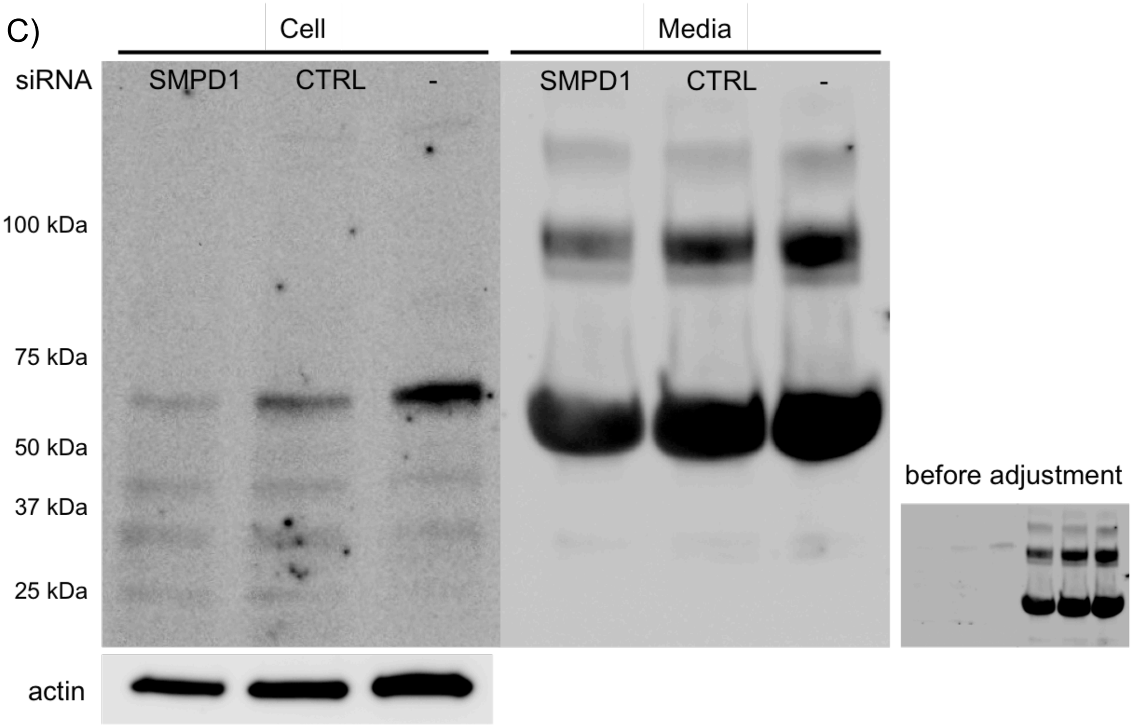

Figure 4.1. Detection of SMPD1 gene expression level (A) and SMPD1 proteins in MDCK cells and their conditioned culture media (B, C) after RNAi. A: MDCK cells were transfected with siRNAs against SMPD1, and negative control RNAs for 6 h. The cells were transferred to fresh media consisting of DMEM with 10% FBS. After 42 h, cellular RNAs were extracted from the cells and subjected to RT-qPCR. The SMPD1 mRNA levels relative to GAPDH (housekeeping) mRNA level of SMPD1 siRNA treated cells were compared to those of control siRNA treated cells. B: MDCK cells were transfected with siRNAs against SMPD1, and negative control RNAs for 6 h. The cells were transferred to fresh media consisting of DMEM with 10% FBS twice, once right after the transfection and again 24 h prior to sample collection. For comparison, cells that were not transfected with siRNA were cultured in the same media for the same time intervals prior to sample collection. 10 µl aliquots of the media that had been conditioned for 24 h were also collected from the transfected and non-transfected cells and subjected to Western blot. C: MDCK cells were transfected the same as A. The media were substituted to DMEM with 0.2% BSA once after the transfection. Cells that were not transfected with siRNA were also cultured under the same conditions. 20 µL aliquots of media that had been conditioned for 42 h were collected for Western blot. SMPD1: cells subjected to siRNA knockdown of SMPD1; CTRL: cells transfected with control siRNA; (-) MDCK cells that were not transfected.

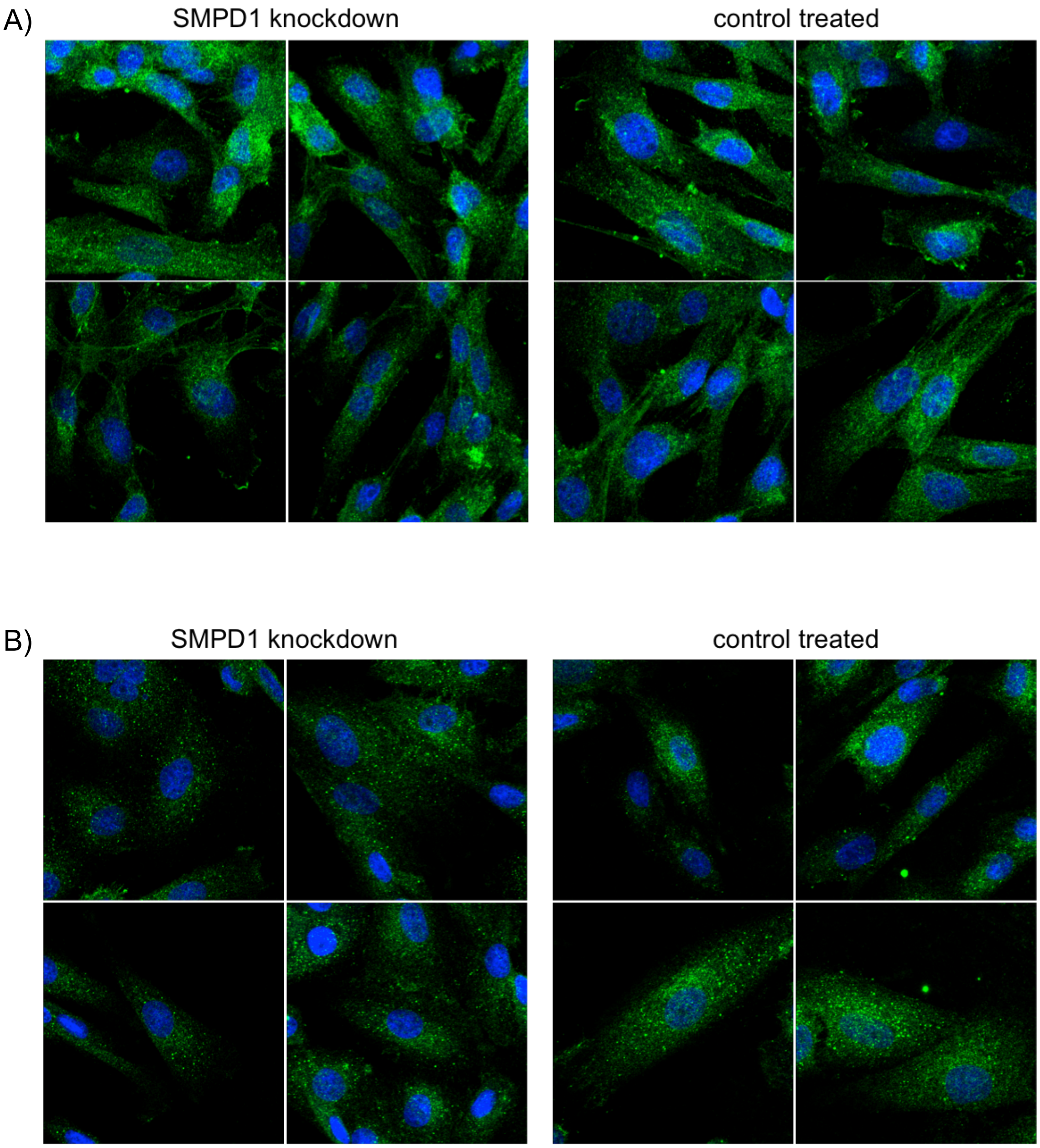

Figure 4.2. Confocal fluorescence microscopy images of nuclear proteins in infected cells with and without knockdown of SMPD1. The z-projection images were produced by combining the z-stack images collected with 0.25 μm interval between two adjacent stacks. A: MDCK cells were transfected with siRNAs against SMPD1, negative control RNAs for 6 h, and then the cells were incubated in fresh siRNA-free media consisting of DMEM with 10% FBS for 48 h after the transfection. At 48 h post-transfection, the cells were infected with influenza virus at ~10 MOI. At 1.5 hpi the cells were fixed, permeabilized and immunolabeled against influenza A nucleoprotein. B: MDCK cells were transfected the same as A, where the media were changed to DMEM with 0.2% BSA after the transfection. Infection, fixation, permeabilization and immunolabeling were performed the same as in A.

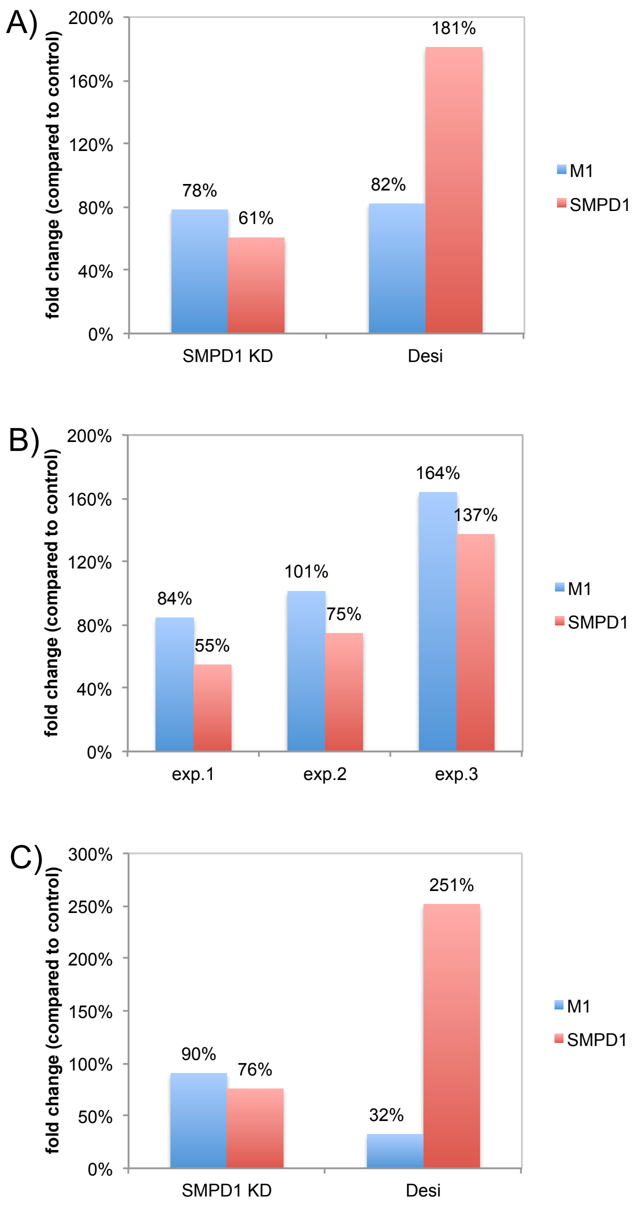

Figure 4.3. The relative levels of M1 and SMPD1 in the infected MDCK cells after knockdown of SMPD1 or desipramine treatment. A: Fold change in virus M1 RNA and SMPD1 mRNA levels measured in SMPD1 knockdown cells and desipramine-treated cells relative to GAPDH (the housekeeping gene) compared to control siRNA treated cells at 1.5 hpi. The cells were transfected, incubated in 10% FBS, and then infected as described in Figure 4.2A. For desipramine treatment, the cells were treated with 25 µM of Desipramine overnight prior to the infection. B. Fold change in virus M1 RNA and SMPD1 level of three repeats of SMPD1 knockdown cells relative to GAPDH compared to control siRNA treated cells at 1.5 hpi. The cells were transfected, incubated in 0.2% FBS, and then infected as described above. C: Fold change in M1 and SMPD1 at 8 hpi. The cells were treated in the same as A.

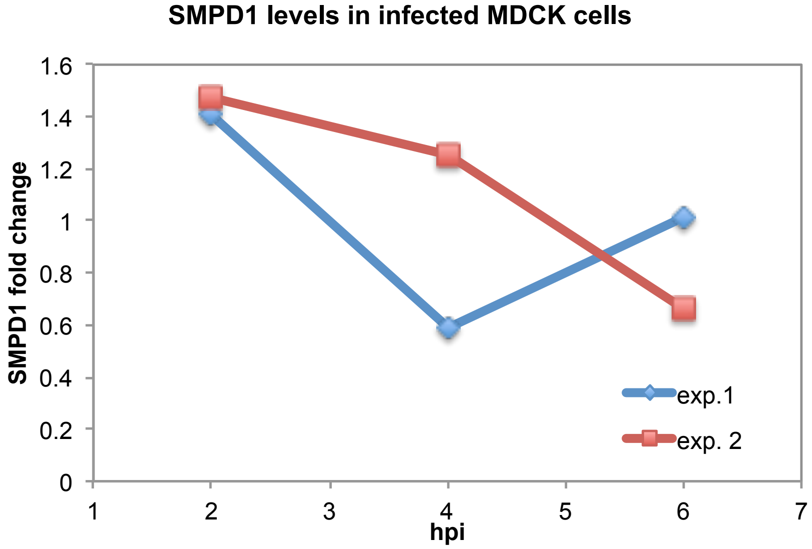

Figure 4.4. SMPD1 expression levels change with time post-influenza infection. MDCK cells were infected with influenza virus at ~10 MOI. The total RNAs were collected at the indicated post-infection time and the levels of SMPD1 mRNA were measured by RT-qPCR.

CHAPTER 5

MANIPULATING PROTEIN CORONA COMPOSITION BY PRE-COATING THE NANOPARTICLES WITH PROTEINS AND ITS IMPACT ON CELLULAR UPTAKE[*]

5.1 INTRODUCTION

Conventional drug administration would benefit from implementing efficient drug delivery systems. Improving drug delivery systems so that they efficiently target the drug to the diseased tissue, and not healthy cells, is expected to lower the required drug dose and reduce possible side effects. To achieve these, smart delivery systems have been designed from various materials and implemented in order to enhance target specificity, circulation time, and drug release profiles.[1-4]

Nanotechnology has been heavily exploited for these novel delivery systems. Nanoparticle-based targeted drug delivery offers multiple advantages over conventional drug

---

[*] This chapter presents portions of work which appeared in and has been reprinted with permission from:
Biomaterials. Mirshafiee, V., Kim, R., Park, S., Mahmoudi, M. & Kraft, M. L. "Impact of protein pre-coating on the protein corona composition and nanoparticle cellular uptake", *Biomaterials* **75**, 295-304 (2016).
The publication in Biomaterials was coauthored by Raehyun Kim, Vahid Mirshafiee, Soyun Park, Morteza Mahmoudi, and Mary L. Kraft. V.M. planned experiment, prepared and characterized the nanoparticles, and performed LC-MS/MS analysis and flow cytometry. R.K. performed protein separation, prepared cell samples for flow cytometry and microscopy, performed microscopy, immunodot blot and analyzed the data. S.P. prepared samples for microscopy and performed immunodot blot with RK's assistance. MM planned experiments and assisted data interpretation. M.L.K. planned experiments and assisited data interpretation.
We thank Prof. Ed Roy for providing the RAW 264.7 cell line and Prof. Catherine J. Murphy for using the ZetaPALS instrument. Portions of this work were carried out in the Flow Cytometry and Protein Sciences Facility in the Roy J. Carver Biotechnology Center, and the Microscopy and Imaging Facility in the Carl R. Woese Institute for Genomic Biology at the University of Illinois at Urbana-Champaign. A portion of this work was carried out in the Frederick Seitz Materials Research Laboratory Central Research Facilities, University of Illinois. This work was partially supported by a 3M Corporate Fellowship (to V.M.), a Drickamer Graduate Research Fellowship (to R.K.), the National Science Foundation (NSF) REU site: nano@illinois REU - Summer Nanotechnology Research Experience for Undergraduates program under EEC-1359454, and by the Department of Chemical and Biomolecular Engineering at the University of Illinois, Urbana-Champaign

administration. The small sizes of the nanoparticles allow extravasation through blood vessels and tissues.[5] This is especially advantageous for targeting solid tumors because tumor vasculature is much more permeable than normal vasculature due to its defective structure,[2,6] which is known as the enhanced permeability and retention (EPR) effect.[7] By designing nano-sized drug delivery systems that penetrate tumor blood vessels, but not normal ones, which is called passive targeting, it would be possible to selectively target solid tumors. Another advantage of using nanoparticle systems for drug delivery is that the surfaces of the nanoparticles can be easily functionalized and modified for more specific targeting,[5] which is also called active targeting. Recently, active targeting has been heavily explored as information on the surface receptors or epitopes overexpressed in cancer cells has become available.[2] Various ligands (folate[8] and transferrin[9,10]), antibodies (anti-HER2[11] and anti-CD19[12]) and peptides (RDG peptide[13,14]) have been exploited for targeting surface proteins that are known to be overexpressed in cancer cells. However, most active targeting strategies have not been successful in vivo, in part because the plasma proteins that adsorb on the nanoparticles, namely the protein corona, affects uptake efficiency,[15] drug release profiles[16] and biodistritution.[17,18,19] Polyethylene glycol (PEG) has been grafted to the nanoparticles to lower this protein binding and increase circulation time, but this doesn't completely inhibit the adsorption of plasma proteins.[20]

A possible alternative strategy is to utilize the proteins in the blood that form the protein corona, instead of removing them, for targeting. The surface of the nanoparticle can be manipulated for enriching the protein corona with certain desired proteins. For instance, a polysorbate-80 pre-coating on the nanoparticles enriched the protein corona with apolipoprotein B and E, which could enhance the transport of the nanoparticle across the brain blood barrier.[21]

Here we examined whether manipulating the protein corona composition is feasible and useful for active targeting. Specifically, we assessed whether enriching certain plasma proteins in the protein corona can enhance targeting efficiency and uptake by select cells. Although undesired in most targeted anticancer drug delivery applications, opsonin-triggered endocytosis in immune cells was utilized as a model system to evaluate targeting efficiency of the nanoparticles and to test the feasibility of our approach, because it is very well established and it may be useful for treating autoimmune diseases or diseases of immune cells. Silica nanoparticles were pre-coated with γ-globulins to enrich the protein corona with opsonins when the nanoparticles were exposed to human plasma solutions that mimic in vivo environment. Human serum albumin (HSA), one of the most abundant proteins in the blood, was used for pre-coating as a control. These pre-coating significantly altered protein corona compositions when the pre-coated nanoparticles were exposed to the diluted human plasma. In particular, γ-globulins pre-coating recruited significantly more opsonins to the protein corona as compared to the HSA pre-coated nanoparticles or the bare nanoparticles. Pre-coating the nanoparticles with γ-globulins increased their uptake by RAW 264.7 mouse macrophage cells compared to the bare nanoparticles. However, the cellular uptake of these nanoparticles was significantly decreased when a protein corona was formed on the γ-globulin pre-coated silica nanoparticles. The cellular uptake of nanoparticles that were functionalized with a protein corona were similar regardless of whether or not they were pre-coated with γ-globulins even though the opsonin content was higher in the protein coronas of the γ-globulin pre-coated nanoparticles. Our finding indicates that the protein corona shielded the opsonins from interacting with the surface receptors on the cells, thereby compromising the targeting. This suggests that for efficient targeting, the spatial distribution of the target moieties on the nanoparticles should be considered more important than their overall abundance in the protein corona.

5.2 MATERIALS AND METHODS

5.2.1 Materials

Unless otherwise indicated, all chemicals were purchased from Sigma-Aldrich. Carboxyethyl-silanetriol sodium salt, 25% in water, was purchased from Gelest Inc.

Concentrated ammonia was purchased from Fisher Scientific. The bicinchoninic acid (BCA) colorimetric protein assay kit was obtained from Pierce Biotechnology. 4-20% polyacrylamide precast gels and QC Colloidal Coomassie Stain were purchased from Bio-Rad. The MSG-Trypsin for protein digestion was purchased from G-Biosciences (St. Louis, USA). Clarity Western ECL substrate was obtained from Bio-Rad. The glass-bottomed dishes for confocal fluorescence microscopy were purchased from CellVis. Paraformaldehyde was purchased from Electron Microscopy Sciences. Rabbit anti-CD64 antibody (sc-15364) was purchased from Santa Cruz Biotechnology. Alexa488 goat anti-rabbit IgG, Hoechst 33342 nuclear stain, Image-iT FX Signal Enhancer, and OptiMEM serum free media were purchased from Life Technologies. RAW 264.7 cells were kindly provided by Prof. Ed Roy (University of Illinois at Urbana-Champaign, USA).

5.2.2 Synthesis of carboxylic acid-functionalized silica nanoparticles and carboxylic acid-functionalized fluorescent silica nanoparticles

The silica nanoparticles were synthesized and functionalized as previously described.[22]

5.2.3 Preparation of HSA, γ-globulin pre-treated nanoparticles and hard corona nanoparticles

The silica nanoparticles were pre-coated with HSA and γ-globulin following the published protocol.[22] The hard corona was formed as described in the same publication.[22]

5.2.4 Measurement of the sizes and zeta potentials of the nanoparticles

The zeta-potential and size measurements for the uncoated (control) nanoparticles (UC-NPs), HSA pre-coated nanoparticles (HSA-NPs) the γ-globulin pre-coated nanoparticles (GG-NPs), and the nanoparticles coated with a protein corona (corona-UC-NPs, corona-HSA-NPs, and corona-GG-NPs) were performed in OptiMEM using a Brookhaven ZetaPALS instrument. Scanning electron microscopy (SEM) was also used to measure the size of the nanoparticles. UC-NPs, protein pre-coated nanoparticles, and nanoparticles with hard-coronas were placed on 5 mm x 5 mm silicon substrates and coated with Au/Pd using an Emitech K575 sputter coater.

The nanoparticles were imaged with a Hitachi S-4800 high-resolution scanning electron microscope. For each sample, the sizes of 50 nanoparticles were measured using ImageJ.

5.2.5 Measurement of the amount of protein on the nanoparticles

The amounts of proteins on the nanoparticles were quantified using a BCA assay as previously described.[22]

5.2.6 Sodium dodecyl sulfate polyacrylamide gel electrophoresis (SDS-PAGE) analysis of hard corona

The proteins on the nanoparticles were denatured by heating the nanoparticles in Laemmli sample buffer for 5-10 min at 85 °C and separated by electrophoresis on 4-20% polyacrylamide precast gels. The resulting gels were fixed in fixing solution (40% methanol, 10% acetic acid and 50% water), stained with QC Colloidal Coomassie Stain overnight and destained in water for 2-3 h. Stained gels were imaged using an Image Quant LAS4010 image analyzer (GE Healthcare).

5.2.7 Identification of the protein corona composition by LC-MS/MS

The composition of the protein corona on each type of nanoparticle was identified by LC-MS/MS analysis, as described in the previous publication.[22]

5.2.8 Cell culture

RAW 264.7 cells (mouse macrophages) were cultured in Dulbecco's Modified Eagle Medium (DMEM) supplemented with 10% fetal bovine serum (FBS) and 1% penicillin/streptomycin in a 5% CO2 incubator at 37°C.

5.2.9 Flow cytometry analysis to evaluate cellular uptake of the nanoparticles

RAW 264.7 cells were used when they reached 50-70% confluence. The nanoparticles were suspended in the medium to make final concentration of 20 μg/mL immediately prior to incubation with cells. OptiMEM was used for serum-free culture conditions and DMEM with 10% FBS was used for experiments performed in the presence of serum. The cells were washed with PBS, incubated with nanoparticles in the appropriate medium for 2 or 6 h, and subjected to flow cytometry after thorough washing. The flow cytometry was performed with BD LSR II Flow Cytometry Analyser using a blue laser and a 575/26 bandpass filter.

5.2.10 Immunodot-blot assay for assessing ligand availability on the nanoparticles

The nanoparticles (GG-NPs, corona-GG-NPs, and corona-UC-NPs) in PBS (250 μg/mL) were spotted onto a pre-wetted polyvinylidene fluoride (PVDF) membrane and dried. Next, the membranes were blocked with 5% skim milk in PBS for 1 h on a shaker at room temperature, and incubated with goat anti-human IgG, IgM, IgA antibody (Jackson ImmunoResearch, 109-005-064) in 1% skim milk in PBS overnight at 4 °C. Membranes were washed three times with PBS for 5 min each, incubated with HRP-conjugated rabbit anti-goat antibody, and washed three times with PBS at room temperature. The resulting membrane was visualized by chemiluminescence and imaged using ImageQuant LAS 4000 Imager (GE Healthcare).

5.2.11 Confocal fluorescence microscopy

The cells were grown in glass-bottomed dishes and used for microscopy when they reached 50-70% confluence. The cells were washed with PBS and incubated with the nanoparticles in the same concentration as used for the corresponding flow cytometry experiment for 2 h in OptiMEM for serum-free culture conditions. Next, the cells were washed thoroughly with medium and PBS, and fixed with 4% paraformaldehyde for 15 min at room temperature. The nanoparticles were visualized with LSM700 confocal fluorescence microscope (Carl Zeiss) using a 555 nm laser for excitation of the nanoparticles. To assess whether the nanoparticle uptake was receptor mediated, RAW 264.7 cells grown on glass-bottomed petri dishes were incubated with nanoparticles in OptiMEM (concentration = 20 μg/mL) for 2 h, and then were washed with OptiMEM. The cells were fixed with 4% paraformaldehyde for 15 min at room temperature, and permeabilized with 0.1% Triton-X 100 in PBS for 10 min on ice. To prevent nonspecific binding, the samples were blocked with Image-iT FX Signal Enhancer (Life Technologies) for 30 min followed by 1% BSA in PBS for 20 min at room temperature. Then the cells were incubated with rabbit anti-CD64 in 1% BSA in PBS overnight at 4°C. After washing with 1% BSA in PBS 3 times, the samples were incubated with Alexa488 goat anti-rabbit IgG in 1% BSA in PBS, and washed three times with 1% BSA in PBS. Cell nuclei were stained with Hoechst 33342 following manufacturer's protocol for 15 min at room temperature. The cells were imaged with a LSM700 (Carl Zeiss) confocal microscope using a 555 nm, 488 nm, and 405 nm laser for excitation of the nanoparticles, CD64, and nuclei, respectively.

5.3 RESULTS

5.3.1 Characterization of γ-globulin and HSA pre-coated silica nanoparticles with and without protein corona

Carboxyl acid-functionalized silica nanoparticles were chemically conjugated to either γ-globulin or HSA. A BCA assay confirmed the presence of the proteins on the nanoparticles. EDC/NHS-activated silica nanoparticles had significantly more proteins than unactivated nanoparticles, which suggests that the proteins were chemically conjugated as well as physically adsorbed to the nanoparticles. To confirm covalent conjugation of the γ-globulin to the nanoparticles, the nanoparticles were treated with SDS to desorb physically bound proteins and subjected to a BCA assay. At least 60% of the γ-globulin remained on the nanoparticles even after SDS treatment. This indicates that the majority of the γ-globulin protein was covalently attached to the silica nanoparticles.

Next, the protein coronas were prepared on the naked (uncoated) nanoparticles, and the HSA and γ-globulin conjugated nanoparticles. To mimic the protein concentration in vivo and in cell culture, human plasma was diluted in PBS at final concentration of 55% and 10%, respectively, and these diluted plasma solutions were used for protein corona formation. The nanoparticles were incubated with the diluted human plasma solutions for 1 h at 37°C, and then were washed to remove the loosely bound proteins.

The sizes and zeta potentials of naked or uncoated nanoparticles (UC-NPs), HSA pre-coated nanoparticles (HSA-NPs), γ-globulin pre-coated nanoparticles (GG-NPs), and the human plasma-exposed nanoparticles without a pre-coating (corona-UC-NPs), pre-coated with HSA (corona-HSA-NPs) and γ-globulin (corona-GG-NPs) were characterized. The hydrodynamic diameters, diameters measured with SEM, and the zeta potentials of the nanoparticles are shown in Table 5.1. Pre-coating of the nanoparticles with HSA and γ-globulins significantly increased their hydrodynamic diameters, size distributions, and zeta potentials measured by DLS. The increased hydrodynamic diameters and size distributions could be indicative of particle aggregation, and not a thick layer of protein. Therefore, the sizes and the size distributions of the nanoparticles were also measured using SEM. The SEM measurements showed that indeed, some types of nanoparticles, especially the protein pre-coated nanoparticles, namely the HSA-NPs and GG-NPs, had aggregated. The increases in size resulting from the protein pre-coating on the individual nanoparticles were less than 10 nm (5 nm and 9 nm for HSA-NPs and GG-NPs respectively).

The nanoparticles that had been functionalized with a protein corona were also characterized. The hydrodynamic diameters of the corona-HSA-NPs and corona-GG-NPs were larger than those of the corona-UC-NPs, but smaller than those of the HSA-NPs and GG-NPs, the parent nanoparticles that lacked a protein corona. The SEM images indicated that protein corona formation seem to reduce the clustering of the protein pre-coated nanoparticles. When measured by SEM, the increased diameters resulting from protein corona formation on the individual nanoparticles were approximately 9 nm and 3 nm for HSA-NPs and GG-NPs, respectively. These are very small differences in comparison to the difference in the sizes of the between UC-NPs and corona-UC-NPs. This indicates that the loosely bound proteins from the pre-coating step were exchanged for plasma proteins during protein corona formation.

5.3.2 Characterization of protein corona composition using SDS-PAGE and LC-MS/MS

Next, to assess the influence of the pre-coating on the protein corona composition, the proteins of corona-HSA-NPs, corona-GG-NPs and UC-corona-NP were characterized. The proteins that were deposited onto the nanoparticles during the pre-coating step were identified (marked in black in Figure 5.2) by comparing the protein bands with the protein pre-coated nanoparticles that were not exposed to human plasma. The protein profiles for those three corona-coated particles were fairly similar, but the intensities of the protein bands were significantly different, as marked in red in Figure 5.2.

The protein corona composition of each type of nanoparticle was analyzed further with LC-MS/MS. The weight percent of each protein detected by LC-MS/MS was calculated using an exponentially modified protein abundance index (emPAI), as described in the literature.[23] The ten most abundant in the protein coronas of the nanoparticles are listed in Table 5.2.

The proteins detected in the protein corona of each nanoparticle were classified by their functions. As expected, the γ-globulin pre-coating enriched the protein corona with immunoglobulins and complement factors compared to the corona-HSA-NPs and the corona-UC-NPs. About 40% of the proteins detected in corona-GG-NPs were identified as immunoglobulins. In contrast, the portion of lipoproteins in the protein corona increased significantly when the nanoparticles had been pre-coated with HSA. Considering the amount of proteins measured on the GG-NPs and corona-GG-NPs, the pre-coated γ-globulins were estimated to make up about 55% of the immunoglobulins (and about 22% of total proteins) that were detected in the protein corona of the corona-GG-NPs. This result supports the hypothesis that the γ-globulin pre-coating recruits opsonins, such as immunoglobulins and complement factors, in the plasma to the protein corona.

5.3.3 Assessment of the cellular uptake of nanoparticles with and without the protein corona

We examined whether the high portion of opsonins in the protein corona increased the cellular uptake of the nanoparticles by macrophage cells. The opsonins, such as the complement factors and immunoglobulins, on the nanoparticles could interact with the receptors on the immune cells and initiate particle internalization. For example, immunoglobulins can bind to the Fc receptors on macrophages, which initiates nanoparticle internalization. However, the unactivated complement factors that were detected in the protein corona of the nanoparticles in this study are not reported to interact with immune cells. Therefore, we used RAW 264.7 mouse macrophage cells to investigate whether the enrichment of the protein corona with immunoglobulins increased nanoparticle internalization.

To measure the relative amount of internalized nanoparticles, fluorescent silica nanoparticles with and without the γ-globulin pre-coating were prepared as described above. Then the protein corona was formed by incubation in 55% human plasma solution for 1 h at 37°C, and washing in PBS. The RAW 264.7 cells were incubated with the resulting corona-UC-NPs and corona-GG-NPs in serum-free medium for 2 h at 37°C. After thorough washing, the cells were then examined with confocal fluorescence microscopy to visualize the internalized nanoparticles, or flow cytometry to quantify the amount of the nanoparticles inside the cells.

Although the corona-GG-NPs had a significantly higher portion of immunoglobulins in their protein corona than the corona-UC-NPs, the confocal fluorescence microscopy and flow cytometry experiments indicated little difference in the amounts of corona-GG-NPs and corona-UC-NPs internalized by RAW 264.7 cells. In contrast, confocal fluorescence microscopy showed that the GG-NPs, the γ-globulin pre-coated particles that were not exposed to the human plasma solution, were internalized substantially more than the nanoparticles functionalized protein coronas. This observation was also confirmed by flow cytometry. This finding indicates that the hard corona formed by exposing the GG-NPs to 55% human plasma solution shielded the immunoglobulins on the nanoparticle surface from interacting with their cellular receptors despite their high levels in the protein corona. The presence of serum in the cell culture medium (10% v/v) during nanoparticle incubation with the RAW 264.7 cells did not affect the uptake of GG-NPs, suggesting that the nanoparticles were rapidly internalized before the serum proteins could deposit on their surfaces and shield the γ-globulins. In addition, this indicates that the lowered cellular uptake of corona-GG-NPs compared to GG-NPs was due to the proteins on the surface of the particles, and not because of the presence of soluble proteins in the culture solution inhibited nanoparticle uptake. These results indicate that protein corona formation hinders the interactions between the immunoglobulins on corona-GG-NPs and the Fc receptors on the RAW 264.7 cells, thereby lowering the internalization of the corona-GG-NPs.

5.3.4 Evaluation of the interactions between opsonins on the nanoparticles and cellular Fc receptors

We further investigated whether the lowered cellular uptake of the corona-GG-NPs was because protein corona formation compromised specific interactions between the opsonins on the particles and the cellular Fc receptors. First, we compared the availability of the immunoglobulins on the GG-NPs, corona-GG-NPs, and corona-UC-NPs to binding partners by using immunodot blotting. A significantly higher level of immunoglobulins was detected on the surfaces of the GG-NPs than either type of nanoparticle that was coated with a protein corona. Even though LC-MS/MS detected more immunoglobulins were in the corona-GG-NPs than the corona-UC-NPs, the immunoglobulin levels detected on both corona-coated nanoparticles by immunodot-blot differed only slightly, indicating the availability of the immunoglobulins was compromised by protein corona formation. When GG-NPs were incubated in cell culture medium supplemented with 10% serum for 1 h, the availability of the immunoglobulins decreased to that of the corona-GG-NPs. Considering the similar levels of cellular uptake for the GG-NPs in serum-free medium and 10% serum-supplemented medium (Figure 5.5), this suggests that internalization of the nanoparticles occurs faster than the change in protein composition on the surface of the nanoparticles that could alter the extent of the nanoparticle uptake.

Next, we evaluated whether cellular uptake of the nanoparticles by RAW 264.7 macrophage cells involved interactions between the immunoglobulins on the nanoparticles and the cellular Fc receptors. The cells were allowed to internalize the GG-NPs, corona-GG-NPs, and corona-UC-NPs for 2 h, and then were washed and chemically fixed. Then CD64 (also known as FcγRI), a Fc receptor that has a high affinity for IgG, on the RAW 264.7 cells were labeled by immunofluorescence and visualized in parallel with the nanoparticles using confocal fluorescence microscopy (Figure 5.7). The GG-NPs were internalized significantly more than the other two types of nanoparticles, which is consistent with the data shown in Figure 5.4. More importantly, colocalization of GG-NPs with CD64 was higher than CD64 colocalization with the corona-GG-NPs and corona-UC-NPs. This indicates that these nanoparticles were internalized by a Fc receptor-mediated mechanism, and the presence of the other corona proteins hindered interactions between the immunoglobulins and the CD64 on the cell surface.

Overall, our data indicates that in spite of the higher amount of immunoglobulins on the surface of the nanoparticles, the other proteins that adsorb onto the nanoparticles during corona formation could prevent the immunoglobulins from interacting with the cellular Fc receptors, which lowers internalization of the nanoparticles.

5.4 DISCUSSION

We investigated whether pre-coating nanoparticles with selected proteins can be used to recruit a certain subset of plasma proteins to the protein corona for nanoparticle targeting. Although the prevention of opsonin-mediated nanoparticle endocytosis is typically desirable for anticancer therapy in clinical settings in order to obtain longer circulation times, we utilized this mechanism to test the feasibility of manipulating protein corona composition for nanoparticle targeting. Opsonin-mediated endocytosis is an ideal model system for evaluating the cellular uptake of the nanoparticles because the endocytosis mechanism that is elicited by the binding of opsonins to their cellular receptors is well established.[18,24]

We showed that composition of the protein corona can be manipulated by chemically conjugating certain proteins to the nanoparticle surface. The compositions of the protein coronas that formed on the uncoated, HSA pre-coated, and γ-globulin pre-coated nanoparticles were noticeably different. The pre-coating itself contributed to some of the differences in protein corona composition. However, the pre-coating also altered the identities of the plasma proteins that were recruited to the protein corona. For example, the HSA pre-coating reduced the amount of fibrinogen in the protein corona. Fibrinogen binding onto the nanoparticle surface can initiate an immune response by inducing inflammatory cytokine release,[19,25,26] therefore the reduction of fibrinogen content in the protein corona that formed on the HSA pre-coated nanoparticles could contribute to the increased circulation time of albumin-coated drugs in the body.[27,28] The γ-globulin pre-coating enriched the protein corona with opsonins, whereas almost no immunoglobulins were detected in the protein corona that formed on the HSA pre-coated and uncoated nanoparticles.

Receptor mediated endocytosis, more specifically phagocytosis, is likely the dominant mechanism of nanoparticle internalization observed in this study. Confocal fluorescence microscopy images clearly show that CD64, which is a Fc receptor with high affinity to IgG, was colocalized with the γ-globulin–pre-coated nanoparticles. Fc receptors are reported to be rapidly and selectively degraded after internalization.[29] Interestingly, CD64 fluorescence was markedly more intense when higher levels of nanoparticles were detected in the cells (Figure 5.7). This implies that the nanoparticles internalized with the Fc receptors may prevent Fc receptor degradation and slow down their turnover.

The finding that higher opsonin content in the protein corona does not translate to higher cellular uptake suggests that protein corona formation obstructs the direct interactions of the immunoglobulins with the cellular Fc receptors. Despite the noticeable difference in the protein corona composition, the availability of the immunoglobulins (Figure 5.6) and the cellular uptake of the corona-GG-NPs and corona-UC-NPs (Figure 5.5, and Figure 5.7) were only slightly different, and almost comparable. This suggests that the outermost proteins in the protein coronas that coated these particles lacked an affinity for the surface proteins, such as Fc receptors, on the RAW 264.7 cells.

The presence of 10% serum in the culture media did not alter the uptake of GG-NPs by RAW 264.7 cells (Figure 5.5), while nanoparticle incubation with this medium for 1 h reduced the immunoglobulins' ability to interact with antibodies (Figure 5.6), and thus, Fc receptors on the cell surface. This indicates that the receptor-mediated internalization of the nanoparticles in in vitro cell cultures (without agitation) likely occurs before the serum proteins are able to adsorb onto the nanoparticles. However, nanoparticles in vivo move quickly within the blood stream and encounter more proteins and metabolites than nanoparticles in a cell culture. Therefore, exposing the nanoparticles to biological fluid (*i.e.* plasma) in vitro using the proper conditions, such as using enough agitation at the physiological temperature prior to cell culture, would more closely mimic the uptake of nanoparticles in vivo and provide a more accurate projection for the outcome in vivo.

Overall, we showed that pre-coating nanoparticles with selected proteins may enrich the protein corona with certain plasma proteins that may be useful for targeting. However, the availability of the recruited target proteins may be compromised by the protein corona if other inactive corona proteins cover the targeting proteins. Therefore, the spatial orientation of the desired proteins in the corona must be carefully regulated for efficient nanoparticle targeting.

5.5 REFERENCES

1 R. Singh & J. W. Lillard. Nanoparticle-based targeted drug delivery. *Exp. Mol. Pathol.* **86**, 215-223 (2009).

2 O. M. Koo, I. Rubinstein & H. Onyuksel. Role of nanotechnology in targeted drug delivery and imaging: a concise review. *Nanomed. Nanotechnol. Biol. Med.* **1**, 193-212 (2005).

3 Y.-W. Wu, H. Goubran, J. Seghatchian & T. Burnouf. Smart blood cells and microvesicle-based Trojan Horse drug delivery: Merging blood transfusion and biomedical engineering expertise in the field of nanomedicine. *Transfusion Apheresis Sci.* **54**, 309-318 (2016).

4 R. Cheng, F. Meng, C. Deng, H.-A. Klok & Z. Zhong. Dual and multi-stimuli responsive polymeric nanoparticles for programmed site-specific drug delivery. *Biomaterials* **34**, 3647-3657 (2013).

5 T. M. Fahmy, P. M. Fong, A. Goyal & W. M. Saltzman. Targeted for drug delivery. *Mater. Today* **8**, 18-26 (2005).

6 Y. Matsumura & H. Maeda. A new concept for macromolecular therapeutics in cancer chemotherapy: mechanism of tumoritropic accumulation of proteins and the antitumor agent smancs. *Cancer Res.* **46**, 6387-6392 (1986).

7 V. Torchilin. Tumor delivery of macromolecular drugs based on the EPR effect. *Adv. Drug Del. Rev.* **63**, 131-135 (2011).

8 S. Ni, S. M. Stephenson & R. J. Lee. Folate receptor targeted delivery of liposomal daunorubicin into tumor cells. *Anticancer Res.* **22**, 2131-2135 (2001).

9 O. Ishida, K. Maruyama, H. Tanahashi, M. Iwatsuru, K. Sasaki, M. Eriguchi & H. Yanagie. Liposomes bearing polyethyleneglycol-coupled transferrin with intracellular targeting property to the solid tumors in vivo. *Pharm. Res.* **18**, 1042-1048 (2001).

10 K. Maruyama *et al.* Intracellular targeting of sodium mercaptoundecahydrododecaborate (BSH) to solid tumors by transferrin-PEG liposomes, for boron neutron-capture therapy (BNCT). *J. Control. Release* **98**, 195-207 (2004).

11 J. W. Park *et al.* Anti-HER2 immunoliposomes enhanced efficacy attributable to targeted delivery. *Clin. Cancer Res.* **8**, 1172-1181 (2002).

12 P. Sapra & T. Allen. Ligand-targeted liposomal anticancer drugs. *Prog. Lipid Res.* **42**, 439-462 (2003).

13 A. Mitra, J. Mulholland, A. Nan, E. Mcneill, H. Ghandehari & B. R. Line. Targeting tumor angiogenic vasculature using polymer–RGD conjugates. *J. Control. Release* **102**, 191-201 (2005).

14 J. Hou, Y. Diao, W. Li, Z. Yang, L. Zhang, Z. Chen & Y. Wu. RGD peptide conjugation results in enhanced antitumor activity of PD0325901 against glioblastoma by both tumor-targeting delivery and combination therapy. *Int. J. Pharm.* **505**, 329-340 (2016).

15 A. Lesniak, F. Fenaroli, M. P. Monopoli, C. Åberg, K. A. Dawson & A. Salvati. Effects of the presence or absence of a protein corona on silica nanoparticle uptake and impact on cells. *ACS Nano* **6**, 5845-5857 (2012).

16 A. Cifuentes-Rius, H. De Puig, J. C. Y. Kah, S. Borros & K. Hamad-Schifferli. Optimizing the properties of the protein corona surrounding nanoparticles for tuning payload release. *ACS Nano* **7**, 10066-10074 (2013).

17 K. Furumoto, K.-I. Ogawara, S. Nagayama, Y. Takakura, M. Hashida, K. Higaki & T. Kimura. Important role of serum proteins associated on the surface of particles in their hepatic disposition. *J. Control. Release* **83**, 89-96 (2002).

18 S. Nagayama, K.-I. Ogawara, Y. Fukuoka, K. Higaki & T. Kimura. Time-dependent changes in opsonin amount associated on nanoparticles alter their hepatic uptake characteristics. *Int. J. Pharm.* **342**, 215-221 (2007).

19 P. Aggarwal, J. B. Hall, C. B. Mcleland, M. A. Dobrovolskaia & S. E. Mcneil. Nanoparticle interaction with plasma proteins as it relates to particle biodistribution, biocompatibility and therapeutic efficacy. *Adv. Drug Del. Rev.* **61**, 428-437 (2009).

20 R. Gref *et al.* 'Stealth' corona-core nanoparticles surface modified by polyethylene glycol (PEG): influences of the corona (PEG chain length and surface density) and of the core composition on phagocytic uptake and plasma protein adsorption. *Colloids Surf. B. Biointerfaces* **18**, 301-313 (2000).

21 J. Kreuter, D. Shamenkov, V. Petrov, P. Ramge, K. Cychutek, C. Koch-Brandt & R. Alyautdin. Apolipoprotein-mediated transport of nanoparticle-bound drugs across the blood-brain barrier. *J. Drug Target.* **10**, 317-325 (2002).

22 V. Mirshafiee, R. Kim, S. Park, M. Mahmoudi & M. L. Kraft. Impact of protein pre-coating on the protein corona composition and nanoparticle cellular uptake. *Biomaterials* **75**, 295-304 (2016).

23 Y. Ishihama, Y. Oda, T. Tabata, T. Sato, T. Nagasu, J. Rappsilber & M. Mann. Exponentially modified protein abundance index (emPAI) for estimation of absolute protein amount in proteomics by the number of sequenced peptides per protein. *Mol. Cell. Proteomics* **4**, 1265-1272 (2005).

24 J.-C. Leroux, F. De Jaeghere, B. Anner, E. Doelker & R. Gurny. An investigation on the role of plasma and serum opsonins on the evternalization of biodegradable poly (D, L-lactic acid) nanoparticles by human monocytes. *Life Sci.* **57**, 695-703 (1995).

25 E. Mahon, A. Salvati, F. B. Bombelli, I. Lynch & K. A. Dawson. Designing the nanoparticle–biomolecule interface for “targeting and therapeutic delivery”. *J. Control. Release* **161**, 164-174 (2012).

26 Z. J. Deng, M. Liang, M. Monteiro, I. Toth & R. F. Minchin. Nanoparticle-induced unfolding of fibrinogen promotes Mac-1 receptor activation and inflammation. *Nat. Nanotechnol.* **6**, 39-44 (2011).

27 K. Furumoto *et al.* Effect of coupling of albumin onto surface of PEG liposome on its in vivo disposition. *Int. J. Pharm.* **329**, 110-116 (2007).

28 K.-I. Ogawara, K. Furumoto, S. Nagayama, K. Minato, K. Higaki, T. Kai & T. Kimura. Pre-coating with serum albumin reduces receptor-mediated hepatic disposition of polystyrene nanosphere: implications for rational design of nanoparticles. *J. Control. Release* **100**, 451-455 (2004).

29 I. Mellman & H. Plutner. Internalization and degradation of macrophage Fc receptors bound to polyvalent immune complexes. *J. Cell Biol.* **98**, 1170-1177 (1984).

5.6 FIGURES AND TABLES

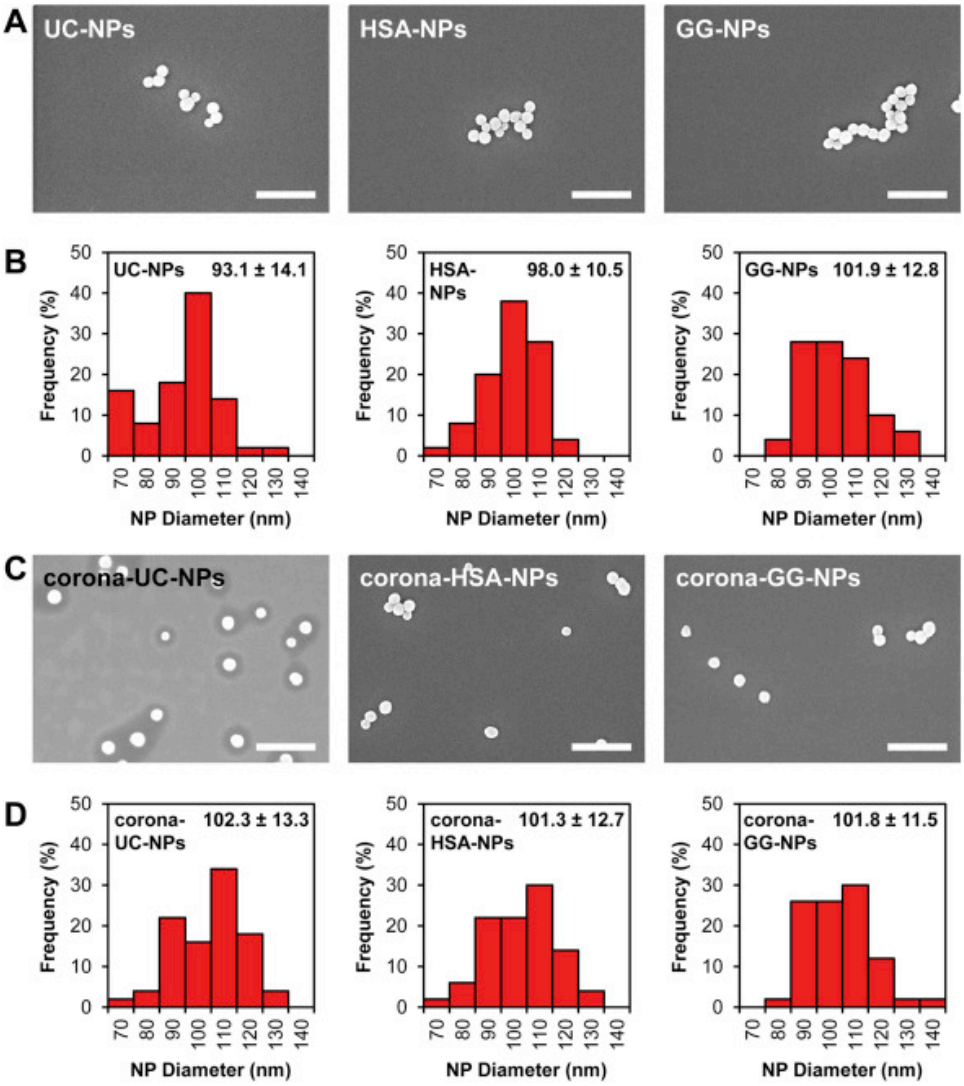

Figure 5.1. The sizes and the size distributions of the nanoparticles used in this study. A: SEM images and B: the corresponding size distribution of the pre-coated nanoparticles. C: SEM images and D: the corresponding size distributions of the corona-coated nanoparticles. Scale bars in A and C indicate 500 nm.

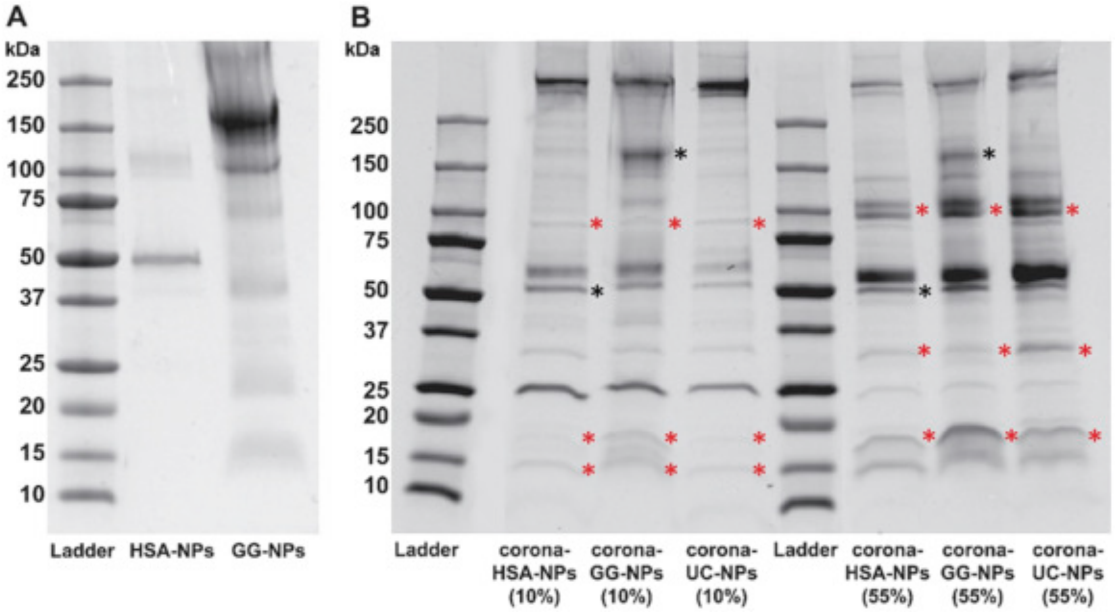

Figure 5.2. Detection of the proteins on the pre-coated nanoparticles (A) and in the protein coronas that formed on the nanoparticles by exposure to human plasma solutions (B) by SDS-PAGE. The black stars indicate the bands produced by the pre-coated proteins. The red stars represent the proteins that were detected in all samples but vary in intensity between the samples.

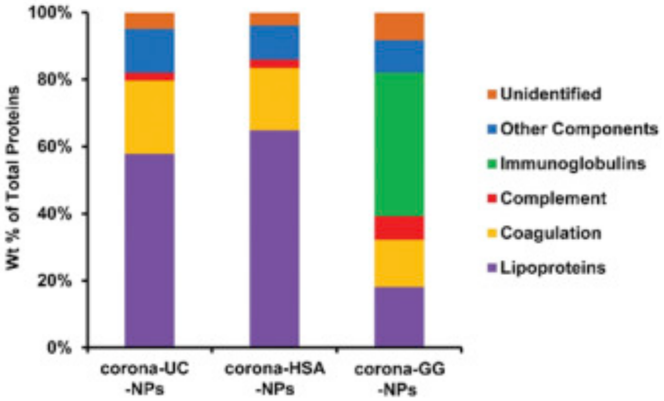

Figure 5.3. Comparison and functional characterization of the corona proteins. The proteins identified by LC-MS/MS analyses of the protein coronas on each type of nanoparticle, and were classified according to their biological functions in the blood.

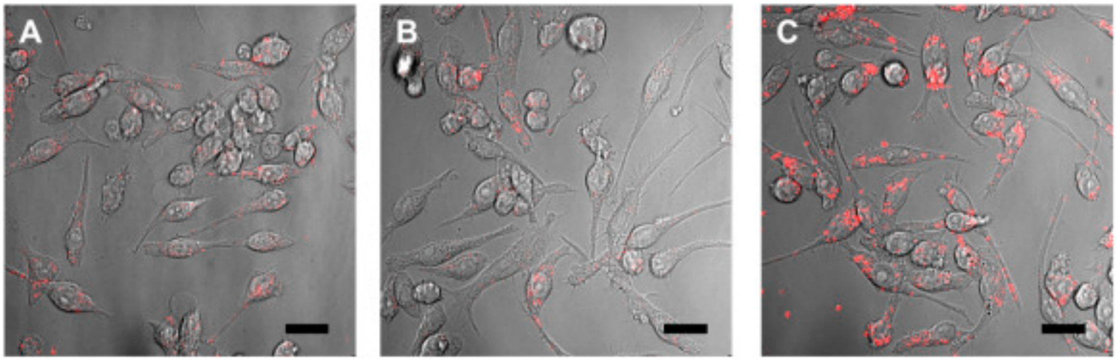

Figure 5.4. Confocal microscopy images of RAW 264.7 cells incubated with A: corona-UC-NPs, B: corona-GG-NPs, and C: GG-NPs (which were not exposed to plasma). The fluorescence images were overlaid on the DIC images of the same locations. Note that the cellular uptake of the GG-NPs was significantly higher than that of the other two types of corona-coated nanoparticles. Scale bars indicate 20 μm.

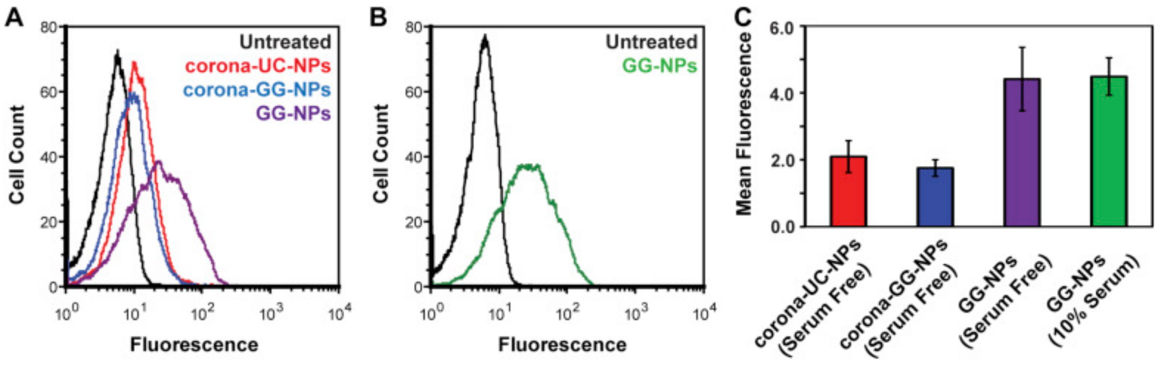

Figure 5.5. Comparison and quantification of nanoparticle uptake using flow cytometry. Flow cytometry curves for the uptake of different types of nanoparticles in A: serum-free medium, and B: 10% serum-supplemented medium. C: quantification of the flow cytometry results.

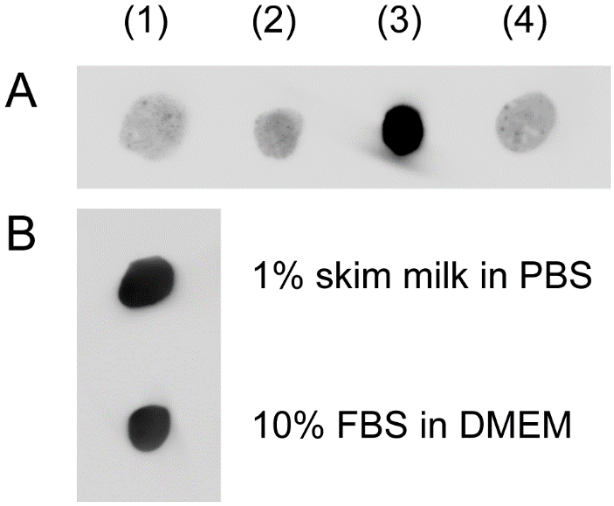

Figure 5.6. Immunodot blot comparison of the accessibility of the immunoglobulins on the surfaces of the nanoparticles. A: Antibody binding to the accessible immunoglobulins on (1) corona-UC-NPs, (2) corona-GG-NPs, (3) GG-NPs, and (4) GG-NPs that had been exposed to DMEM supplemented with 10% serum. Darker color signifies higher antibody binding, and thus, higher immunoglobulin accessibility in the protein corona. The immunoglobulins on the GG-NPs (3) were the most accessible. B: The immunoglobulins accessible to antibody binding in the standard dilution solution for immunoblotting (1% skim milk) or typical cell culture medium, which contains 10% FBS. Immunoglobulin detection by antibody only slightly decreased in the presence of serum.

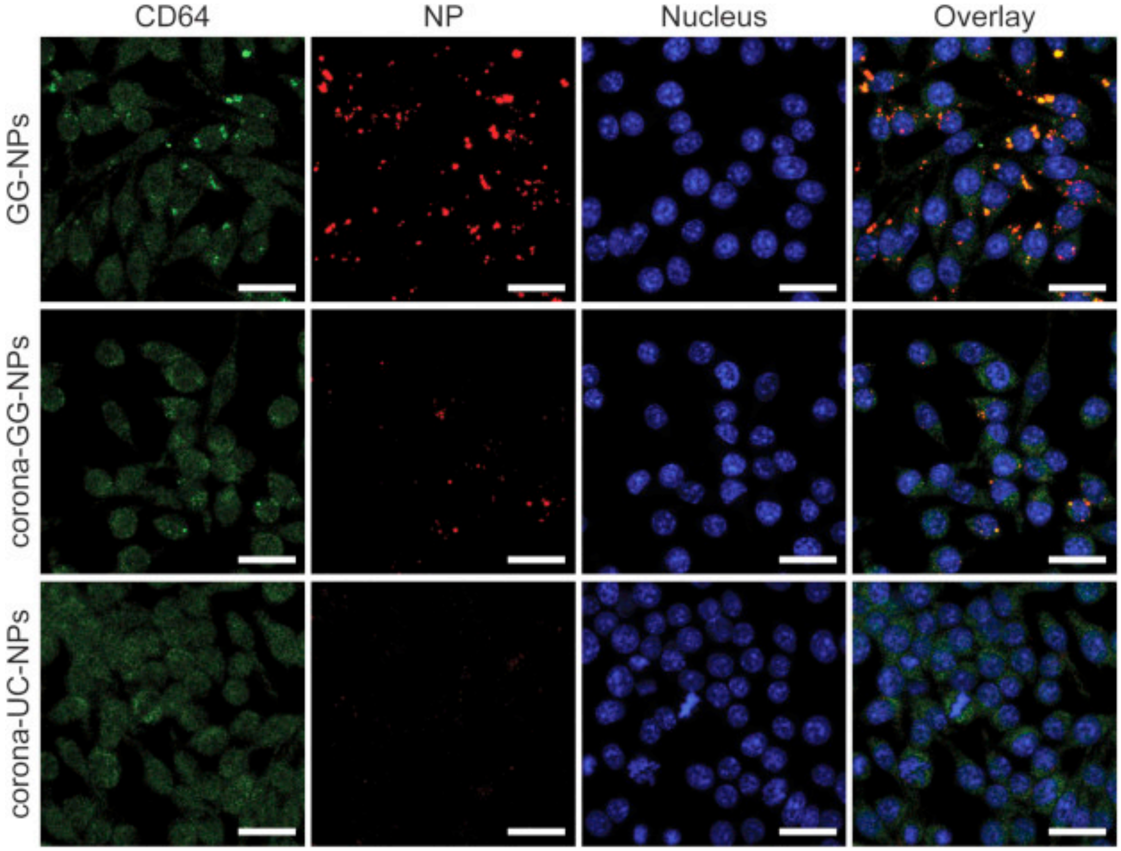

Figure 5.7. Confocal fluorescence microscopy images of each type of nanoparticle in parallel with immunolabeled CD64, a Fc receptor. RAW 264.7 cells were incubated with the nanoparticles for 2 h and then fixed and immunolabeled against CD64. The cell nuclei were stained with Hoechst 33342. Red: nanoparticles; green: immolabeled CD-64; blue: nuclei stained with Hoechst 33342. Scale bars are 20 μm.

Table 5.1. Characterization of nanoparticle ζ-potential, diameter (d, hydrodynamic diameter measured with DLS), size distribution (polydispersity index, PDI), and diameter measured with SEM.

Type of NPs	ζ-potential (mV)	d, hydrodynamic (nm)	PDI	d, SEM (nm)
UC-NPs	-29.83 ± 3.00	94.5 ± 1.1	0.086	93.1 ± 14.1
HSA-NPs	-17.03 ± 1.54	343.9 ± 10.0	0.338	98.0 ± 10.5
GG-NPs	-12.79 ± 2.08	749.2 ± 19.6	0.336	101.9 ± 12.8
corona-UC-NPs	-10.18 ± 1.02	157.9 ± 3.0	0.282	102.3 ± 13.3
corona-HSA-NPs	-8.00 ± 3.22	212.8 ± 1.9	0.223	101.3 ± 12.7
corona-GG-NPs	-7.19 ± 3.17	292.6 ± 11.6	0.353	101.8 ± 11.5

Table 5.2. Ten most abundant proteins detected by LC-MS/MS in each protein corona

corona-UC-NPs	corona-HSA-NPs	corona-GG-NPs
Apolipoprotein E	Apolipoprotein E	Apolipoprotein B100
Apolipoprotein E chain A	Apolipoprotein E4 chain A	Apolipoprotein E
Alpha fibrinogen	Kininogen-1	Ig gamma-1 heavy chain
Apolipoprotein C3 chain A	Serum albumin	Ig heavy chain
Fibrinogen chain A	Apolipoprotein B100	Ig M chain C
Apolipoprotein B100	Gelsolin	Histidine-rich glycoprotein
Gelsolin	Histidine-rich glycoprotein	Complement C3
Tetranectin	Apolipoprotein C3 chain A	Complement C4-A
Kininogen-1	Apolipoprotein J	Proapolipoprotein
Serum albumin	Plasminogen	Fibrinogen alpha chain

CHAPTER 6

CONCLUSIONS AND FUTURE OBJECTIVES

We established metabolic labeling methods that may be used to study the behavior of cellular sphingolipids using two different tags, fluorophores and stable isotopes. With the fluorophore-tagged sphingosines, we were able to visualize and track sphingolipids and their metabolites within cells. Stable isotope labeling offered a novel opportunity to investigate sphingolipid metabolism more comprehensively than with the traditional use of radioactive labels. We also investigated whether sphingolipids affect influenza virus infection. Lastly, we demonstrated that the adsorption of undesired proteins to the nanoparticle during protein corona formation impairs the active targeting of nanoparticles by covering the plasma proteins that were recruited to the corona due to their targeting capabilities. Consequently, the spatial orientation of the plasma proteins with targeting capabilities within the corona must be controlled for efficient active targeting.

Chapter 2 describes the use of fluorescent sphingosines for labeling and visualizing sphingolipids and their metabolites in cells. BODIPY 540 sphingosine was designed and developed to enable labeling and visualizing both sphingolipids and their metabolites. We confirmed that BODIPY 540 sphingosine was metabolized following native sphingolipid metabolic pathways. Interestingly, compared to BODIPY sphingosine, BODIPY 540 sphingosine produced more BODIPY 540 glycerophospholipids than BODIPY 540 sphingolipids in NIH3T3 mouse fibroblast cells. The cause of this difference in the metabolism of these two fluorescent sphingosines is of interest. The subcellular location of the BODIPY 540 sphingosine metabolites was observed in conjunction with distinct organelle markers. The BODIPY 540 sphingosine metabolites were located at the ER, the Golgi apparatus and the mitochondria at 30 min post-labeling and were transported out of these organelles over time, primarily to the plasma membrane. Their abundance at the lysosomes was low at 30 min post-labeling compared to other organelles, but this abundance increased over time, likely due to (sphingo)lipid catabolism. In summary, we demonstrated that BODIPY 540 sphingosine is a useful tool to investigate sphingolipid metabolism and subcellular localization, and possibly for use in vitro assays.

The other labeling method to study sphingolipid behavior was demonstrated in Chapter 3. When combined with imaging mass spectrometry, such as secondary ion mass spectrometry performed with a NanoSIMS instrument, stable isotope labeling is a valuable tool for visualizing cellular lipids. Here we showed that stable isotope labeled sphingoid bases and mass spectrometry detection can not only provide the same information as radioactive labeling, a traditional tool to study sphingolipid metabolism and behavior, but it also yields additional information about the unlabeled species. Recently developed high mass resolution mass spectrometry techniques facilitate the use of stable isotope-labeled sphingolipid precursors by provided a highly specific detection mechanism. Our lipidomics analysis of unlabeled lipid from NIH3T3 mouse fibroblast cells revealed that C_{16}-SM is the major sphingolipid, accounting for about 60% of all sphingolipid species. The incorporation of ^{15}N-sphingoid bases and ^{13}C-fatty acids over various labeling times were assessed using LC-MS analysis. The pattern of ^{15}N-sphingoid base incorporation into ceramide and sphingomyelin was similar to that of ^{3}H-sphingosine, clearly showing that stable isotope labeling can be used as a substitute for radioactive labeling.

Overall, in Chapter 2 and Chapter 3, we developed tools to metabolically label sphingolipids with fluorescence tags and stable isotopes. One drawback of these metabolic labeling approaches is that the exogenously added labels can change the flux of metabolic products in the cells. Because the labels and their immediate metabolites, ceramides, are proapoptotic, their addition may also adversely affect cell growth. Therefore, the labeling conditions should be carefully chosen based on the purpose of the labeling and the cell's ability to tolerate the labels. Investigations that are carefully designed to perturb distinct pathways in sphingolipid metabolism (such as using inhibitors of certain steps in sphingolipid metabolism or labeling with only ^{15}N-sphingosine instead of both ^{15}N-sphingosine and ^{15}N-sphinganine) will enable closer scrutiny of sphingolipid metabolism and ultimately, deciphering the intertwined sphingolipid biosynthesis and catabolic pathways. In order to obtain a more complete understanding of sphingolipid metabolism, trafficking, and function, the secreted sphingolipids would also need to be analyzed, which would be facilitated by pulse-chase labeling.

The involvement of sphingolipids, in particular those generated by aSMase, in influenza virus infection was investigated in Chapter 4. Prior to virus infection, aSMase in the cells and in conditioned culture media was detected by Western blot. Our data clearly show that a significant amount of aSMase was secreted, while this enzyme was barely detected in the cell lysates. Even though sphingolipids have been shown to regulate the entry of many pathogens into cells, under our experimental conditions, influenza virus entry decreased by only 20% when the aSMase level was lowered through use of siRNAs and a functional inhibitor, desipramine. Desipramine treatment significantly decreased virus particle release 8 hpi, but knockdown of SMPD1 was not as effective as desipramine treatment. This suggests that the inhibitory effect of desipramine treatment on the infection may be attributed to its biological actions other than inhibiting aSMase. We revealed that influenza virus entry led to an upregulation of SMPD1 levels in the cells, which implies that aSMase may be involved in an early phase of influenza virus infection. More studies are needed to verify the potential role of acid sphingomyelin in influenza virus infection. Such work will need to use other methods, such as overexpression or complete knockdown by genome editing, to manipulate the aSMase levels in the host cells. These studies have the potential to markedly improve our understanding of sphingolipid functions and their roles in infection.

Finally, in Chapter 5, we showed that the protein corona, the protein layer that forms on nanoparticles when they are exposed to biological fluids, such as whole blood or plasma, can be manipulated, prior to protein corona formation, by coating the nanoparticles with proteins that have an affinity for the subset of the plasma proteins with the desired targeting capabilities. Opsonin mediated endocytosis in immune cells was utilized as a model system to evaluate the feasibility of manipulating the protein corona composition and its effects on cellular uptake. We demonstrate that, although the protein pre-coating increases the abundance of the desired plasma proteins in the protein corona, the adsorption of other plasma proteins to the nanoparticle during protein corona formation significantly reduces nanoparticle uptake by preventing the targeting proteins on the nanoparticles from binding to their targets on the cell surface. Our data suggest that in addition to the abundance of the targeting proteins in the protein corona, their orientations must also be regulated to attain more efficient targeted nanoparticle delivery.